The Geological Cycle of Atacama Desert Nitrate Deposits, Northern Chile

I N A U G U R A L - D I S S E R T A T I O N

zur

Erlangung des Doktorgrades

der Mathematisch-Naturwissenschaftlichen Fakultät

der Universität zu Köln

vorgelegt von

Camila Javiera Riffo Contreras

aus Calama, Chile

angenommen in

Köln 2026

Abstract

The Atacama Desert of northern Chile hosts the world's largest natural nitrate accumulations, whose origin and geologic evolution have long been debated between atmospheric and volcanic mechanisms, among others (Ericksen, 1983; Chong, 1994; Böhlke *et al*., 1997; Michalski *et al.,* 2004; Pérez-Fodich *et al*., 2014; Reich & Bao, 2018). However, there is currently no universally accepted model that explains all types of nitrate deposits across their different geological contexts.

This thesis develops a multi-source genetic model by integrating detailed field mapping, chemical composition, and multi-isotope ($\delta^{18}O$, $\Delta^{17}O$, $\delta^{15}N$, $\delta^{34}S$) analyses of nitrate and associated sulfates from all major deposit types—sedimentary (type-i), veins in sedimentarx deposits (type-iia), neptunic dykes (type-iib), veins in rocks (type-iic), and salar-type (type-iii)—across the Tarapacá and Antofagasta regions. Systematic sampling yielded nitrate-bearing soils, caliche, veins, dykes, salt crusts, and host rocks, which were characterized by characterized by spectrophotometry for nitrate concentration, inductively coupled plasma optical emission spectrometer (ICP-OES) for soluble salts composition, Thermo Finnigan MAT253 isotope ratio mass spectrometer (IRMS) for triple-oxygen, nitrogen, and sulfur isotope composition, and Raman spectroscopy for mineralogy identification.

All nitrate types display large positive $\Delta^{17}O$ anomalies (+13 to +22‰) and high $\delta^{18}O$ values (+43 to +65‰), confirming a mass-independent oxygen isotope signature acquired during photochemical oxidation of NO_x by ozone and demonstrating a dominantly atmospheric source for nitrate in every deposit type. The positive correlation between $\Delta^{17}O$ and $\delta^{18}O$, in addition to their regression extrapolated to $\Delta^{17}O$ = 0‰ ($\delta^{18}O$ = 2.47‰), which closely matches the average $\delta^{18}O$ of fossil hydrothermal water ($\delta^{18}O$ = 2.89‰), suggests a hydrothermal recycling of the deposits. Nitrogen isotopes ($\delta^{15}N$ = −8 to +4‰) fall within the range of atmospheric and volcanic-lightning nitrate and show a weak positive correlation with $\Delta^{17}O$ and $\delta^{18}O$, inconsistent with strong microbial recycling and instead reflecting limited post-depositional alteration of an originally atmospheric nitrogen reservoir. Sulfur isotopes in associated sulfates ($\delta^{34}S$ = −2.1 to +9.8‰), together with a distinctive thenardite trend toward a $\Delta^{17}O \approx 0$ hydrothermal endmember (Klipsch *et al*., 2023), indicate mixing among

secondary atmospheric and hydrothermal sulfate sources, with the most ^{34}S-depleted values approaching El Tatio–type hydrothermal signatures.

Field relations and Raman spectra reveal nitratine–epsomite–erdite assemblages as exsolution and amygdaloidal infill within Paleocene–Eocene rhyolites and structurally controlled veins, demonstrating the involvement of nitrate-bearing hydrothermal fluids that dissolved, transported, and reprecipitated pre-existing atmospheric nitrate rather than generating new nitrate in situ. Integrating these observations, the thesis proposes a two-stage "geological super-cycle" for Atacama nitrates. In the first stage, long-term atmospheric deposition, focusing, groundwater transport, and evaporative enrichment in endorheic basins under increasing Andean uplift and hyperaridity form sedimentary and related deposits (type-i to type-iib). In the second stage, hydrothermal and tectonic reactivation of buried nitrate-rich sequences drives partial nitrate–water oxygen exchange and concentrates nitrate into vein-type-iic deposits, while preserving the atmospheric $\Delta^{17}O$ and light $\delta^{15}N$ signatures. This two-mechanism framework reconciles the isotopic, mineralogical, and spatial diversity of sedimentary and bedrock nitrate deposits, demonstrating that the Atacama province records a coupled atmospheric–hydrothermal cycle linked to the tectonic and magmatic evolution of the central Andean margin, and providing a template for other nitrate-bearing deserts and for the search for oxidized nitrogen on Mars.

Table of Contents

1 Introduction

The Atacama Desert Nitrate Deposits in Northern Chile, a unique case world around, are well known for their widespread occurrence in the hyperarid desert, within the Central Depression, and eastern border of Coastal Cordillera, from the longitude of Pisagua (19º35' S) in the Tarapacá Region to Taltal (25º34' S) in the Antofagasta Region (Figure 2.1). The severe conditions of hyperaridity since the Oligocene-Miocene (Dunai *et al.,* 2005; Ritter *et al*., 2018) make an ideal environment for the accumulation and preservation of water-soluble salts of the deposits. Nitrate ore deposits (called as *caliche* in the Chilean mining slang), was extensively mined since the second part of the 19th Century in the *Oficinas* (former nitrate mines) and continues to be mined today for its associated iodine, driving Chile as a major world producer of this element (Ericksen, 1981; Chong, 1994; Chong *et al.,* 2020). The Atacama nitrate deposits have been classified by Ericksen (1983) into two main types: the classic alluvial caliche, where nitrates occur as cement in poorly consolidated sedimentary rocks, and bedrock caliche with veins in various types of bedrock. A later generic classification was provided by Chong (1994), who identified three principal types. (i) Sedimentary deposits (same as alluvial caliche described by Ericksen, 1981), where the ore is included as thin veinlets, pores, and cement of detrital continental rock, sometimes including neptunic dykes (nitrate-cemented sands emplaced by hydraulic fracturing). ii) Deposits in rocks as veins, veinlets, massive bodies of continental desert sediment as manto-type deposits, with fine dissemination, up to 1-meter thickness, impregnating host rock of variable lithologies along fractures, fault or dissemination, in some areas displace in the same assemblage as supergene copper oxides and may also include neptunic dykes. And (iii) Miscellaneous deposits associated with saline crusts in salt flats, and nitrate ore in paleo-geothermal fields (Chong, 1994). Since the discovery of nitrate deposits, several authors have debated and dismissed different theories about their origin, leading Ericksen (1983) to explain the genesis and preservation of these deposits through several theories, including atmospheric, volcanic, marine, and some exotic ideas. Some deposits in rocks led Chong (1994) to propose a magmatism origin related to magmatic fluids produced during the Lower Tertiary volcanic arc. Subsequent oxygen isotope studies in Atacama nitrates revealed non-mass dependent signatures showing $\Delta^{17}O_{NO3}>0‰$, produced by photochemical reaction in the

troposphere and stratosphere (ozone oxidation pathways of NO_x), and thus, confirmed the primary source is atmospheric deposition in all measured nitrates (Michalski *et al*., 2004). A later study on chromium (Cr) and iodine (I) isotopes confirmed evaporative enrichment from groundwater aquifers in endorheic basins (Pérez-Fodich *et al.,* 2014). Together, these results support a multi-source genetic model involving primary atmospheric deposition, dissolution, and infiltration in the High Andes, groundwater transport, and evaporative enrichment Central Depression driven by increasing aridity and tectonic uplift (Pérez-Fodich *et al.,* 2014; and Reich and Bao, 2018). However, this model is not compatible with the formation of deposits in rocks (bedrock caliche) far displaced from alluvial planes, particularly those found in purely volcanic contexts, or the neptunic dykes. Previous $\Delta^{17}O$ isotope studies report a range between 14-20‰ for Atacama nitrates (Michalski *et al*., 2004) but did not report the full geologic context of the samples. This work reports the results from a study of the geological cycle of the different types of nitrate deposits. It uses multi-isotope composition ($\delta^{18}O$, $\Delta^{17}O$, $\delta^{15}N$, $\delta^{34}S$) from all depositional types sampled in the geologic setting to develop a general, generic depositional model for the Atacama Desert Nitrate Deposits. We suggest that the multi-source model (Pérez-Fodich *et al.,* 2014; Reich and Bao, 2018) is the first stage of a depositional super-cycle comprising sub-cycle(s) of primary atmospheric deposition – pluvial emplacement/groundwater transportation in shallow aquifer – evaporation enrichment – burial. The second stage of the super-cycle comprises hydrothermal reactivation of a buried sedimentary/alluvial deposit and pressured emplacement into fault planes and cracks.

2 Atacama Desert

2.1 Geomorphological and Geological Setting

The Atacama Desert in northern Chile extends between 18° and 27°S, extending roughly 700 km in length and 180 - 350 km in width. It is considered a tectonically active desert, primarily controlled by two major north-south fault systems: the Atacama Fault System to the west, active since the Jurassic, and the Domeyko System (West Fault System) to the east, active since the Paleogene (Chong *et al.*, 2020). In between, a third fragile structural system is considered since the Oligocene by Chong *et al.* (2020). As a product of these tectonic processes, six main physiographic units have developed from west to east: the Coastal Cordillera, Central Depression, Domeyko Cordillera (Precordillera), Pre-Andean Basins, High Andes Cordillera, and Altiplano (Puna; Figure 2.1). The Coastal Cordillera is a 30 km wide mountain range with elevations up to 3400 m, bounded to the west by a steep marine cliff that can rise to 1000 m. It is mainly composed of Jurassic-Cretaceous andesites and subordinate marine sedimentary rocks. The Central Depression is a tectonic forearc basin averaging 1000 m elevation and about 50 km in width, filled with Paleogene-Neogene volcanic deposits, Cenozoic fluvial sediments, and lacustrine sediments derived from eastern ranges. It also includes isolated reliefs of Mesozoic/Paleozoic rocks (Chong *et al.*, 2020). The Domeyko Cordillera (Precordillera) forms a tectonically uplifted block reaching ~5000 m of altitude. Its eastern border varies depending on the region. It is formed of folded and faulted sedimentary and volcanic rocks from the Precambrian to the present. The Pre-Andean Basins reach elevations around 2,300 m, with their lower parts containing Chile's largest salt flats (salars), including Salar de Atacama and Salar de Punta Negra. The High Andes Cordillera, dominated by Miocene up to recent volcanic structures, reaches up to 7000 m, including the youngest salt flats of Northern Chile (e.g., Salar del Huasco). The Altiplano forms a broad volcanic-sedimentary plateau up to approximately 4000 m high, sloping regionally to the west, displacing volcanic features from the Andes Cordillera (Chong *et al.*, 2020; Voigt *et al.*, 2020).

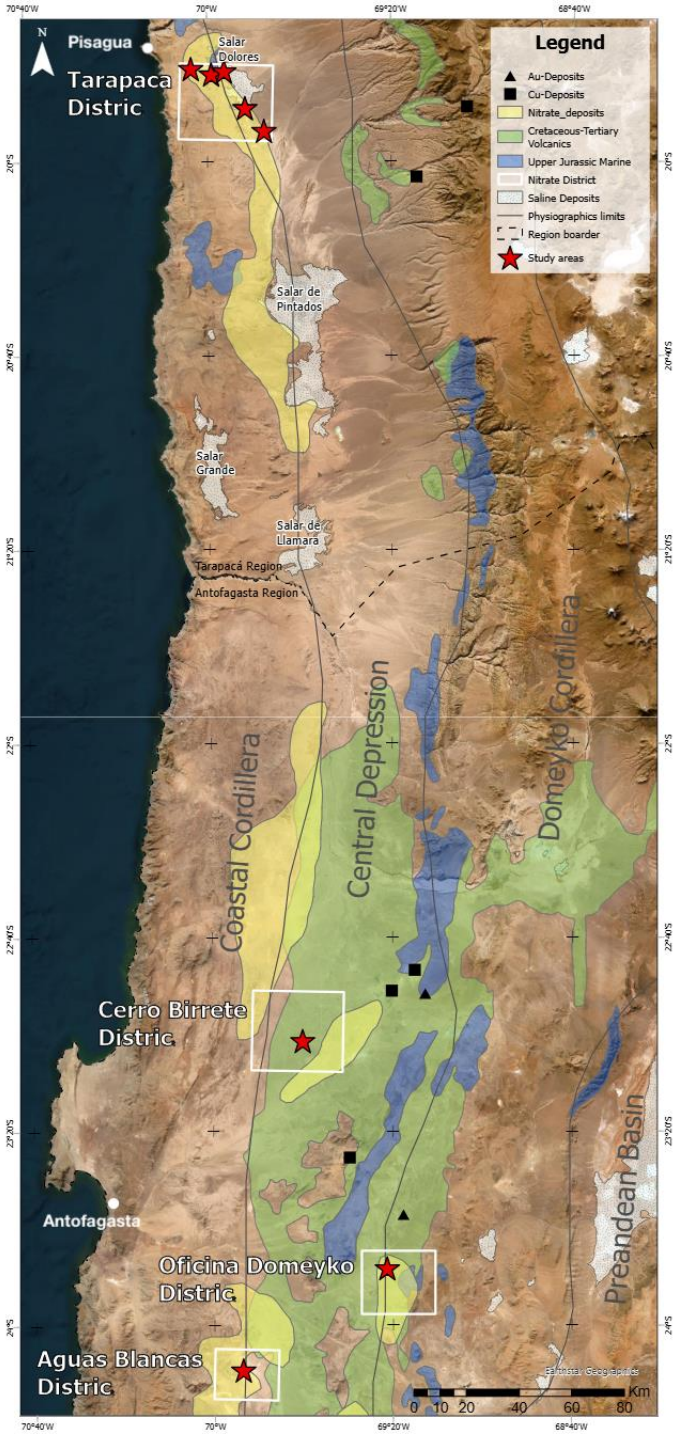

Figure 2.1: Map of Atacama Desert Nitrate Deposits of northern Chile (created using ArcGIS Pro). The location of the studied areas for this thesis is indicated with red stars, including from north to south: Oficinas California, Santa Rita, San Francisco, Asturias, Germania, Cerro Birrete, Oficina Domeyko, and the Aguas Blancas. The distribution of Nitrate Deposits (Michalski *et al.,* 2004) is shown in yellow, volcanic rocks from Cretaceous-Tertiary (Amilibia *et al.,* 2008; SERNAGEOMIN, 2003) are exhibited in green, and the paleographic reconstruction of the Jurassic Andean Basin (Vicente, 2006 in Pérez-Fodich *et al.,* 2015) is shown in blue. The physiographic units (Coastal Cordillera, Central Depression, Domeyko Cordillera, Preandean Basin) are separated by a solid gray line. Saline Deposits (Silva, 1977; Vásquez y Sepúlveda, 2013; Sepúlveda *et al.,* 2014; Vásquez *et al.,* 2018). Gold (Au) and Copper (Cu) deposits from the Paleocene-Eocene Metallogenic belt (Kojima and Campos, 2011) are indicated with black triangles and squares, respectively.

From north to south, the Atacama Desert is subdivided into four geographic regions, each with distinct geomorphological characteristics.

In the Arica and Parinacota Region (northernmost Atacama), the Altiplano extends westward to the Pacific coast, where Miocene ignimbrites and paleolake sediments, including diatomites, are observed in the northern sector of Arica city. The Coastal Cordillera progressively decreases in elevation and finally disappears at the Morro de Arica. This region is incised by deep east-west-oriented *quebradas* (ravines) that reach the sea and are probably controlled by important deep faults.

Farther south, in the Tarapacá Region, the landscape is dominated by a well-developed Central Depression, the Pampa del Tamarugal, an endorheic basin characterized by a flat surface and a dipping slope to the west. Its sedimentary filling derives from the erosion of the Precordillera and High Andes, which are practically together in this area. Several ravines descend from the eastern ranges, forming alluvial fans that terminate against the western flank of the Coastal Cordillera, giving rise to important salt-flats systems, such as the Salar de Pintados and the Salar de Llamara (Figure 2.1).

Continuing southward, the Antofagasta Region presents a markedly different structural pattern. It is transected by major regional faults that disrupt the continuity of the Precordillera, producing a more complex relief. Within the Central Depression, isolated hills and sierras emerge, contrasting with the more uniform topography of the Tarapacá Region. The Precordillera is separated from the High Andes by a series of fault-controlled basins—the Pre-Andean Basins—that host extensive salt-flat systems such as the Salar de Punta Negra and the Salar de Atacama, two of the largest in northern Chile (Chong *et al.,* 2020).

2.2 Climate Evolution and Implications

The hyperaridity of the Atacama is a paleoclimatic ancient feature, resulting from a unique convergence of tectonic and climatic conditions. The principal causes for the generation of these conditions are (1) its location within the subtropical high-pressure belt, where a continuous descent of warm, dry air masses is produced by the Hadley Cell circulation (latitudinal forcing); (2) the establishment of the upwelling, cold, north-flowing Humboldt Current along the Pacific coast produces a strong temperature inversion layer that inhibit precipitation in coastal regions (oceanic forcing); and (3)

the uplift of the Andes Cordillera, creating a profound rain shadow effect (elevation forcing), limiting moisture sources from the east (Hartley & Chong, 2002; Houston and Hartley, 2003; Hartley *et al*., 2005; Schween *et al*., 2020). These effects lead to a modern mean annual rainfall (MAR) of less than 1 mm yr^{-1} with some areas of 0.1 mm yr^{-1} (Houston, 2006), defining the hyperarid core of the Atacama Desert, a zone of extreme hyperaridity in the Coastal Cordillera and Central Depression between 19º and 22ºS at below 2000 m a.s.l. However, the climate in Atacama is more complicated than an untouchable hyperaridity, since it can be interrupted by wetter events/periods, but still arid (Ritter *et al*., 2018).

Precipitation takes place in the Atacama Desert. During summer, the precipitation occurs mainly at high altitudes, with moisture sources from the east (Houston, 2006). Nevertheless, extreme precipitation events also take place on the hyperarid core of the Atacama Desert, triggered by a weather pattern called "moist northerlies" (MNs), which transport moisture from the tropical eastern Pacific to the south (Vicencio *et al*., 2024). During winter, the precipitation is broadly distributed, increases to the south, and falls as snow at high altitudes (Houston, 2006).

An additional source of moisture that becomes significant in the absence of rain is Coastal fog. It is locally known as Camanchaca and forms a critical hydrologic input in the Coastal Cordillera below 1200 m and sometimes is even able to move inland through ravines, reaching some areas of the Central Depression (e.g., 50 km inland the Pampa del Tamarugal in the Tarapacá Region). This last one is known as an advective fog. Another type is the radiation fog, which occurs when the temperature in the Central Depression decreases during the night, forming condensation of atmospheric vapor (Cereceda *et al*., 2002;2008; Schween *et al*., 2020). Recently, monitoring from climate stations has revealed wind patterns with easterly winds during the night and morning, and westerly winds from noon to the evening, transporting moisture from the Pacific Ocean into the desert, forming fog during the night, providing a moisture supply in the hyperarid core of the Atacama Desert (Schween *et al*., 2020).

The onset of the hyperaridity in the Atacama Desert—conditions more severe than simple aridity—is a subject that remains in discussion. Evidence from terrestrial cosmogenic nuclide dating of erosion-sensitive landforms indicates that semi-arid to arid conditions were established by the Oligocene-Miocene (~25-23 Ma; Dunai *et al*., 2005), pointing to extremely low erosion rates consistent with a long history of aridity.

Sedimentological evidence from forearc basins argues for the onset of hyperaridity in the Late Pliocene (~3 Ma; Hartley & Chong, 2002). This timeline was further refined by studies of the ancient Atacama Planation Surface (APS), which was analyzed by cosmogenic ^{3}He and ^{21}Ne exposure ages, indicating that the surface has been stable for tenths of millions of years, suggesting the onset of hyperaridity may have start as early as the Middle Miocene (15-13 Ma) and certainly by the Late Miocene (8-10 Ma) (Evenstar *et al*., 2009; 2017). Later, an investigation on fluvial landscape evolution inferred the onset of hyperaridity since the Oligocene (~28-34 Ma), interrupted by wetter synchronic periods with the climate-induced changes on the Andean foothills (Ritter *et al*., 2018).

The hyperarid conditions of the Atacama Desert generate an elaborate and restricted hydrogeological system, resulting from the combination of tectonics (Andes uplift, landscape stability) and moisture sources (limited precipitation and fog), allowing the accumulation, remobilization, and preservation of high soluble salts, such as nitrate.

2.3 Nitrate Deposits

The nitrate deposits from the Atacama Desert are located in the eastern part of the Coastal Cordillera in the Tarapacá Region, forming the most abundant and continuous deposits, the Central Depression, and the western part of Domeyko Cordillera (Precordillera) of the Antofagasta Region, where they are spatially distributed along the west side of Upper Cretaceous -Paleogene volcanic rocks (Figure 2.1). In the Central Depression of the Tarapacá Region, these deposits and the volcanic rocks are covered by the sedimentary deposits of the Pampa del Tamarugal. There aren't nitrate deposits in the Arica and Parinacota Region; they were leached by the water flowing in the ravines that reach the ocean, preventing their accumulation (Chong, 1994; Chong *et al*., 2020). The classification of nitrates deposits is described in the next subsections and basically follows the classification of Ericksen (1981) and Chong (1994), with additional field observations and documentation enhanced during the development of this study.

2.3.1 Sedimentary Deposits (Type-i)

Continental sedimentary sequences are characterized by horizontal layers of sedimentary rocks, consolidated to semi-consolidated, deposited in distal and proximal alluvial fans. From top to bottom is described as follows: (1) Surface crust, a 0.5 cm thick layer of semi-consolidated sandstone, cemented mainly by sulfates with less abundant chlorates and nitrates. Volcanic, igneous, or sedimentary regolith lies on top. (2) Chuca, a 10-40 cm thick layer of semi-consolidated sandstone with volcanic clasts ~2 cm, cemented mainly by sulfates, with less abundant chlorates and nitrates, forming polygon structures (desiccation cracks). (3) Thenardite, a 4-20 cm thick layer of white powder, unconsolidated soluble salt. Sometimes it is mixed with volcanic clasts. (4) Costra, a 30 cm to 1 m thick layer of breccia matrix-supported with volcanic clasts 2-30 cm, moderately to well cemented by sulfates, chlorates, and nitrates. (5) Caliche, 50 cm to 3 m thick layer of breccia matrix-supported with volcanic clasts 2-10 cm. The matrix is composed of sandstone and is very well cemented by sulfates, chlorates, and nitrates. This layer contains the highest nitrate enrichment and is the mineral ore of the type-i deposits. (6) Coba, a layer of breccia matrix-supported with volcanic clasts, poorly cemented, and of variable thickness (Table A3.1; Figure 2.2; Ericksen, 1981; Chong, 1994; Chong *et al*., 2020).

This sedimentary sequence is not always complete as described above. In some cases, the Thenardite and/or the Coba layers are missing, and the Costra and Caliche layers are intercalated multiple times. In the Antofagasta Region, this profile is more commonly observed, but in the Tarapacá Region, the Thenardite layer is not so frequently exposed. The Caliche layer normally is intercalated with breccias composed of limestone and shale clasts in the Tarapacá Region, because of the underlying host rock.

These are the most common deposits, the famous alluvial-caliche deposits (Ericksen, 1981), and the only ones that have been isotopically analyzed before in previous studies.

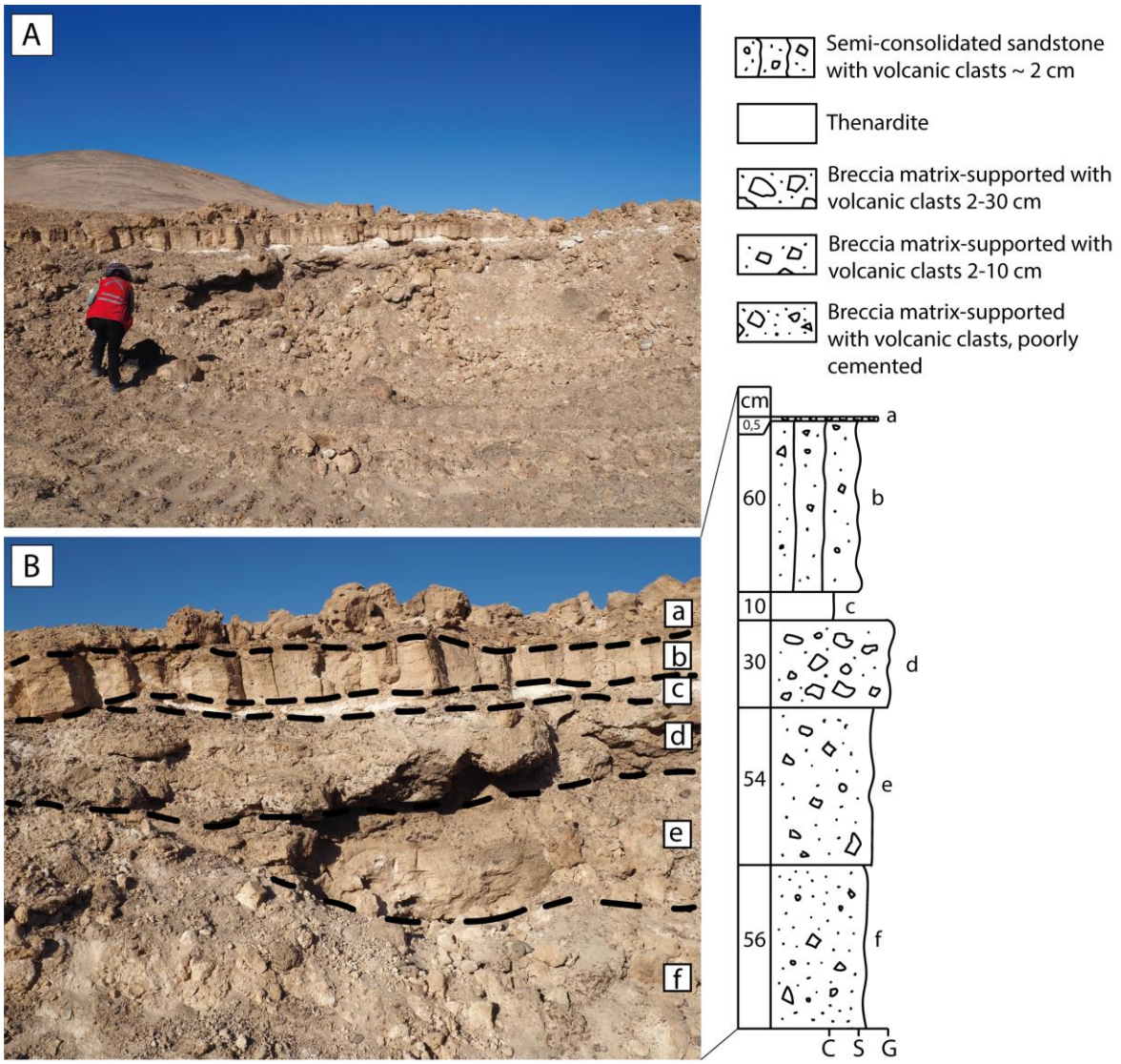

Figure 2.2: Sedimentary Deposit (type-i) from Aguas Blancas District (samples from ATA23-003/1). A) Sedimentary sequence in a proximal alluvial fan, showing the different layers of a type-I deposit. B) Close view from the upper picture, where the sedimentary profile can be better appreciated. The different layers correspond to a: surface crust, b: chuca, c: thenardite, d: costra, e: caliche, and f: coba. The thickness of the layers and the lithology are shown. Photographs by Swea Klipsch.

2.3.2 Veins in Sedimentary Deposits (Type-iia)

High nitrate concentrated mantos (horizontal structures cutting through sedimentary sequence; Chong, *Pers. Comm*.) cut through the sedimentary deposits at the caliche layer, or under it. Additionally, composed of chlorates, sulfates, and/or iodates (Table A3.1). Mainly, they are present as white structures, but the occurrence of iodine gives a yellow coloration to the veins (Table A3.1). They are from 10 to 50 cm thick, with massive or fibrous habits and, commonly, mixed with the Caliche layer from type-i

deposits in the contact zone (Figure 2.3). Commonly known as caliche blanco among miners. They are mostly located in proximal alluvial fans.

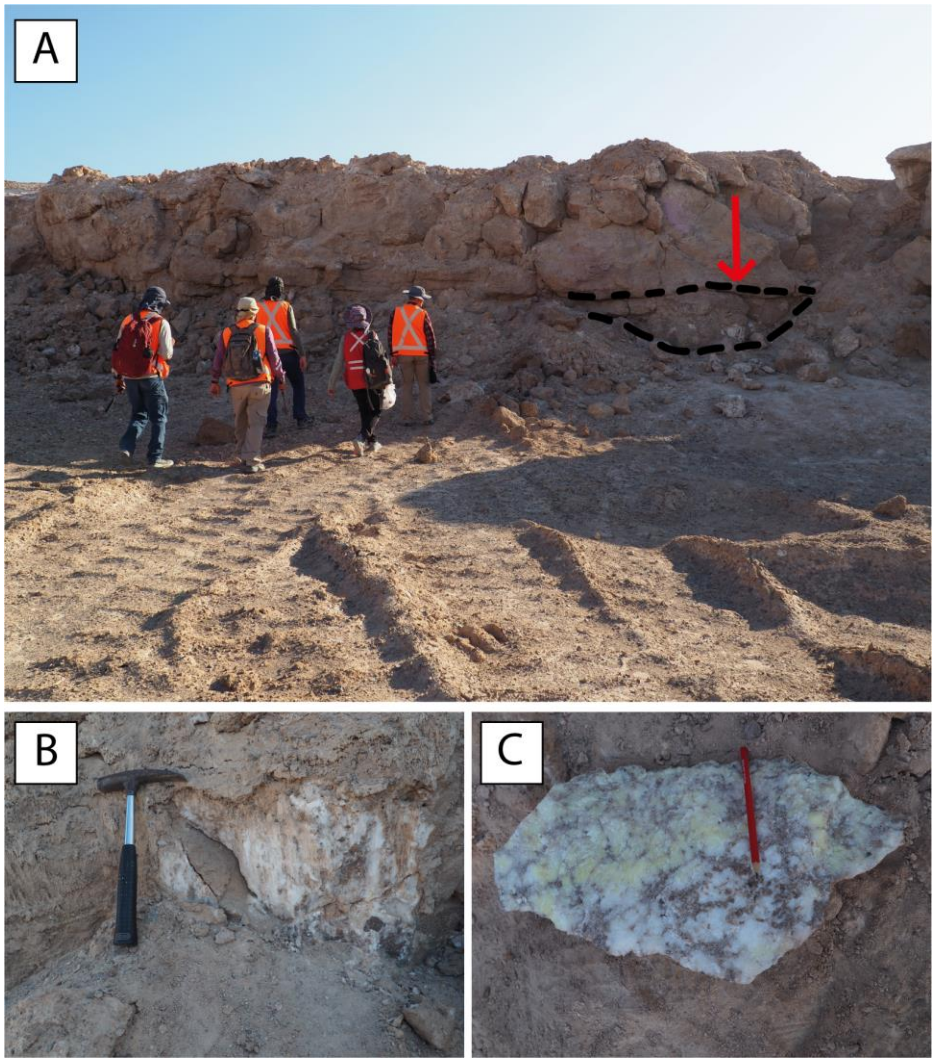

Figure 2.3: Veins in Sedimentary Deposit (type-iia) from Aguas Blancas District (samples from ATA23-003/2). A) View from the outcrop of a type-I deposit, in which a type-iia deposit is identified at the bottom of the sedimentary sequence. B) Close view of the position pointed with a red arrow in A. White fibrous manto cutting through type-i deposit. C) Massive white and yellow manto, with parts of the host Caliche from a type-i deposit. Photographs by Swea Klipsch.

2.3.3 Neptunic Dykes (Type-iib)

Detritus and saline material form under pressure conditions by superficial fluids, forming a very well-cemented sandstone, with nitrates, chlorates, sulfates, iodates, chromates, borates, and some strontium (Table A3.1) as cement material. They occur by filling cracks previously formed in volcanic or sedimentary rocks (Figure 2.4A-B), with a thickness from 10 to 20 cm and reddish-brown coloration. Frequently, they cut

through sedimentary sequences (e.g., brecciated rocks), and occasionally through type-iic deposits (see section 2.3.4; Figure 2.4C). Some of them include clast from the host rock, or present zonation due to different injection cycles (Figure 2.4A), and others present a massive texture (Figure 2.4 B-C). They were mined in the past as a high-grade nitrate ore (Chong *et al*., 2020).

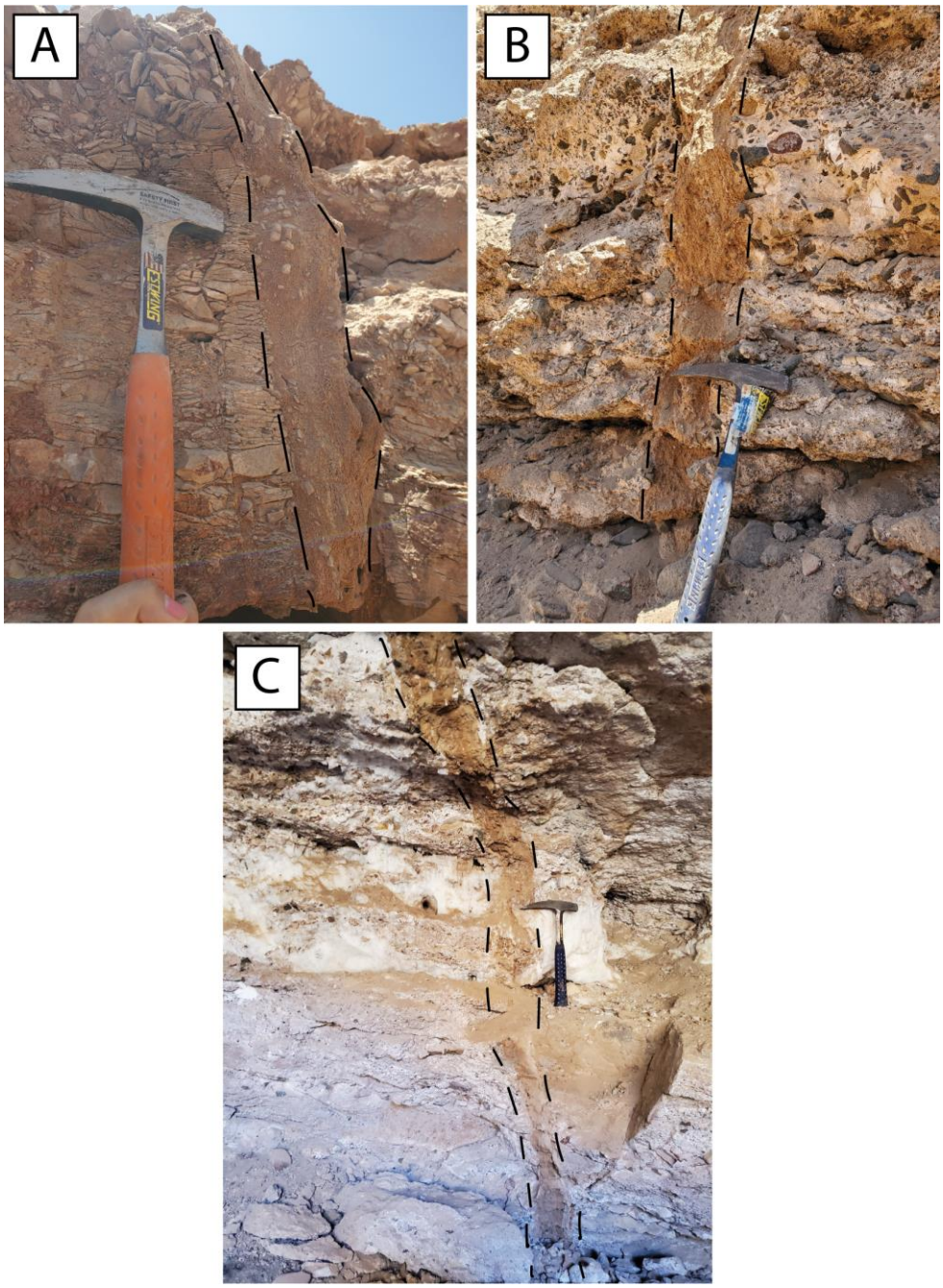

Figure 2.4: Neptunic dykes (type-iib), with thickness from 10-15 cm, and cutting through different host rocks, and from various localities. Cutting through A) brecciated shale from Oficina Santa Rita (Sample ATA23-101d), with some shale clasts included in the Neptunic Dyke; B) breccia-matrix supported (Sample ATA23-111a); and C) nitrate vein type-iic deposit from Oficina California (Sample ATA23-111d). Photographs by the author.

2.3.4 Veins in Rocks (Type-iic)

Thick structures (15 to 100 cm) cut horizontally (mantos) and vertically (veins) through massive volcanic or marine sedimentary rocks (Figure 2.5). Normally, with a massive habit, but occasionally fibrous, white (nitrate), yellow (iodane, cromates and bromates), and/or blue color (potassium nitrate, bromates; Table A3.1). They occur from the top surface to a depth of 4 m or more (unexplored). They are filled with sodium and potassium nitrates, sulfates, chlorates, and, in minor concentrations, iodates, chromates, borates, strontium, lithium (Table A3.1), and perchlorates (Chong *et al.,* 2020).

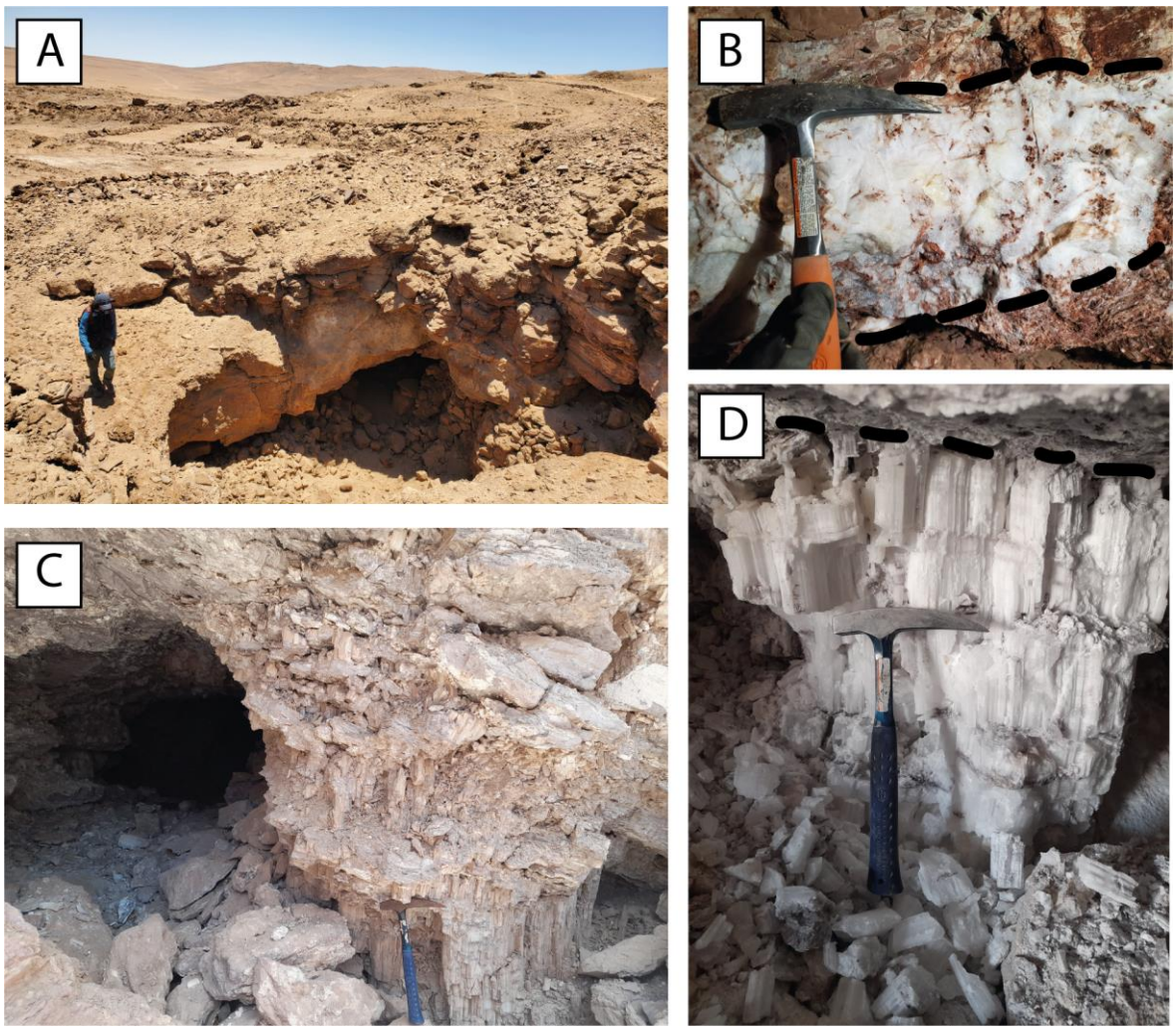

Figure 2.5: Veins in Rocks (type-iic). A) Landscape view of the entrance to a cave in the Oficina Santa Rita. B) Inside the cave, a massive white vein from Oficina Santa Rita (Sample ATA23-101b). C) View of the entrance to the cave in the Oficina Domeyko. D) Inside the cave, a white and fibrous manto cut through rhyolites (Sample ATA22-020A). The hammer measures 30 cm long. Photographs by the author.

2.3.5 Salt Flats Deposits (Type-iii)

The salars (salt flats) are endorheic sedimentary basins filled by sedimentary rocks and evaporites, occasionally intercalated with volcanic rocks. The salt accumulation is generated by transportation and evaporation of surface and groundwater, forming a saline crust on the surface, and lake systems when the recharge is greater than the evaporation rate. When the salar is completely dry (neither superficial nor underground brines), they are called Fossil Salars (Chong *et al.,* 2020). They are distributed along the Coastal Cordillera (e.g., Salar Grande), Central Depression (e.g., Salar Dolores, Salar de Pintados, Salar de Llamará, Salar de Navidad, Salar del Carmen; Figure 2.1; Figure 2.6), Pre-Andean Basins (e.g., Salar de Atacama, Salar de Punta Negra), and the High Andes (e.g., Salar del Huasco, Salar de Pajonales). The surface saline crust composition consists of chlorides, sulfates, nitrates, borates, and lithium (Table A3.1). They are considered part of nitrate ore deposits only when their crust contains sufficiently high nitrate concentrations to be economically mined, as is the case of Salar del Carmen (Antofagasta Region) and Salar Dolores (Tarapacá Region; Figure 2.6). The Salars from the Central Depression form in the distal part of alluvial systems from the Precordillera and the Andes Cordillera, as part of a lake system getting recharged from the east. A cycle of climate change that generates aridity changed the conditions of these lakes, evolving into salt flats in the deeper basins (Chong *et al.,* 2020).

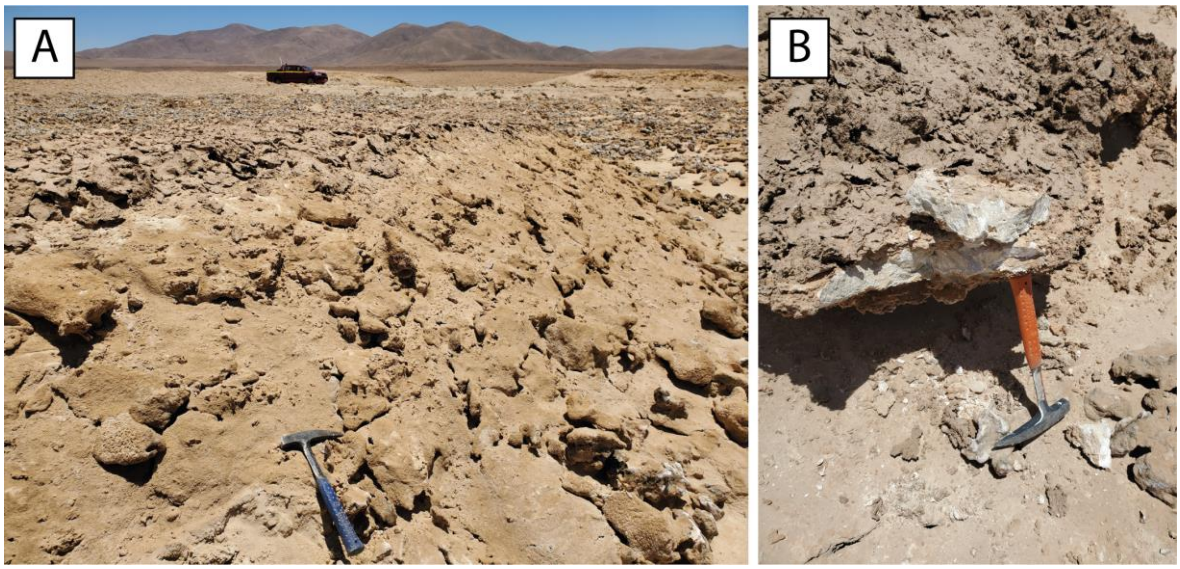

Figure 2.6: A) Salar Dolores (type-iii). B) Close view of the well-cemented salt crust. Photographs by the author.

2.4 Origin of Nitrate Deposits

The origin of Nitrate Deposits in the Atacama Desert has been a subject of debate among scientists since their discovery. Within these studies, the origin of the nitrates has been attributed to leaching of volcanic rocks (Whitehead, 1920); algae and vegetation decay in saline lakes (Sieveking *in* Ericksen, 1983) or sea water (Forbes, Noellner, Flagg & Muntz *in* Ericksen, 1983); nitrification and leaching of seabird guano (Hillminger, Gautier, Penrose *in* Ericksen, 1983); nitrification and fixation of atmospheric nitrogen by bacteria (Gale and Bruggen *in* Ericksen, 1983); reaction of nitric acid with feldspars from igneous rocks in nitrate fields (Pissis, Sundt, Wetzel, Knoche *in* Ericksen, 1983); accumulation of nitrogen compounds of volcanic origin in gases associated with intense Andean volcanism (Kalb, Fiestas, Steinmann *in* Ericksen, 1983), leaching from tuffs of rhyolitic composition from the Tertiary and Quaternary (Ericksen, 1961). Garret (1983) *in* Ericksen (1982) proposes two methods: (1) nitrates originated from the photocatalytic oxidation of nitrogen from various rock surfaces, and (2) for the other constituents of the deposits, he proposes that they were derived from hot springs or from the discharge of water from the Andes.

Michalski *et al*. (2004) did an oxygen isotope study that shows a non-mass-dependent signature ($\Delta^{17}O > 0‰$) in all measured nitrates. This signature is produced by photochemical reaction in the atmosphere (ozone oxidation pathways of NOx), postulating a primary atmospheric source. Oyarzun & Oyarzun (2007) stipulate that the volume of pyroclastic rocks of the Miocene-Pleistocene Altiplano-Puna Volcanic Plateau (APVP) created the conditions for electrical and thermal nitrogen fixation. Reich and Bao (2018), based on chromium (Cr) and iodine (I) isotopes of Pérez-Fodich et al. (2014), propose a multi-source model. Cr-isotopes are evidence for transportation in a reducing aquifer, and I-isotopes evidence of their source from marine Jurassic rocks from the Domeyko Cordillera, leading to the following mechanism formation: primary dry atmospheric deposition, dissolution and infiltration in the High Andes, groundwater transport, and evaporative enrichment from groundwater in the Central Depression, triggered by increasing aridity and tectonic uplift. Chong (1994) and Chong *et al*. (2020) consider that the nitrate deposits are closely related to units developed in the Paleogene volcanic arc, giving a magmatic origin for the nitrogen, which later would have been fixed as nitrates. During this

period, a wetter climate in the Lower Oligocene leads to the salt contribution and distribution from meteoric waters, and the development of geothermal activities in the later phases of volcanism. These salts would have been transported by conduits that favor their migration, such as faults, fractures, and porosity of strata, forming deposits type-iic, and the different permeability of the horizons in the sedimentary sequences would have allowed the mineralization of deposits type-i. However, there is currently no geochemical evidence to substantiate this proposed mechanism.

While research on nitrate formation in the Atacama Desert has been ongoing for more than 150 years, with continuous contributions from leading scientists and the incorporation of progressively advanced analytical techniques, there remains a need for integrative studies that combine detailed geological field observations, systematic sampling across deposit types, and comprehensive compositional and multi-isotopic analyses. Such an approach would refine and consolidate the existing models into a more unified framework for understanding the diverse geological settings of nitrate deposits in the Atacama.

3 Stable Isotope Geochemistry

3.1 Generalities

Stable isotope geochemistry provides a fundamental framework for tracing the origin, transformation, and preservation of elements in natural systems. In arid environments, the isotopic composition of nitrates, sulfates, and associated compounds provides key information about atmospheric inputs, biological activity, post-depositional processes, and paleoclimatic conditions (Böhlke *et al.,* 1997; Michalski *et al*., 2004; Thiemens, 2006; White, 2015; Sharp, 2017; Melchiorre *et al.,* 2018). Considering that the Atacama Desert represents one of the most hyperarid environments on Earth, isotopic tracers offer unique opportunities to trace atmospheric, volcanic, and biological signatures that would otherwise remain hidden in more dynamic hydrological systems (Pérez-Fodich *et al*., 2015; Reich & Bao, 2018). When integrating different isotope systems—oxygen, nitrogen, and sulfur in this thesis—the balance between volcanic, atmospheric, and biological processes that shape nitrate and sulfate deposits over geological time is constrained (Michalski *et al.,* 2004; Reich and Bao, 2018; Klipsch *et al.,* 2023).

In this context, stable isotope analysis serves as a complementary tool to geological, mineralogical, and geochemical evidence, allowing for the evaluation of the different processes that have contributed to the formation and evolution of nitrate deposits. Through the combined interpretation of oxygen, nitrogen, and sulfur isotopes, this study aims to develop a comprehensive model that explains the formation of the different types of nitrate deposits, integrating their isotopic signatures with field relations, mineralogical assemblages, and hydrothermal activity. This integrative approach contributes to a more complete understanding of the geological cycle of nitrate accumulation, transformation, and preservation in one of the most extreme environments on Earth.

3.1.1 The delta notation and isotope ratios

Isotopes are atoms of the same element with the same number of protons (p) but different numbers of neutrons (n). This means that they have the same atomic number

(Z=p) but different mass numbers (A=p+n). As a result, isotopes of an element have different masses and abundances and behave differently in nature. Natural processes that generate small chemical and physical differences between the isotopes of an element, such as kinetic effects, isotope exchange reactions (equilibrium distribution), and physicochemical processes (e.g., diffusion, condensation, and evaporation) allow the fractionation/separation of isotopes, changing their abundance/composition (Kendal & Caldwell, 1998; Hoefs, 2018).

Isotope composition is reported in ratios relative to internationally accepted standards (reference materials) using the delta (δ) notation (McKinney *et al.* 1950; Hayes, 2004; White, 2015; Sharp, 2017):

$$\delta^{*}X_{std} = \left(\frac{{}^{*}R_{\mathrm{smp}}}{{}^{*}R_{\mathrm{std}}} - 1\right) \cdot 1000 \qquad (3.1)$$

where ${}^{*}R$ is the ratio of the abundance of the rare/heavy to the abundant/light isotope, in the sample $\left({}^{*}R_{smp}\right)$, and the standard $({}^{*}R_{std})$. The * indicate the mass number of the rare/heavy isotope. For example, for oxygen, the delta notion would be $\delta^{17}O$ with $R = {}^{17}O/{}^{16}O$, or $\delta^{18}O$ with $R = {}^{18}O/{}^{16}O$ and, in the same way for others elements. The delta values are reported in per mil or parts per thousand (‰), and common standards include Vienna Standard Mean Ocean Water (VSMOW) for oxygen, atmospheric nitrogen (AIR) for nitrogen, and Vienna Cañon Diablo Troilite (VCDT) for sulfur (Sharp, 2017).

3.1.2 Isotope fractionation and fractionation factors

Isotope fractionation occurs because isotopes of the same element differ in mass and bond vibrational energies, generating differences in their chemical and physical properties, and altering the ratio of partition functions (isotopes distribution between different phases).

The fractionation factor (α) is a quantitative measure that describes the extent of fractionation between two phases A and B. Essentially, a ratio of the isotope abundance ratios in those phases, and it is defined as (Sharp, 2017; Hoefs, 2018):

$$\alpha_{A-B} = \frac{R_A}{R_B} = \frac{1000 + \delta_A}{1000 + \delta_B} \qquad (3.2)$$

Fractionation can originate from kinetic or equilibrium effects or both.

- Equilibrium isotope fractionation is related to reversible (bidirectional) processes like high-temperature reactions, where the isotope exchange occurs between coexisting minerals or between minerals and external fluid. The equilibrium fractionation is temperature-dependent and follows well-understood thermodynamic rules (Sharp, 2017; Hoefs, 2018).

- Kinetic isotope fractionation occurs with fast, incomplete, and irreversible (unidirectional) processes like evaporation, diffusion, bacterial metabolism (e.g., microbial reduction), dissociation reactions, or photosynthesis, generating large isotope fractionations. (Sharp, 2017; Hoefs, 2018).

3.1.3 Mass-dependent and mass-independent fractionation

In most terrestrial systems, fractionation (kinetic and equilibrium) is mass-dependent (MDF), which means isotopic ratios vary in proportion to their relative mass differences. That implies that for elements with more than 2 isotopes such as oxygen, the enrichment of the $^{18}O/^{16}O$ is expected to be approximately twice that of the enrichment of $^{17}O/^{16}O$ on Terrestrial materials, yielding to a relationship between $\delta^{17}O$ and $\delta^{18}O$ that follows a slope near 0.52, known as the Terrestrial Fractionation Line (TFL; Sharp, 2017; Hoefs, 2018), show in Figure 3.1 as MDF Line, typically expressed as:

$$\delta^{17}O \approx 0.52 \cdot \delta^{18}O \tag{3.3}$$

However, some processes in nature lead isotope behaviour to deviate from the MDF, described as mass-independent fractionation (MIF). This is the case of extra-terrestrial samples (e.g., carbonaceous chondrites, with a slope close to 1), and terrestrial samples that have undergone photochemical reactions (Thiemens & Heidenreich, 1983; Thiemens, 2006; Sharp, 2017).

For oxygen, MIF will generate slopes that lie off from the TFL when $\delta^{17}O$ is plotted against $\delta^{18}O$ (Figure 3.1), and is expressed as:

$$\Delta^{17}O = \delta^{17}O - \lambda \cdot \delta^{18}O \tag{3.4}$$

where λ is the main parameter that characterizes the mass-dependent fractionation and depends on the molecular mass. The λ-value in this case, and use in this thesis, is

0.52 for terrestrial materials (TFL) and is commonly used when dealing with large MIF effects (Klipsch, 2021), but can vary between 0.509, which is the lower limit for kinetic fractionation processes, and 0.530, which is the equilibrium high temperature limit (Young *et al.*, 2002 *in* Hoefs, 2018). Positive Δ-values indicate that samples or reservoirs are enriched relative to the predicted MDF line, whereas negative Δ-values reflect corresponding depletions. Although the precise mechanism of formation for MIF is still not fully understood, the best-characterized process involves ozone (O_3) formation in the stratosphere. This reaction, extensively documented in O_3, CO_2, N_2O, and CO, produces characteristic isotopic anomalies that serve as distinctive atmospheric markers and may also operate under comparable photochemical conditions on Mars (Thiemens, 1999; Hoefs, 2018). Consequently, MIF provides a unique isotopic fingerprint that captures non-mass-dependent processes and serves as a critical tracer for understanding atmospheric chemistry and planetary evolution (Figure 3.1; Hoefs, 2018).

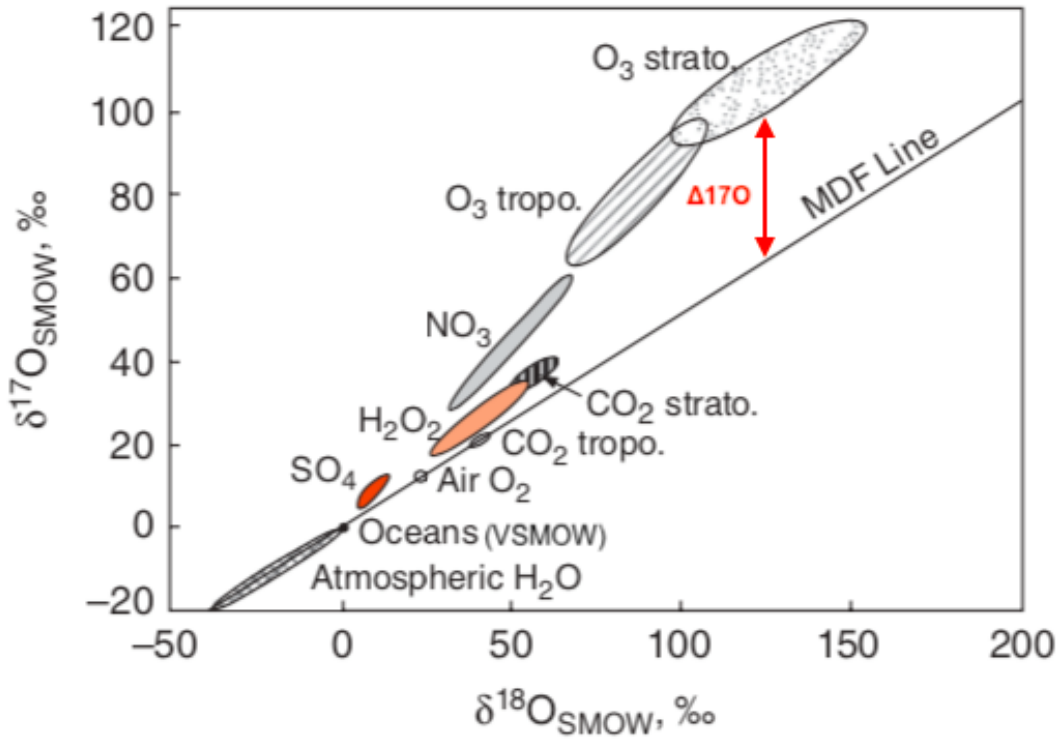

Figure 3.1: Oxygen isotopic composition of atmospheric oxygen-bearing species. MDF Line corresponds to the mass-dependent fractionation line of terrestrial materials (TFL) with a slope of 0.52. All oxygen-bearing species that lie off of this line present a mass-independent fractionation quantified by $\Delta^{17}O$ (red arrow). VSMOW refers to the Vienna Standard Mean Ocean Water. Figure modified from Thiemes and Shaheen (2014) *in* White (2015).

3.2 Triple Oxygen Isotopes in Nitrates

There are three stable isotopes of oxygen: ^{16}O, ^{17}O, and ^{18}O, with average terrestrial abundances in atom per cent are 99.757, 0.038, and 0.205, respectively (Sharp, 2017; Hoefs, 2018). For most natural processes, variations in ^{17}O and ^{18}O follow a mass-dependent relationship, because the relative fractionation of these isotopes is proportional to their mass differences (equation 3.3), as is the case with evaporation, condensation, or diffusion. However, in some atmospheric reactions, the ^{17}O isotope deviates from this proportionality, expressed as $\Delta^{17}O$ or ^{17}O- anomalies (equation 3.4; Figure 3.1). These anomalies are crucial for identifying atmospheric and biological oxygen sources.

Atmospheric nitrate can be formed through different oxidation pathways of nitrogen oxides (NO_x = NO+NO_2) in the troposphere during daytime:

$$NO_2 + OH + M \longrightarrow HNO_3 + M \tag{3.5}$$

and during nighttime:

$$NO_2 + O_3 \longrightarrow NO_3 + O_2 \tag{3.6}$$

$$NO_3 + HC, DMS \longrightarrow HNO_3 + products \tag{3.7}$$

$$NO_2 + NO_3 \longrightarrow N_2O_5 \tag{3.8}$$

$$N_2O_5 + H_2O_{(surf)} \longrightarrow 2HNO_{3(aq)} \tag{3.9}$$

In atmospheric geochemistry, M is a molecule that participate in the reaction by carrying away excess energy (energy transfer partner), often N_2 or O_2, but does not chemically change (Amedro *et al.*, 2020); HC refers to hydrocarbon, or broadly to volatile organic compounds (VOCs) of anthropogenic or biogenic origin; and DMS stands for dimethyl sulfide (CH_3SCH_3), is a sulfur-containing compound emitted mainly by marine phytoplankton and it is a precursor to other atmospheric sulfur compounds

such as SO_2, H_2SO_4. The products in equation 3.7 can be organic nitrates, sulfur-containing products, or other oxidation products (Michalski *et al*., 2003; Morin *et al*., 2007; Savarino *et al.,* 2013).

However, daytime NO_3 is negligible, except in shadowed/particle interiors, because it is rapidly photolyzed by sunlight; it only accumulates and reacts significantly at night. Nitrate forming during nighttime is recycled to the following photochemical reactions:

$$NO_2 + hv \longrightarrow NO + O(^3P) \quad (3.10)$$

$$O(^3P) + O_2 + M \longrightarrow O_3 \quad (3.11)$$

$$NO + O_3 \longrightarrow NO_2 + O_2 \quad (3.12)$$

$$NO + HO_2(RO)_x \longrightarrow NO_2 + OH(RO) \quad (3.13)$$

Where RO represents peroxy radicals, and $O(^3P)$ is the most stable and common form of atomic oxygen in the atmosphere, produced primarily by photolysis of NO_2 and O_3 (Michalski *et al*., 2003; Morin *et al*., 2007; Savarino *et al.,* 2013).

Because of the tropospheric bulk O_3 have $\Delta^{17}O$ values of around +26‰, and $\delta^{18}O$ between +111 to +115‰, and O_3 transferrable present ^{17}O-anomalies of around +39‰, and $\delta^{18}O$ between +126 and +130‰ (Vicars and Savarino, 2014; Figure 3.2B), the nitrate oxygen derived from ozone results in atmospheric nitrate being highly enriched in $\Delta^{17}O$, as high as +20 to +35‰, with $\delta^{18}O$ between +50 and +90‰ (Michalski *et al*., 2003; Patris *et al.,* 2007; Morin *et al.,* 2009; Savarino *et al*., 2013; Reich and Bao, 2018; Figure 3.2B).

The origin of reactive nitrogen oxides (NO_x) in the atmosphere can be related to the molecular N_2 breaking via volcanic lightning during explosive volcanic eruptions (Aroskay *et al.,* 2024; Contamine *et al.,* 2025). In the high-energy lightning channel, molecular N_2 can be dissociated and converted to reactive nitrogen oxides (NO, NO_2). Those NO_x species are rapidly oxidized in the plume atmosphere (notably by O_3 and other oxidants) to form nitrate (NO_3^-) that can be deposited with volcanic ash and aerosol fallout. This pathway is referred to as abiotic N-fixation via ozone-driven

oxidation in volcanic plumes, carrying a $\Delta^{17}O \approx 30\text{-}40‰$, and high $\delta^{18}O$ values in the order of +50 and +90‰, which vary with atmospheric chemistry and mixing (Aroskay *et al.,* 2024).

In contrast, biogenic nitrate formed through nitrification or microbial oxidation exhibits $\Delta^{17}O \approx 0‰$ due to complete oxygen isotope exchange with local water (Kaneko & Poulson, 2013). These zero anomalies can also be produced by NO_x oxidation by OH or other tropospheric radicals carrying a zero ^{17}O-anomaly (Aroskay *et al.,* 2024).

In the Atacama Desert, ^{17}O-anomalies in nitrates are direct indicators of atmospheric photochemistry (Thiemens, 1983; Michalski *et al.,* 2003), with positive $\Delta^{17}O$ values between +14 and +21‰ (Böhlke *et al.,* 1997; Michalski *et al*., 2004; Melchiorre *et al.,* 2018; Figure 3.2B) produced by photochemical reactions in the atmosphere, particularly the oxidation of NO_x by O_3.

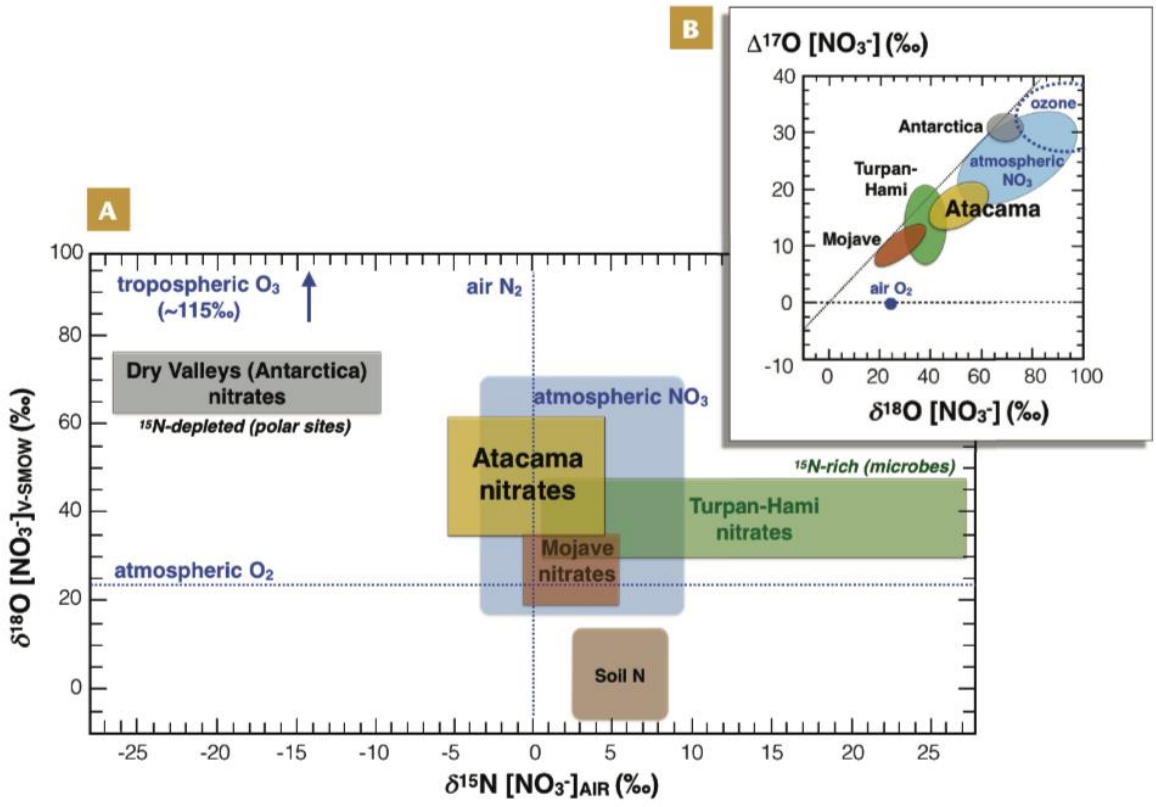

Figure 3.2: A) $\delta^{18}O$ vs $\delta^{15}N$, and B)$\Delta^{17}O$ versus $\delta^{18}O$ signatures of desert nitrate worldwide. The Sedimentary (type-i) Nitrate Deposit from the Atacama Desert (Chile) in yellow, the Mojave Desert (USA) in red, the Turpan-Hami Basin (China) in green, and the Antarctica Dry Valleys in grey. O-anomalies ($\Delta^{17}O$) indicate the varying mixture degrees of atmospheric nitrate and terrestrial nitrate produced by microbial nitrification, and nitrate-water oxygen exchange. Figure from Reich and Bao (2018).

The $\delta^{18}O$ values in Atacama nitrates range from +40 to +60 ‰ (Böhlke *et al.,* 1997; Michalski *et al*., 2004; Melchiorre *et al.,* 2018; Figure 3.2), reflecting an equilibrium value with local meteoric water, rather than its original atmospheric signature, overwriting any isotope signature during microbial denitrification This occurs because during microbial processes such as denitrification and nitrification, oxygen atoms in intermediate nitrogen species (e.g., nitrite, NO_2^-) can exchange with oxygen from water (H_2O). Because water is the dominant oxygen-bearing species in the system, this exchange can significantly alter the original oxygen isotope composition of nitrate, decreasing the $\delta^{18}O$ values of residual nitrate, because Atacama local water (mainly derived from snowmelt) has relatively negative $\delta^{18}O$ signatures (Reich and Bao 2018). However, Reich and Bao (2018) do not present geochemical evidence that could corroborate this proposed mechanism.

3.3 Nitrogen Isotopes

Nitrogen constitutes about 78% of the present-day atmosphere, and more than 99% of Earth's surface nitrogen exists as atmospheric N_2 or dissolved N_2 in the ocean. However, significant nitrogen reservoirs also reside in the crust and mantle (Figure 3.3; Hoefs, 2018; Li, 2024).

Nitrogen has two stable isotopes, ^{14}N and ^{15}N, and its isotopic composition is expressed as $\delta^{15}N$ (equation 3.1). The $\delta^{15}N$ values differ among Earth's major reservoirs—mantle, crust, and atmosphere (Figure 3.3)—allowing nitrogen isotopes to serve as tracers of mantle-surface exchange processes, including subduction and volcanism (Li, 2024).

Atmospheric nitrogen is composed of 99.63% of ^{14}N, and 0.37% of ^{15}N (Hoefs, 2018), totalling approximately $4x10^{18}$ kg N with a $\delta^{15}N$ = 0‰ by definition. The upper mantle is isotopically depleted in ^{15}N relative to the atmosphere, with $\delta^{15}N$ values between -10 and 0‰, and a global average near -5‰. In contrast, crustal material is typically enriched in ^{15}N, showing $\delta^{15}N$ value around +6‰ (Figure 3.3; Li, 2024). Nevertheless, some crustal rocks exhibit negative values as low as -7‰ (Liu *et al.,* 2023 in Li, 2024).

The flux of nitrogen between the crust and mantle has likely varied through geological time, influencing the composition and evolution of the atmosphere. Mantle nitrogen is released to the surface primarily via volcanism, whereas subduction zones act as the main pathway returning nitrogen to the mantle (Li, 2024).

Atmospheric N_2 is the least chemically reactive nitrogen species due to its strong N≡N triple bond. To participate in the nitrogen cycle, N_2 must first be converted into more reactive forms such as NO_3^-, NO_2^-, NH_3, and NH_4^+. Both biotic and abiotic processes can drive this conversion, and these transformations are recorded in nitrogen isotope fractionation (Hayes, 2004; White, 2015; Sharp, 2017; Hoefs, 2018).

Fractionation during these processes produces diagnostic $\delta^{15}N$ variations that reveal nitrogen sources and transformation pathways.

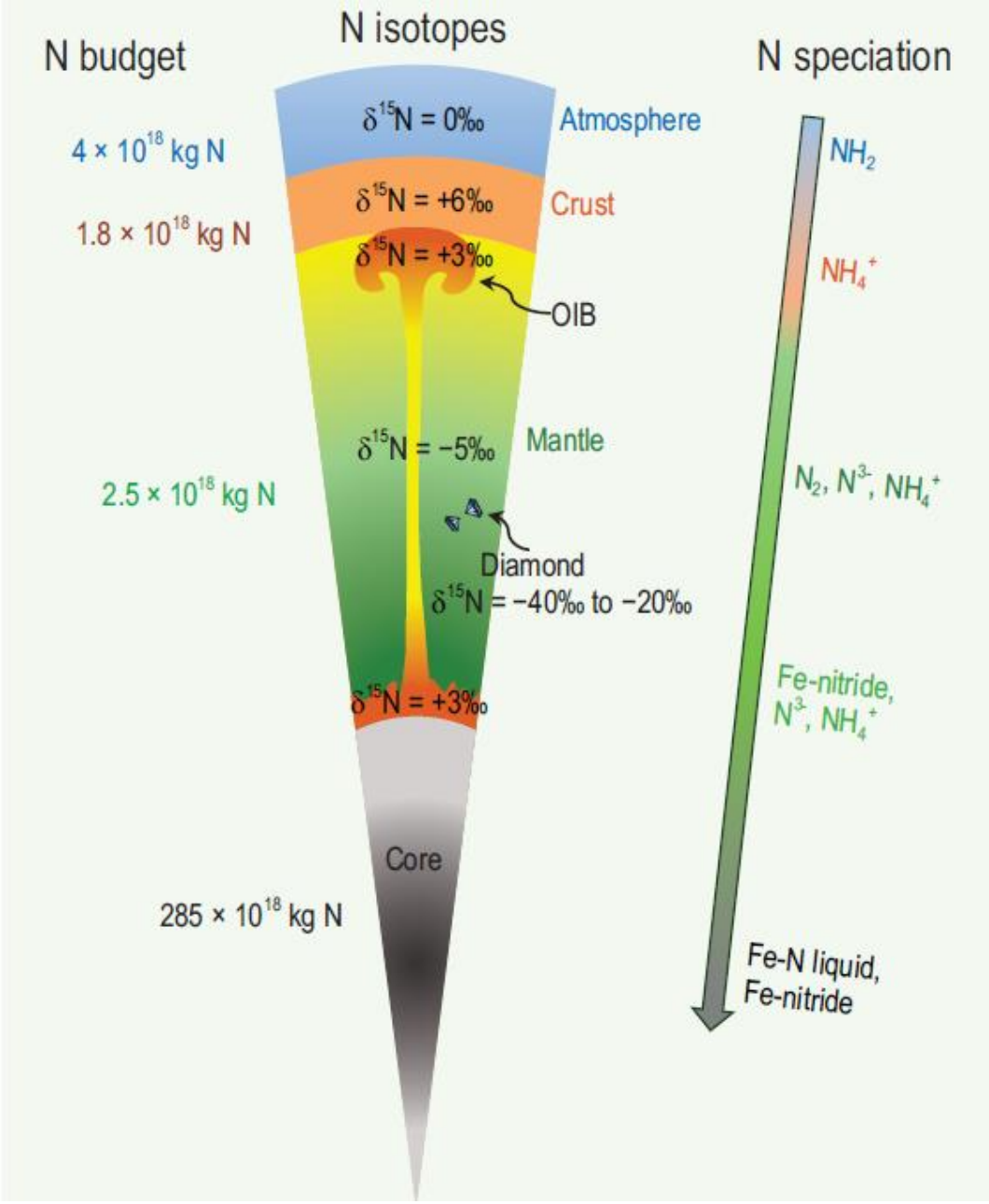

Figure 3.3: The nitrogen budget, isotope composition, and speciation of Earth's different reservoirs. The figure is not to scale and is taken from Li (2024).

The main biological processes that fractionate nitrogen isotopes are fixation, nitrification, and denitrification.

Fixation converts unreactive atmospheric N_2 into reactive nitrogen species (e.g., ammonium: NH_4^+, nitrate: NO_3^-), primarily through bacterial activity. The resulting products typically have $\delta^{15}N$ values between -2 and +2‰, indicating minimal isotopic fractionation (Casciotti, 2009; Hoefs, 2018).

Nitrification is a multi-step oxidation process mediated by specialized autotrophic organisms, generating nitrogen oxides as intermediates and nitrate as the final product. It proceeds via two partial reactions, oxidation by *Nitrosomas*:

$$NH_4^+ \rightarrow NO_2^- \tag{3.14}$$

and oxidation by *Nitrobacter*:

$$NO_2^- \rightarrow NO_3^- \tag{3.15}$$

The first oxidation reaction (3.13) is comparatively slow, whereas the second (3.14) proceeds much faster. As a result, most of the nitrogen isotope fractionation occurs during the slow oxidation of ammonium (3.13). The residual nitrate typically results in $\delta^{15}N$ values between -3 to +5‰ (Casciotti, 2009). The second oxidation step exhibits an inverse kinetic isotope effect, producing a nitrate depleted in ^{15}N ($\delta^{15}N \approx$ -13‰) as oxidation progresses (Casciotti, 2009).

Denitrification is also a multi-step reduction process, during which nitrate is biologically reduced through several intermediate nitrogen species. It typically occurs in poorly aerated soil and suboxic aquatic environments, leading to an enrichment in ^{15}N in the residual nitrate as its concentration decreases. Denitrification produces significant isotope fractionation, leading to residual nitrate with $\delta^{15}N$ up to 30‰ (Casciotti, 2009; Hoefs, 2018).

Anammox (anaerobic ammonium oxidation) is another dissimilatory pathway, involving the reaction of ammonia with nitrite to form dinitrogen gas, the dominant nitrogen loss mechanism in oxygen-minimum-zone waters (Hoefs, 2018):

$$NH_4^+ + NO_2^- \rightarrow N_2 + 2H_2O \tag{3.16}$$

This reaction (3.16) produces isotope fractionation similar in magnitude to that of denitrification, generating $\delta^{15}N$ values up to 38‰ (Casciotti, 2009).

Another way to fixate nitrogen is through lightning fixation from storms or volcanic activity. Volcanic lightning represents an important abiotic nitrogen fixation mechanism (see Section 3.2), producing NO_x species with $\delta^{15}N$ values between -6 and +15‰ (Aroskay *et al.,* 2024), while atmospheric nitrate typically exhibits $\delta^{15}N$ between −15 and +10‰ (Patris *et al.*, 2007; Morin *et al.*, 2009; Savarino *et al.*, 2013; Reich and Bao, 2018).

Currently, anthropogenic activities such as fossil fuel combustion dominate global NO_x production. The $\delta^{15}N$ values of nitrate derived from pollution are typically similar to those of the nitrogen source, as the high combustion temperatures in vehicles and power plants produce only minimal isotope fractionation (Hoefs, 2018).

In Atacama nitrate deposits, $\delta^{15}N$ values often cluster between -5 and +5‰ (Figure 3.2A; Böhlke *et al*., 1997; Michalski *et al.,* 2004; Melchiorre *et al*., 2018), interpreted as consistent with an atmospheric origin that has undergone limited denitrification and evaporation (Michalski *et al.,* 2004; Pérez-Fodich *et al.,* 2015). This minimal biological overprinting and limited post-depositional alteration imply that much of the nitrogen preserves its original atmospheric signature (Reich & Bao, 2018). Combined analysis of $\delta^{15}N$, $\delta^{18}O$, and $\Delta^{17}O$ on Atacama nitrates helps distinguish between primary atmospheric deposition and biologically recycled nitrogen.

3.4 Sulfur Isotopes

Sulfur is an important constituent of Earth's lithosphere, biosphere, hydrosphere, and atmosphere. Its isotope geochemistry characteristics are analogous to those of nitrogen, because it occurs in reduced and oxidized forms, undergoing different oxidation states because of biological processes (Sharp, 2017).

Sulfur has four stable isotopes ^{32}S, ^{33}S, ^{34}S, and ^{36}S, of which ^{32}S, and ^{34}S are the most abundant. Because of this, $^{34}S/^{32}S$ and $^{32}S/^{32}S$ are the common ratios measured of sulfur and are valuable for tracing sulfate origins and their coupling to nitrogen and oxygen cycles. (Sharp, 2017).

Sulfate (SO_4^-) is the most dominant ion present in the Atacama Desert soils (Ericksen, 1981, 1983; Voigt *et al.,* 2020), commonly occurring as $CaSO_4$, and less frequently as Na_2SO_4 in the subsurface because its higher solubility (-300 g L^{-1} at 20°C; Willmes, 1993; Voigt *et al.,* 2020; Klipsch *et al.,* 2023). Together with nitrates (NO_3^-) and chlorides (Cl^-), sulfate plays an important role in soil dynamics and is the major component in Atacama nitrate deposits (Ericksen, 1981; Chong, 1994; Chong *et al.,* 2020).

Sulfur isotopes ($\delta^{34}S$ values) reflect sulfur source and redox history (Sharp, 2017; White, 2015). In the Atacama Desert, $\delta^{34}S_{SO4}$ values allow the identification between primary atmospheric sulfate (PAS) and secondary atmospheric sulfate (SAS) from marine and atmospheric sources. PAS corresponds to oxidized sulfate directly emitted from its sources to the atmosphere (e.g., marine sea spray). SAS belongs to pre-industrial reduced sulfur gases from volcanic (SO_2, H_2S) or marine (dimethyl sulfide, DMS) sources that are oxidized in the atmosphere (Klipsch *et al.,* 2023). Marine PAS exhibits a $\delta^{34}S$ value of +21.15‰ (Johnston *et al.,* 2014), whereas volcanic SAS falls in the range between -7 and +10‰, and marine SAS (DMS) between +18.9 and +20.3‰ (Klipsch *et al*., 2023). Biological cycled sulfate involves reduction by plants (Koprivova and Kopriva, 2016) or by microorganisms in anaerobic environments (Wankel *et al.,* 2014), and subsequently abiotically or biotically re-oxidation (Klipsch *et al*., 2023). The biological cycled sulfate isotope composition depends on the $\delta^{34}S$ of the initial sulfate, covering a large range of $\delta^{34}S$ values, from 0‰ to 27.3‰. Consequently, the range of $\delta^{34}S$ of cycled sulfate is not further defined, and the use of triple oxygen isotopes in sulfate is necessary to identify biological recycled sulfate, water availability, and mass independent fractionation of SAS (Figure 3.4; Klipsch *et al*., 2023).

In the Atacama Desert, there are four endmembers that contribute to the sulfate composition in the soils. (1) Oxidation from reduced volcanic gases (SAS), delineated by samples from high Coastal Cordillera (> 1200 m a.s.l.); (2) marine aerosols from dissolved sulfate in the ocean (PAS) and from DMS oxidation in the atmosphere (SAS_{DMS}), defined by samples from low Coastal Cordillera samples (< 1200 m a.s.l.); (3) biological recycled sulfate (BRS), delimit by salar samples; and hydrothermal sulfate pointed by an unique negative trend of thenardite (Na_2SO_4) samples in a multi-isotope plot, tending toward zero in $\Delta^{17}O$ and low $\delta^{18}O$ and $\delta^{34}S$ (Klipsch *et al*., 2023). When this trend is extrapolated to $\Delta^{17}O$ = 0‰, it yields a hypothetical hydrothermal

endmember represented by hydrothermal sulfate deposits from El Tatio hot spring in the Atacama Precordillera, with $\delta^{34}S$ from -9.7 to +2.6‰ (Figure 3.4; Cortecci *et al.,* 2005; Klipsch *et al*., 2023). Thus, when analyzing $\delta^{34}S$ in sulfates from nitrate deposits, the hydrothermal contribution can be identified. Nevertheless, triple oxygen isotopes in sulfates should be analyzed for differentiation of hydrothermal input and SAS.

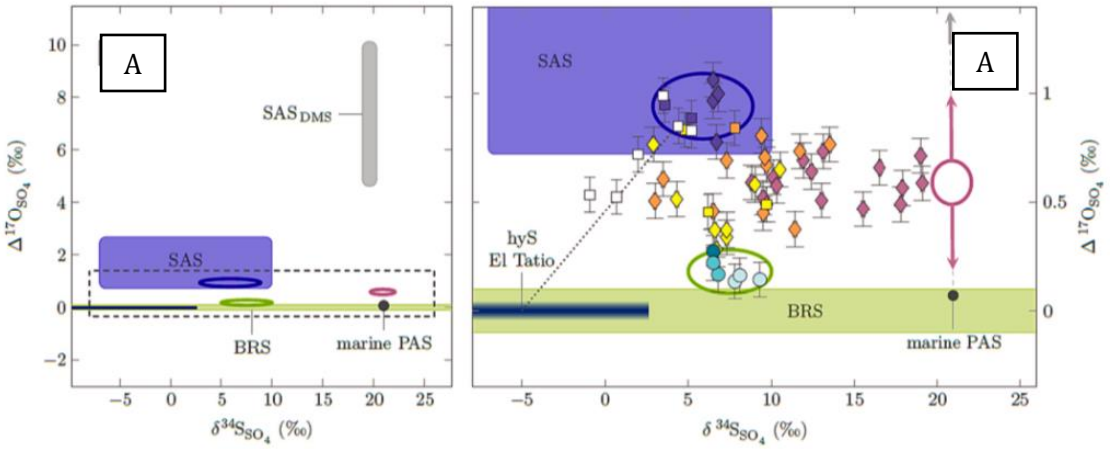

Figure 3.4: Sulfate endmembers from Atacama soils. A) $\Delta^{17}O_{SO4}$ versus $\delta^{34}S_{SO4}$. SAS indicates secondary atmospheric sulfate originating from volcanic emissions, SAS_{DMS} SAS originated from oxidation of biogenic sulfur gases (e.g., DMS), marine PAS corresponds to dissolved marine sulfate, and BRS refers to biological recycled sulfate (BRS). Additionally, HyS belongs to hydrothermal sulfate from El Tatio geothermal field (Cortecci *et al*., 2005) with an expected $\Delta^{17}O_{SO4}$ of ~ 0‰. B) Enlarged section from A. For interpretation of the references to colour in this figure legend, the reader is referred to the source of the Figure: Klipsch *et al.* (2023).

4 Objectives

The main objective of this thesis is to build a multi-source genetic model that integrates geological, geochemical, and isotopic evidence to explain the origin and evolution of the different types of nitrate deposits in the Atacama Desert.

Accordingly, this study aims to expand existing frameworks—such as Pérez-Fodich *et al.* (2014), and Reich and Bao (2018)—through the integration of new field observations, mineralogical characterization, and multi-isotopic analyses.

This research builds on prior studies that suggest that Atacama nitrates originate primarily from atmospheric deposition (Böhlke *et al.,* 1997; Michalski *et al*., 2004; Reich and Bao, 2018), with possible contributions from volcanic emissions and lightning fixation (Aroskay *et al.,* 2024). The diversity of deposit types—sedimentary, veins in sedimentary deposits, veins in rocks, neptunic dykes, and salt flats—reflects post-depositional remobilization, evaporation, hydrothermal activity, and tectonic reactivation operating over geological time. This study, therefore, seeks to determine how an atmospheric source of nitrate can lead to a wide variety of deposit morphologies with their isotopic signatures through diverse geological processes.

To achieve this objective, the following specific goals are established:

- Characterize the geochemical composition (major and trace elements) of soils, sediments, veins, saline crusts, and host rocks to understand the distribution and enrichment of soluble salts associated with nitrate mineralization.
- Evaluate triple-oxygen isotope ratios ($\delta^{17}O$, $\delta^{18}O$, $\Delta^{17}O$) in different deposit types to identify mass-independent oxygen anomalies indicative of atmospheric photochemical origin, and to analyze subsequent isotopic modification through interaction with local meteoric and hydrothermal waters.
- Determine nitrogen isotope compositions ($\delta^{15}N$) to distinguish between atmospheric, volcanic, and possible biological influences in the nitrogen cycle of the Atacama nitrates.
- Analyze sulfur isotopes ($\delta^{34}S$) in sulfates associated with nitrates to assess the role of hydrothermal or fumarolic processes in the genesis and alteration of these deposits.

- Integrate geological setting and isotopic results to develop a comprehensive model describing the geological cycle of Atacama nitrate deposits, from primary atmospheric deposition to secondary hydrothermal remobilization and vein formation.

The foundations of this study:

(1) Primary atmospheric deposition of nitrate in desert environments (Böhlke *et al.,* 1997; Michalski *et al*., 2004); and

(2) focusing and groundwater transport in aquifers followed by evaporative enrichment in endorheic basins (Pérez-Fodich *et al*., 2014; Reich & Bao, 2018).

These processes form the sedimentary deposit (type-i; Ericksen, 1981; Chong, 1994).

The working hypothesis of the present study was built on the extensive field evidence by Chong (1994) suggesting a volcanogenic role in the deposition of the vein deposits, which constitute so far the richest nitrate ores. However, it also must account for the ubiquitous $\Delta^{17}O$ anomaly that implies an atmospheric origin.

The results presented here strongly suggest that a second stage of this super-cycle would involve hydrothermal and tectonic reactivation of buried nitrate-rich sequences, leading to remobilization and emplacement of nitrate-bearing fluids into fractures and veins (type-iic deposits).

This model acknowledges that nitrate deposits may have undergone multiple cycles of formation, destruction, and redeposition associated with tectonic activity, hydrothermal circulation, and climatic oscillations over geological time.

Finally, this study provides new insights into the paleoclimate evolution of the hyperaridity in the Atacama Desert, establishing analogies with other nitrate-bearing deserts (e.g., Mojave, Tupan-Hami, Namib) and offering a comparative framework for the study of biosignatures and oxidized nitrogen compounds on Mars.

5 Field Work and Sampling

Systematic field campaigns were carried out between 2021 and 2025 across the Tarapacá and Antofagasta Region, northern Chile, within the framework of the CRC1211 “Earth Evolution at the Dry Limit” multidisciplinary project. The objective was to collect representative materials from distinct geological and geochemical settings, including all recognized nitrate deposit types (type-i, type-iia, type-iib, type-iic, and type-iii).

Fieldwork involved detailed geological observations, photographic documentation, and the sampling of diverse materials, including soils, host rocks, mineralized veins, dykes, salt crusts, and speleothems. These samples provide the foundation for the mineralogical, chemical, and isotopic analyses presented in later chapters, allowing a direct link between field observations and laboratory interpretations.

Sampling sites were selected to represent a range of geomorphological and structural environments, from endorheic basins and alluvial plains to fault-controlled hydrothermal zones. In the Tarapacá Region, samples were obtained from historical nitrate “oficinas” such as California, Santa Rita, San Francisco, Asturias, and Germania. In the Antofagasta Region, sampling focused on Cerro Birrete, Oficina Domeyko, and Aguas Blancas, covering all types of nitrate deposits.

A detailed summary of sample locations, lithological descriptions, and deposit types is provided in Appendix Table A1.1. The collected materials were analyzed for major and trace elements to characterize elemental associations, while triple-oxygen ($\delta^{17}O$, $\delta^{18}O$, $\Delta^{17}O$) and nitrogen ($\delta^{15}N$) isotopes were measured in nitrates to distinguish atmospheric, volcanic, and post-depositional processes. Sulfur isotopes ($\delta^{34}S$) in sulfates were used to evaluate possible hydrothermal inputs. The methodology and results are discussed in the next chapters.

Together, these field and analytical datasets form the empirical basis for reconstructing the geological evolution and geochemical cycling of nitrate deposits in the Atacama Desert, connecting field-scale geological context with isotopic and geochemical evidence.

5.1 Tarapacá Region

5.1.1 Oficina California (19,68°S / 69,87°W)

- Type of nitrate deposit: Type-i, type-iib, and type-iic.

- Nitrate description: Type-i deposits occur as cement of breccia and sandstone from alluvial deposits (black caliche; Table A3.1), found at 2 to 3 m depth (Figure 5.1A-B). Type-iib deposits belong to neptunic dykes 15 cm thick cutting breccia and nitrate veins, occurring in depth levels at the cave, to the top reaching the surface level (Figure 5.1C). And type-iic belong to nitrate veins and mantos with a thickness from 10 to 50 cm, white color, and massive and fibrous in habit. They are cutting through a breccia and found at depth levels in caves (Figure 5.1C).

- Other salts: The secondary associated phases include sulfates, chlorates, iodates, borates, chromates, and strontium and lithium-bearing salts (Table A3.1).

- Host rock and alteration: Continental sedimentary rocks, including sandstones in alluvial fan planes and polymictic matrix-supported breccia as the host rock of veins and mantos. Sandstones are generally brown with light red coloration due to oxidation and are moderately to well cemented. Breccia with subangular clasts ranging from 2 to 30 cm. The sand matrix of the breccia is white to grey, with some red coloration, and moderately to well-cemented by nitrates and other salts. The breccia is poorly sorted and immature in texture and composition and presents low oxidation.

- Stratigraphic and chronologic correlation of the host rock: The continental sedimentary rocks described above are compared with the Gravas de Alto Hospicio (Oligocene-Pliocene; Vásquez and Sepúlveda, 2013).

- Depositional environment of the stratigraphic sequence: The sedimentary rocks were deposited in an alluvial setting characterized by episodic water flows, producing interbedded layers of gravel, sand, and mud. The gypsum-cemented strata (chuca layer from type-i deposits) were interpreted as the development of paleosoils, suggesting that these deposits would have accumulated under arid climatic conditions (Vásquez and Sapúlveda, 2013).

- Structural Geology of the area: The reactivation of normal faults NS oriented would have generated hemigrabens, which were also affected by reverse faults with E-W and N-S orientation, creating the necessary structural depression for the accumulation of

these sediments. The east-west-oriented fractures and faults would have allowed the circulation of groundwater loaded with dissolved salts from the Central Depression and the Precordillera (Vásquez and Sapúlveda, 2013).

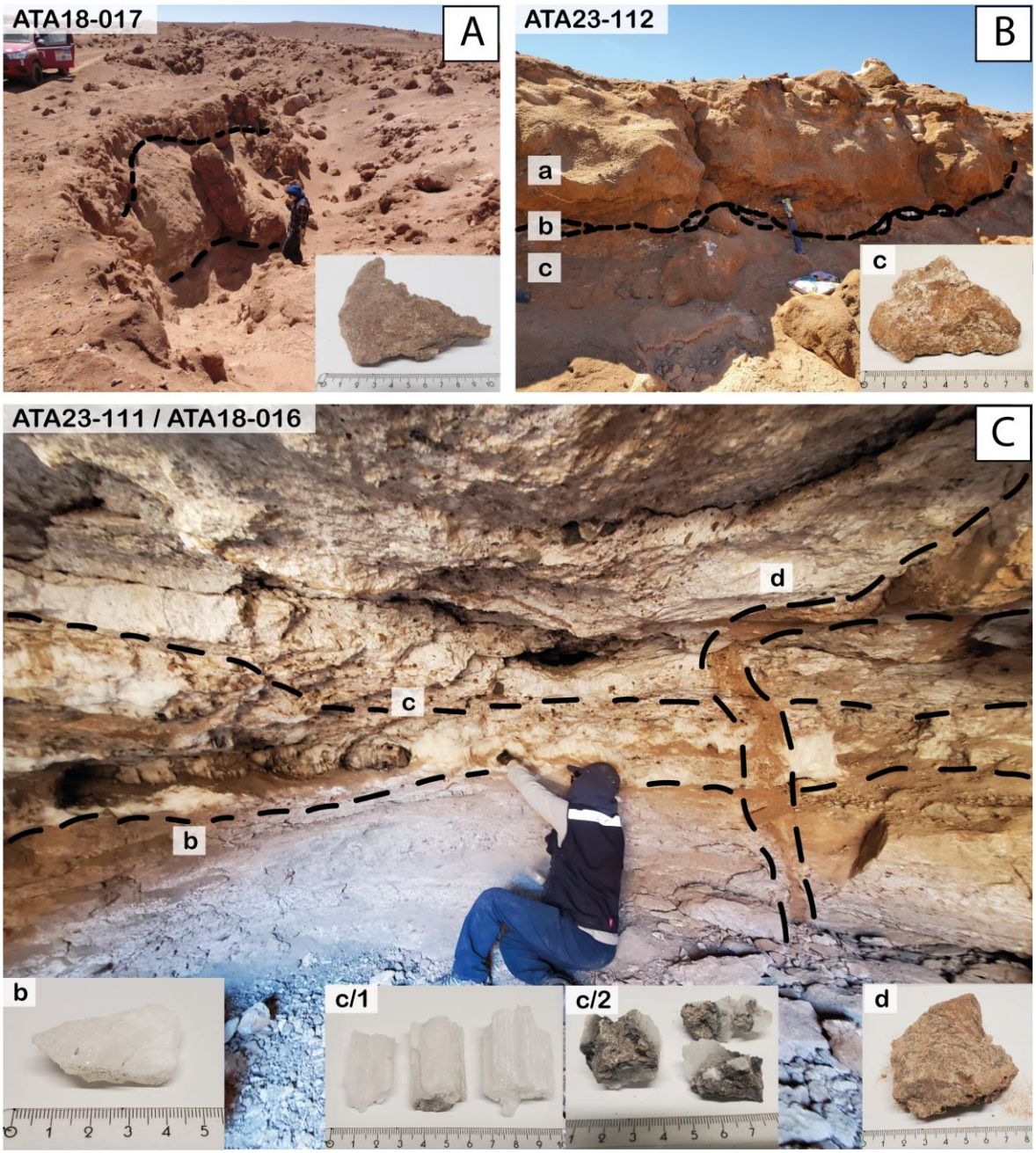

Figure 5.1: Types of nitrate deposits occurring in Oficina California. A) Samples ATA18-017, and B) ATA23-112 represent the caliche layer of a sedimentary profile (type-i deposit). C) Mining cave exposing a manto of white caliche cutting through a matrix-supported breccia (type-iic deposit; ATA23-111b, 111c/1, 111c/2, and ATA18-016), which in turn is cut by a neptunic dyke (type-iib deposit). The small photographs refer to the rock sample taken for chemical and isotopic analysis. The hammer used as a scale for the pictures is approximately 30 cm.

5.1.2 Oficina Santa Rita (19,70°S / 69,97°W)

- Type of nitrate deposit: Type-iib, and type-iic.

- Nitrate description: Type- iib occurrences consist of neptunic dykes up to 10 cm thick that intersect the host rock near the surface (Figure 5.2C). Type-iic deposits occur as nitrate veins cutting through grey limestone and calcareous shale at deep levels inside the cave. The vein thickness covers a range between 20 and 100 cm, with different colorations, mostly white, but also yellow and blue. Different habits can be appreciated in these structures, from massive to fibrous (Figure 5.2D-I). The yellow coloration is given by the presence of iodine species, and the blue given by potassium (Table A3.1).

- Other salts: Associated phases include sulfates, chlorates, iodates, borates, bromides, chromates, and strontium and lithium-bearing salts (Table A3.1).

- Host rock and alteration: Marine sedimentary. Intercalation of grey limestone with calcareous shale with intensive oxidation and fracturing, increasing to the top (Figure 5.2). In the field, this alteration is recognized as red-colored zones with intensive fracturing.

- Stratigraphic and chronologic correlation of the host rock: The host rock sequence corresponds to the El Godo Formation (Bajocian-Oxfordian; Vásquez and Sepúlveda, 2013).

- Depositional environment of the stratigraphic sequence: Back-arc marine basin, deep environment, contemporary with submarine volcanism (Vásquez and Sepúlveda, 2013). Altered by tectonic and hydrothermal activity, generating oxidation and vein filling.

- Structural Geology of the area: Angela Fault with NW-SE orientation, that brings the stratified rocks on the uplifted side into contact with the nitrate and plain deposits on its more depressed side (Vásquez and Sepúlveda, 2013). The nitrate veins exhibit evidence of ductile deformation, indicating multiple deformation and fluid flow episodes during post-depositional tectonism within this fault zone.

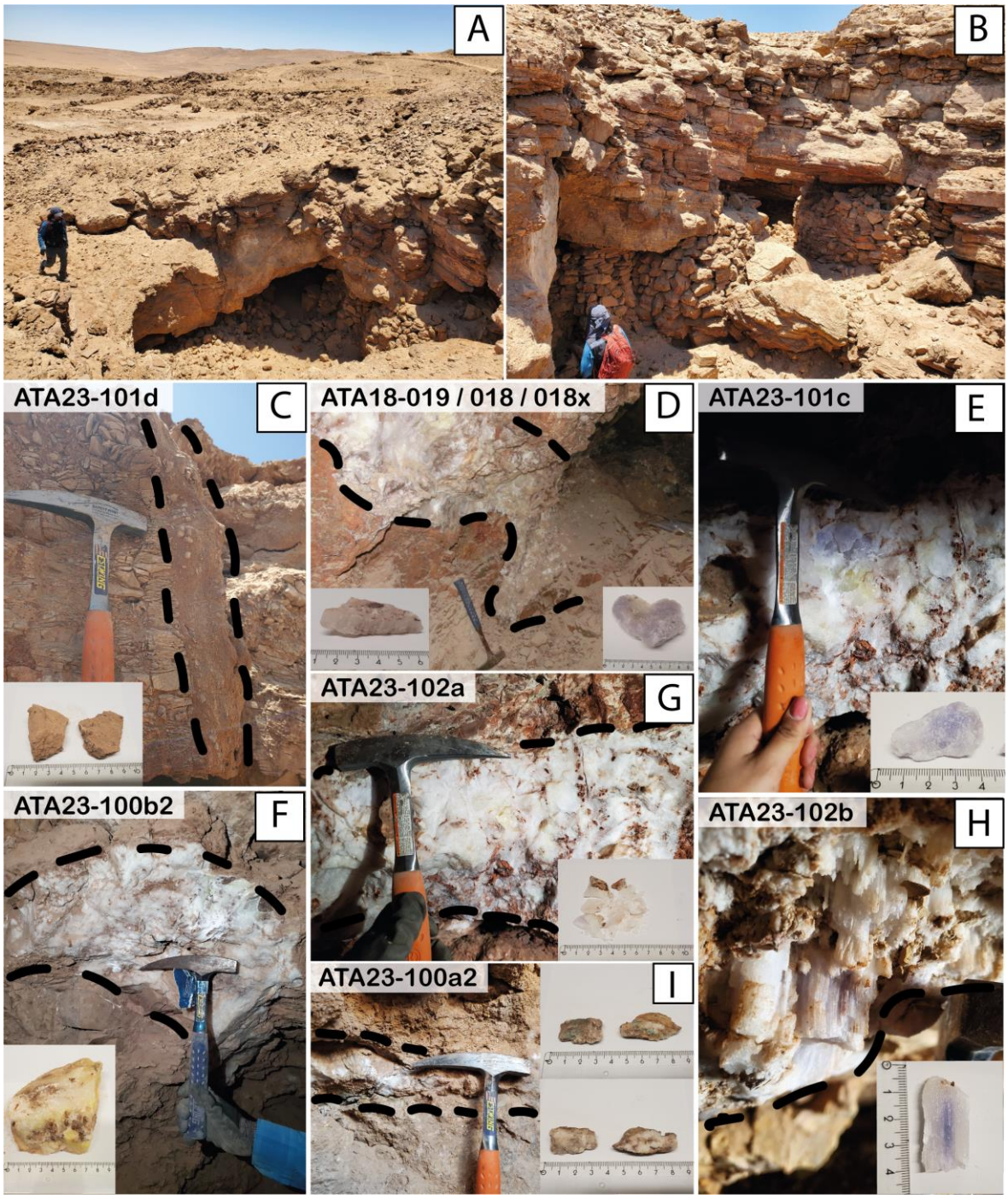

Figure 5.2: Type of nitrate deposit taking place at Oficina Santa Rita. A) Landscape morphology from the area, reworked by mining. B) Entrance to the cave in the mining site. C) Neptunic dyke cutting a brecciated limestone (type-iib deposit). D-H) white, yellow, and blue veins cutting a Jurassic limestone (type-iic deposit). Sample names are indicated in each photograph. The small photographs refer to the rock sample taken for chemical and isotopic analysis. The hammer used as a scale for the pictures is approximately 30 cm.

5.1.3 Oficina San Francisco (19,70°S / 69,93°W)

- Type of nitrate deposit: Type-i.

- Nitrate description: Nitrates occur as cement in sandstone and fractured limestone matrices (black caliche; type-i deposits). The material is dense, fine-grained, and displays a compact gray coloration with occasional darker laminations (Figure 5.3). The cementation is pervasive, forming continuous crusts that locally fill intergranular pores and small fractures, resulting in massive, indurated horizons with sharp contacts against the host rock.

- Other salts: carbonates, sulfates, chlorates, iodates, and minor strontium and lithium-bearing salts (Table A3.1). These minerals occur as fine intergrowths or dispersed inclusions within the nitrate cement. The carbonates also occur filling cracks of the host rock.

- Host rock and alteration: Continental and marine sedimentary sequences composed of grey-brown sandstone that is well-cemented and fine-grained, together with fractured grey limestone exhibiting localized $CaCO_3$ veins and oxidation surfaces (Figure 5.3).

- Stratigraphic and chronologic correlation of the host rock: The sandstone unit corresponds to the Gravas de Alto Hospicio (Oligocene-Pliocene), whereas the limestone belongs to the Santa Rosa Formation (Oxfordian; Vásquez and Sepúlveda, 2013).

- Depositional environment of the stratigraphic sequence: The sandstone was deposited in an alluvial setting characterized by episodic flows, producing interbedded layers of sand and mud, while the limestone represents deposition in a shallow back-arc marine basin typical of a carbonate platform. Subsequent tectonic deformation produced fracturing and minor veining of calcite (up to 1 cm thick), reflecting fluid circulation through permeable zones.

- Structural Geology of the area: Angela Fault with NW-SE orientation, that brings the stratified rocks on the uplifted side into contact with the nitrate and plain deposits on its more depressed side (Vásquez and Sepúlveda, 2013). Locally, the fault zones act as a conduit for fluid migration.

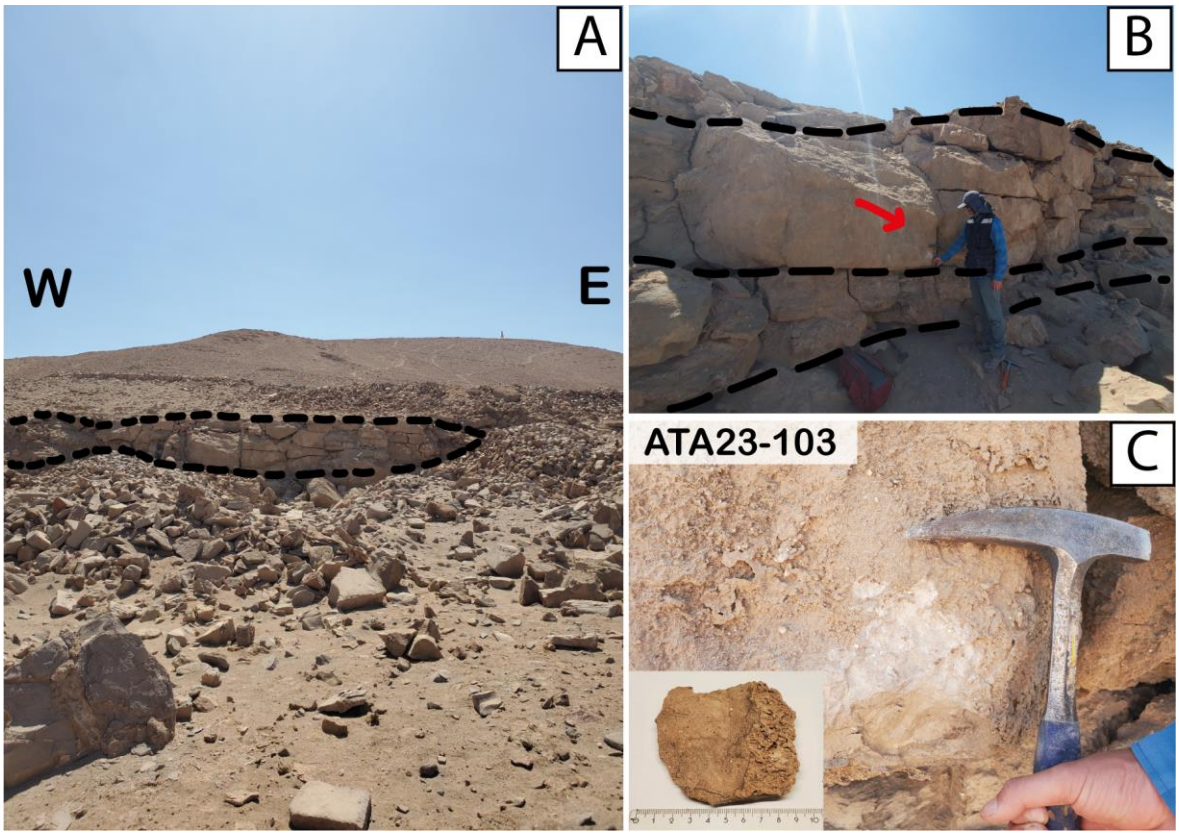

Figure 5.3: Types of nitrate deposits in Oficina San Francisco. A) The landscape of the geological site shows the outcrop of a distal alluvial fan. B) Closer view of the sedimentary sequence of A, where 2 layers can be identified, the upper one belongs to a well-cemented sandstone, and the lower one to a fractured limestone. C) Shows a closer picture of B, in the red arrow's direction, where the sample ATA23-103 was taken.

5.1.4 Oficina Asturias (19,82°S / 69,87°W)

- Type of nitrate deposit: Type-i, and type-iia.

- Nitrate description: Type-i deposits consist of white to reddish, powdery, and soft nitrate accumulation that fills fractures near the surface, typically developed at the top of a brecciated layer derived from an alluvial fan deposit (Figure 5.4D and E). Type-iib deposits, in contrast, are characterized by white fibrous nitrate mantos that are poorly consolidated and locally friable, with thicknesses reaching up to 15 cm (Figure 5.4C). These mantos are generally subparallel and occur approximately one meter below the surface, cutting through unconsolidated alluvial sediments.

- Other salts: The associated phases include sulfates, chlorates, borates, and minor strontium-bearing salts (Table A3.1).

- Host rock and alteration: Continental and marine sedimentary. Brecciated limestone with moderate oxidation and highly fractured. Poorly cemented, the matrix is partly wet, red in color due to oxidation, and the sequence is cut by unconsolidated thin nitrate veins.

- Stratigraphic and chronologic correlation: The host rock corresponds to the Santa Rosa Formation (Oxfordian; Vásquez and Sepúlveda, 2013).

- Depositional environment of the host rock: Proximal alluvial fan environment with active circulation of saturated fluids. Back-arc marine basin, shallow environment, characteristic of a carbonate platform. Fractured by tectonic activity, giving rise to the formation of nitrate veins due to the circulation of saturated fluids.

- Structural Geology of the area: Angela Fault with NW-SE orientation, that brings the stratified rocks on the uplifted side into contact with the alluvial deposits (Figure 5.4A and B; Vásquez and Sepúlveda 2013).

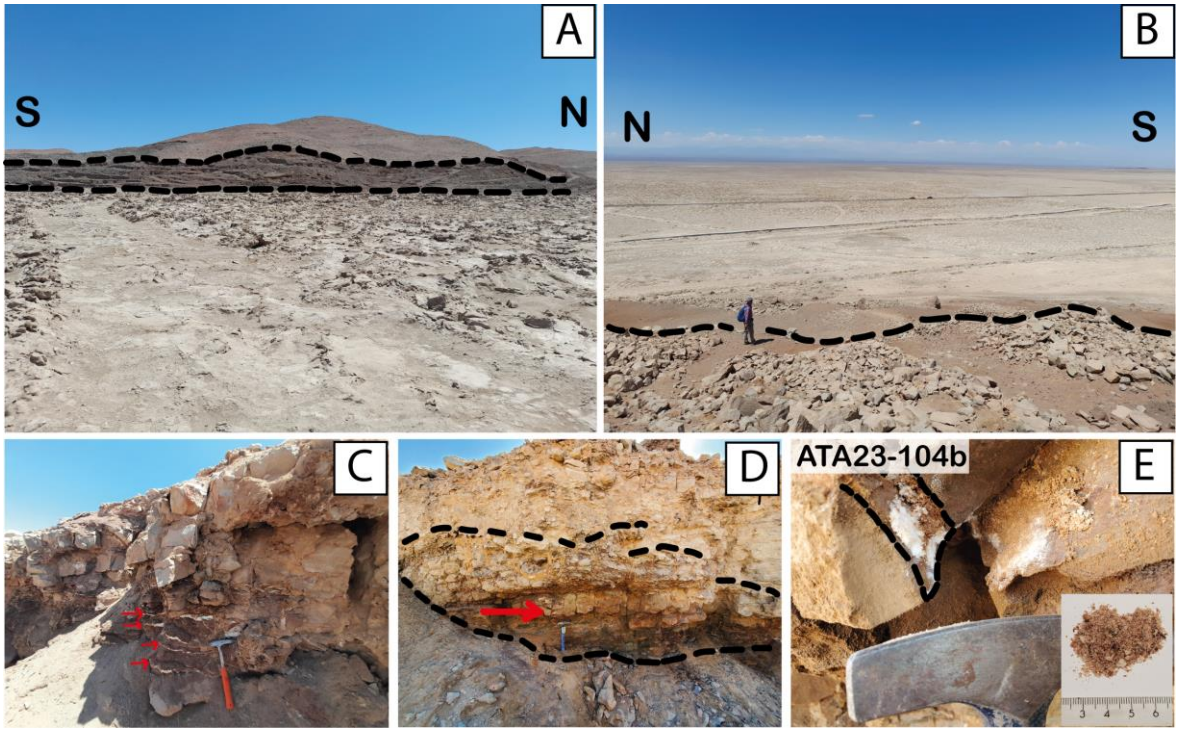

Figure 5.4: Types of nitrate deposits occurring in Oficina Asturias. A) The landscape of the geological site shows the outcrop of a proximal alluvial fan. B) Another landscape photography, but with a view to the east, showing the flat topography of the saline deposits from the Pampa del Tamarugal. C) Closer view to the south of the sedimentary sequence shows a brecciated limestone with a fibrous nitrate vein to the bottom (red arrows), corresponding to type-iia deposits. D) Closer view to the north of the sedimentary sequence, where powdery soft white nitrate is filling the fractures of the brecciated limestone. The red arrow shows the place where the sample was taken. E) Detailed photography from D, where the powdery nitrate can be appreciated (Ata23-104b; type-i deposits). The small photographs refer to the rock sample taken for chemical and isotopic analysis. The hammer used as a scale for the pictures is approximately 30 cm.

5.1.5 Oficina Germania (19,89°S / 69,79°W)

- Type of deposit: Type-iib, and type-iic

- Nitrate description: Type-iib deposits consist of neptunic dykes that occur at or near the surface, cutting across volcanic breccia unity (Figure 5.5K-L). These dykes are typically narrow, planar to irregular in geometry, and infilled with fine-grained nitrate material, forming light-colored structures that contrast with the darker host rock. They commonly follow existing fracture networks and display a rugose, hard texture.

Type-iic deposits are represented by nitrate veins cutting brecciated andesite, reaching a thickness up to 30 cm (Figure 5.5C-J). These veins are mainly white in color, locally showing pale yellow associated with elevated iodine contents (Table A3.1). They mainly present massive and compact habit, and in some cases, fibrous textures are visible, reflecting episodic influxes of nitrate-bearing solutions during fracturing events.

- Other salts: Associated salts include chlorates, sulfates, iodates, borates, lithium, and strontium-bearing phases (Table A3.1).

- Host rock and alteration: The host rock is a volcano-sedimentary sequence, dominated by a brecciated andesite exhibiting strong oxidations and pervasive fracturing (Figure 5.5B, I, and M). The breccia clasts are subangular to angular, embedded in a reddish to brown matrix rich in iron oxides, giving the outcrop a distinct coloration. Hydrothermal alteration is evident in the form of hematite coatings on fracture surfaces, suggesting circulation of oxidizing fluids that contributed to both the brecciation and alteration of the rock.

- Stratigraphic and chronologic correlation of the host rock: The deposits is hosted within the Punta Barranco Formation (Berriasian-Albian; Vásquez and Sepúlveda, 2013).

- Depositional environment of the stratigraphic sequence: The overall depositional setting corresponds to a continental environment characterized by alluvial sedimentation in a small intra-arc basin, contemporaneous with active volcanism, later affected by tectonic and hydrothermal activity (Figure 5.5M-O; Vásquez and Sepúlveda, 2013).

- Structural Geology of the area: Angela Fault with NW-SE orientation, that brings the stratified rocks on the uplifted side into contact with the alluvial deposits (Figure 5.5A) (Vásquez and Sepúlveda 2013).

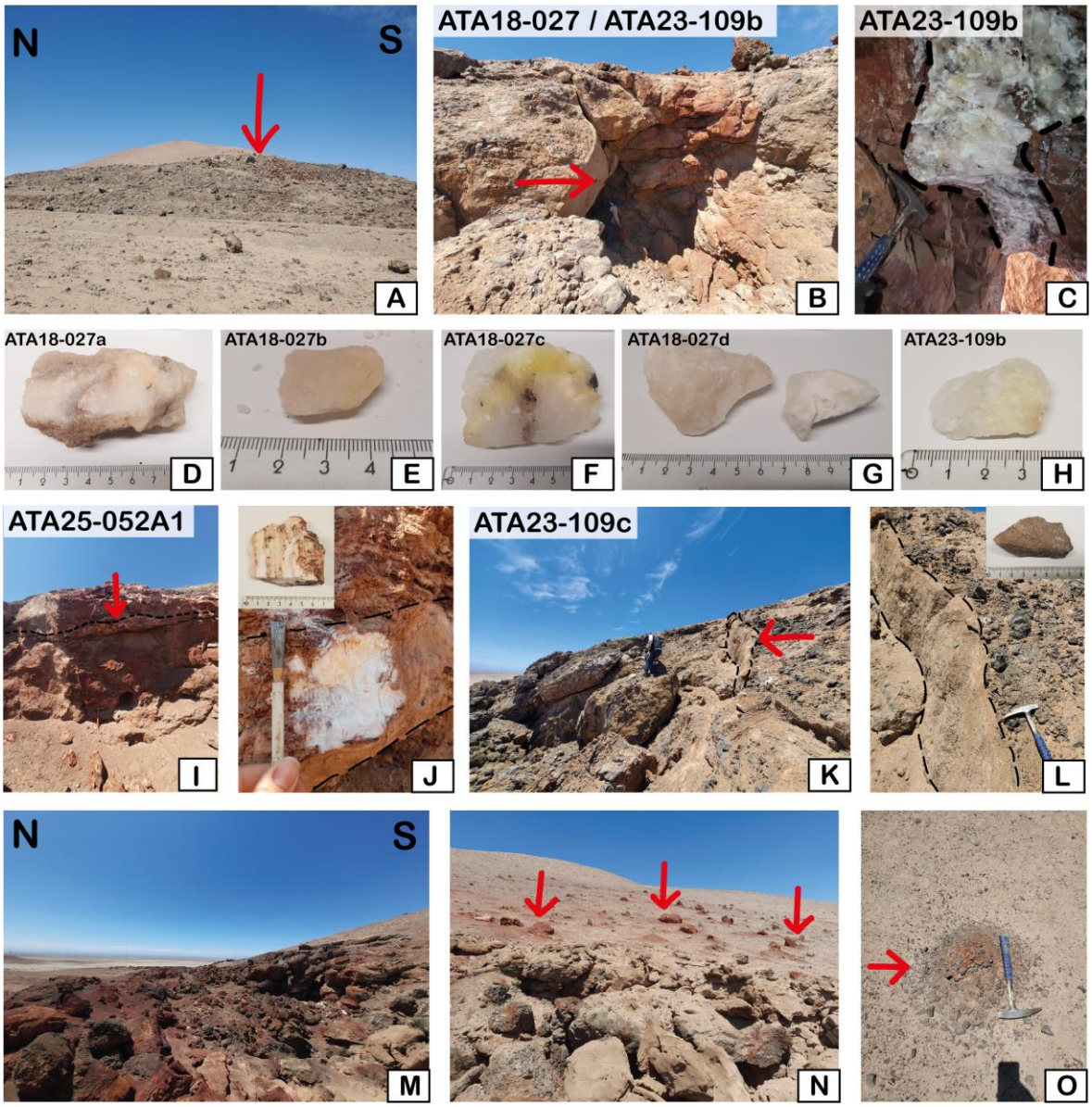

Figure 5.5: Types of nitrate deposits of Oficina Germania. A) Landscape view to the west, the red arrows show the location of B. B) Entrance to the cave (red arrow). C) White caliche vein cutting through a brecciated andesite in the roof of the cave. D to H) White and yellow caliche samples taken from the cave. I) Next to B, a white manto of nitrate cutting through an oxidized brecciated andesite. J) Closer view of the white manto of I, showing the fibrous habit of the white caliche. K) Another outcrop, located to the NW of outcrop B. The red arrow shows the neptunic dyke filling the fracture. L) A closer view from N, exposing the neptunic dyke. M and N) show the landscape view from the position in I, M) to the east, showing the intense oxidation in the area, and N) to the south of the hill, showing the occurrence of hydrothermal vents (red arrows). O) Closer view of one of the hydrothermal vents from N. Sample names are indicated in each photograph. The small photographs refer to the rock sample taken for chemical and isotopic analysis. The hammer used as a scale for the pictures is approximately 30 cm.

5.2 Antofagasta Region

5.2.1 Cerro Birrete (22,91°S / 69,77°W)

- Type of deposit: Type-i, type-iib, and type-iic

- Nitrate description: Type-i deposits occur as cementing material within fine to coarse-grained sandstones, forming the characteristic black caliche horizons at the base of the stratified alluvial sequences (Figure 5.6B and C). Type-iib occurrences comprise neptunic dykes that cut the volcano-sedimentary sequence, characterized by narrow structures filled with compact sediment cemented by nitrates and other minor salts (Figure 5.6J-L). Type-iic deposits include white, massive nitrate veins (Figure 5.6D), white to dark-grey massive lenses (Figure 5.6E), paleoconduits composed of mixed nitrate-sediment aggregates showing white-yellow coloration (Figure 5.6F). Additionally, both well-cemented grey and poorly cemented red-orange saline crusts occur along fault-controlled contact zones (Figure 5.6G-I), representing late-stage mineralization associated with capillary enrichment and fluid migration. In some outcrops, travertine veins cut through the sedimentary sequence (Figure 5.7A), indicating interaction between hydrothermal fluids and meteoric waters during late diagenetic stages.

- Other salts: The associated saline assemblage includes carbonates, sulfates, chlorates, iodates, borates, strontium, lithium, arsenic, and chromates (Table A3.1).

- Host rock and alteration: The host rock belongs to a volcano-sedimentary sequence, comprising horizontally stratified red sandstone and shale unit overlain by andesitic lava flows (Figure 5.6A, E, F). The sedimentary rocks exhibit variable degrees of oxidation, typically moderate to high, with iron-oxide staining. The andesitic units show brittle deformation and contain disseminated alteration minerals, suggesting localized hydrothermal overprinting.

- Stratigraphic and chronologic correlation of the host rock: The volcano-sedimentary sequence can be correlated to the Quebrada Mala Formation (Upper Cretaceous; Baeza & Astudillo, 2019).

- Depositional environment of the stratigraphic sequence: The unit represents alluvial and lacustrine hydrological systems that filled continental depositional centres, contemporaneously with active volcanism.

Figure 5.6: Types of nitrate deposits from the Cerro Birrete (CB) area. A) Panoramic view from the volcano-sedimentary sequence. B and C) Alluvial deposits (type-i) 15km close to CB. D) Andesitic lava cut by white veins (type-iic), 11 km northwest of A. E) Close view from A, showing lenses of white and black minerals cutting through the lacustrine sequence (type-iic). F) Paleoconduits in the lacustrine sequence. G) Well-cemented salt crusts emerging from the fault plane, 5 km northeast of A, and in H) same location as A. I) Orange and grey poorly cemented salts, emerging from the fault plane, close to G. J) Sandstone cut by neptunic dykes, 17 km northwest of A. K) Alluvial deposits cut by neptunic dykes, 6 km east of A. L) Limestones underlying imbricated conglomerates, cut by neptunic dykes, 5 km northeast of A.

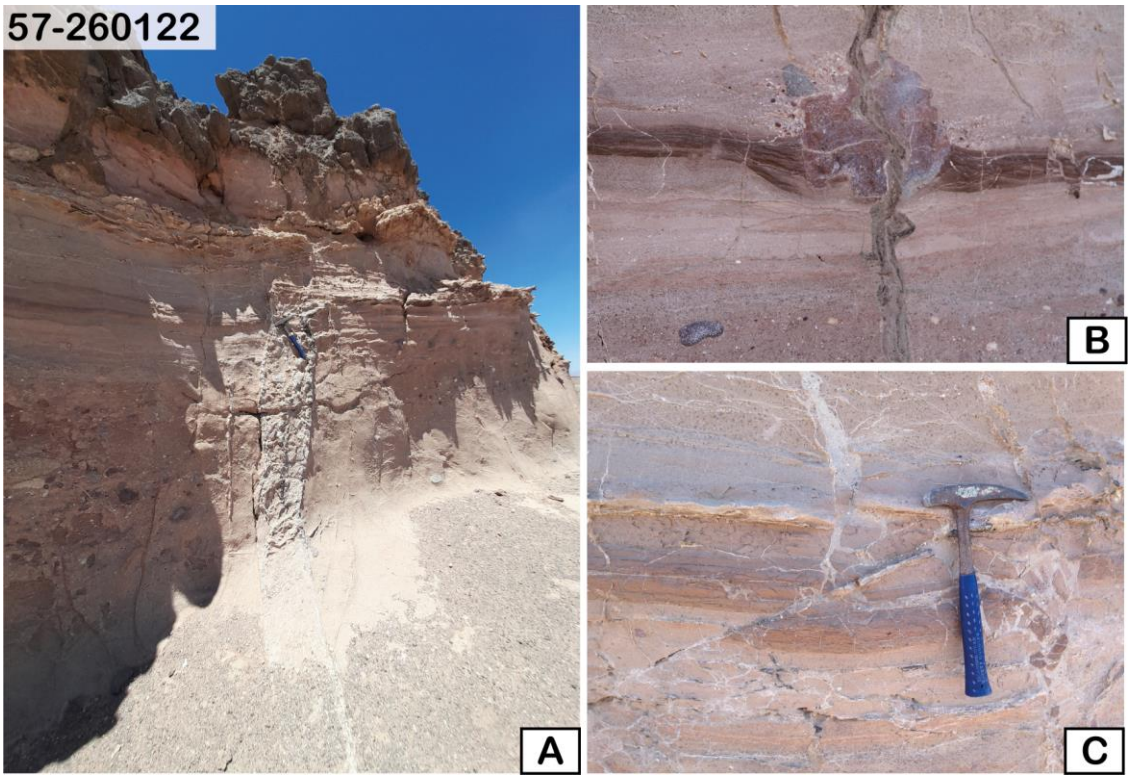

Figure 5.7: A) Travertine vein cutting the lacustrine sequence. B) Volcanic bomb in the lacustrine sediments, which in turn is cut by a neptunic dyke. C) Local reverse fault displacing the lacustrine sediments.

Volcanic bombs are frequently interdigitated with the sedimentary sequence, providing evidence of episodic pyroclastic input (Figure 5.7B). Subsequent tectonic fracturing facilitated the intrusion of unconsolidated sedimentary material, forming neptunic dykes that record syn-sedimentary deformation and later fluid circulation. (Figure 5.7B).

- Structural Geology of the area: The region is structurally controlled by the extensional reactivation of the Atacama Fault System, which generated a horst-and-graben morphology expressed as prominent fault scarps in the Pedro de Valdivia Basin and the Central Depression (Baeza & Astudillo, 2019). These fault zones acted as conduits for the ascent of supersaturated saline fluids, leading to the precipitation of nitrate-rich crusts and filling of cavities and paleoconduits (Figure 5.6F-I). In addition, local reverse faults displace the horizontally stratified lacustrine sediments (Figure 5.7C), most likely resulting from mechanical adjustments to the pressure exerted by the overlying volcanic flows. This structural complexity favored repeated episodes of fluid migration, salt accumulation, and partial remobilization, contributing to the multi-phase evolution of nitrate mineralization in the area.

5.2.2 Oficina Domeyko (23,81°S / 69,35°W)

- Type of nitrate deposit: type-i, type-iib and type-iic.

- Nitrate description: Type-i deposit occurs as cementing material within ancient alluvial deposits on the slopes and foothills surrounding rhyolitic outcrops. They form black caliche up to 1 m thick, typically at the base of stratified gravel layers (Figure 5.8 B-D). These caliches exhibit dense, fine-grained textures and display local color variations related to oxidation and the presence of soluble salts. At the surface, yellow soluble salts (I and Cr rich; Table A3.1) are observed coating wet alluvial sediments (Figure 5.8 E-H), where evaporative concentration occurs after rainfall or groundwater discharge, representing the present-day nitrate deposition on the surface. Type-iic occurrences consist of massive and fibrous nitrate, predominantly white and yellow in color, forming extensive mantos and veins up to 1 meter thick that crosscut the rhyolitic host rock (Figure 5.9 D-H). These veins commonly exhibit crystalline, transparent to opaque textures, with occasional layering indicative of multi-stage mineral deposition. In several localities, stalactitic nitrate accumulations are observed hanging from fracture cavities, suggesting mineral precipitation from descending brines in open spaces.

- Other salts: The associated minerals include sulfates (cogenetic gypsum, anhydrite, and thenardite), chlorates, iodates, borates, lithium, and strontium-bearing nitrates (Table A3.1).

- Host rock and alteration: The host rock is volcano-sedimentary, primarily composed of rhyolitic lava flows showing pink to light-grey coloration, with phenocrystals of quartz, feldspar, and biotite in an aphanitic groundmass. Exsolution and alteration textures (Figure 5.9 I-J) are locally developed, reflecting post-magmatic processes. Rhyolitic tuff is also present, containing plagioclase, quartz, feldspar crystals, and lithics. The surrounding deposits comprise poorly sorted, polymictic braccias and sandstones, moderately consolidated and containing interbedded volcanic ash lenses, extending toward the lower slopes of the rhyolitic outcrops.

- Stratigraphic and chronologic correlation of the host rock: The rhyolitic units correspond to the Cinchado Formation (Upper Paleocene - Lower Eocene; Marinovic, 2007), with the sedimentary sequences assigned to the Depósitos de gravas antiguas (Lower Miocene-Upper Miocene) and Depósitos aluviales y coluviales antiguos (Upper

Miocene – Pliocene; Marinovic, 2007). This stratigraphic framework records the long-term interplay between Paleogene volcanism and Neogene sedimentation in the evolving forearc domain of northern Chile.

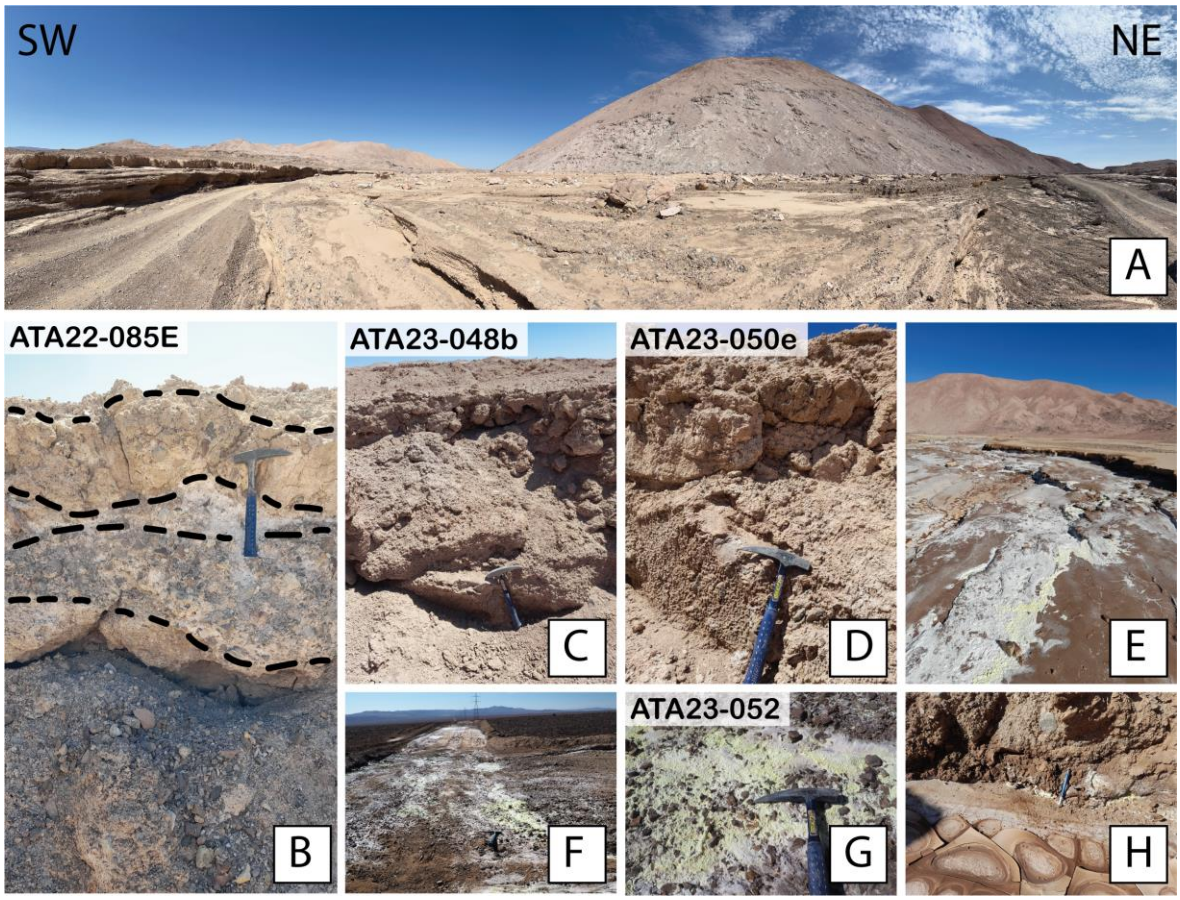

Figure 5.8: Type-I deposits from the Oficina Domeyko. A) Panoramic view of Oficina Domeyko. B), C) and D) Sedimentary sequences from alluvial deposits. E-H) Yellow soluble salts coating the wet surface on the active drainage.

- Depositional environment of the stratigraphic sequence: The rhyolitic rocks formed within a continental volcanic-arc setting during the Paleocene-Eocene, currently exposed in the eastern part of the Central Depression and the Precordillera (Marinovic, 2007). Subsequent tectonic fracturing generated a network of open cavities and fractures, which were later filled with nitrate-, chlorate-, and sulfate-rich salts transported by circulating fluids. These processes reflect the transition from volcanic to sedimentary environments and the influence of repeated aridification cycles on salt accumulation.

- Structural Geology of the area: The region is dominated by a N-S fault system in the northern sector, which facilitated the emplacement of dykes within the volcanic rocks,

and a NW–SE fault system in the south. These faults served as conduits for the circulation of saline fluids and for mineral precipitation. Some nitrate veins show ductile deformation features, implying precipitation during or shortly after tectonic movement, under conditions of elevated temperature and fluid pressure.

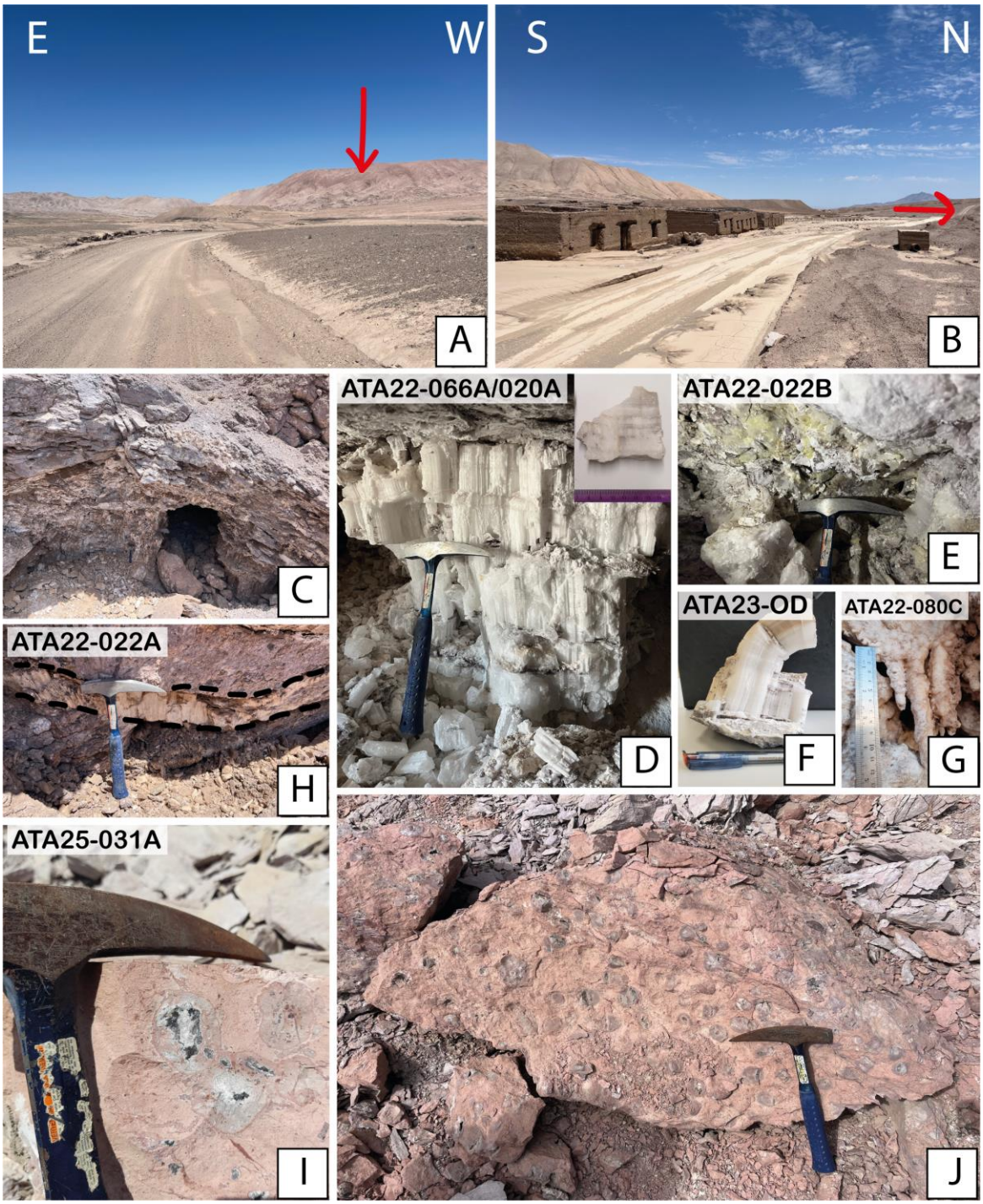

Figure 5.9: Type-iic deposits from the Oficina Domeyko. A) Landscape view from the cave is shown in C (red arrow). B) Landscape view from the mining ruins, showing the sample position of H. C) Mining cave. D) Manto of white caliche cutting through rhyolitic rocks. E) Yellow caliche veins at the roof of the cave. F) Fibrous white caliche sample taken from the cave, showing ductile deformation. G) Stalactite from the roof of the cave. I-J) Exsolutions in host rhyolitic rocks.

5.2.3 Aguas Blancas (24,16°S / 69,89°W)

- Type of nitrate deposit: Type-i, type-iia, type-iic

- Nitrate description: Type-i nitrates occur as cement in horizontal stratified sedimentary sequences composed of moderately to highly consolidated breccias and sandstones (Figure 5.10 A, F, and H). The highest nitrate concentration is found in the black caliche horizon, displaying commonly massive textures and brown to miner red coloration due to oxidation and variable salt content. Type-iia deposits are observed as nitrate mantos up to 50 cm thick, cutting the caliche layer (type-i) of the sedimentary succession (Figure 5.10 B-E, G). These veins show massive to fibrous habits and exhibit color variations from white to pale-yellow, reflecting compositional variability and iodine enrichment (Table A3.1). Type-iic deposits are observed as transparent nitrate crystal veins and druse cutting andesitic lava (Figure 5.10 I-J).

- Other salts: Associated salts include sulfates (gypsum and thenardite), chlorates, iodates, borates, chromates, bromides, strontium, lithium, and arsenic-bearing nitrates (Table A3.1).

- Host rock and alteration: The host rocks are volcanic-sedimentary, comprising black andesitic lava flows and overlying alluvial deposits. The andesitic lava displays a porphyritic texture, with phenocrystals of plagioclase and pyroxene, immersed in a black aphanitic matrix. Locally, the lava is brecciated and oxidized along fracture zones, providing pathways for nitrate-bearing fluids. The overlaying alluvial sequence consists of well-stratified, horizontally layered, brown-coloured breccia and sandstone, moderately to highly consolidated, with thicknesses of the whole sequence ranging from 1.20 to 5 m. The clasts are polymictic, poorly sorted, ranging in size from 1 to 15 cm, subangular to angular, immersed in a matrix of fine sand and silt. The clasts are mainly volcanic and intrusive rocks of the surrounding area (Lucero, 2023). Moderate oxidation and incipient cementation are observed toward the upper portions of the sequence, whereas the basal horizons show strong caliche development.

- Stratigraphic and chronologic correlation of the host rock: The andesitic lava belongs to the La Negra Formation (Middle Jurassic; Ferrando *et al*, 2013), whereas breccias and sandstones from the alluvial deposits are assigned to the Pampa de Mulas Formation (Upper Oligocene-Middle Miocene; Ferrando *et al*, 2013).

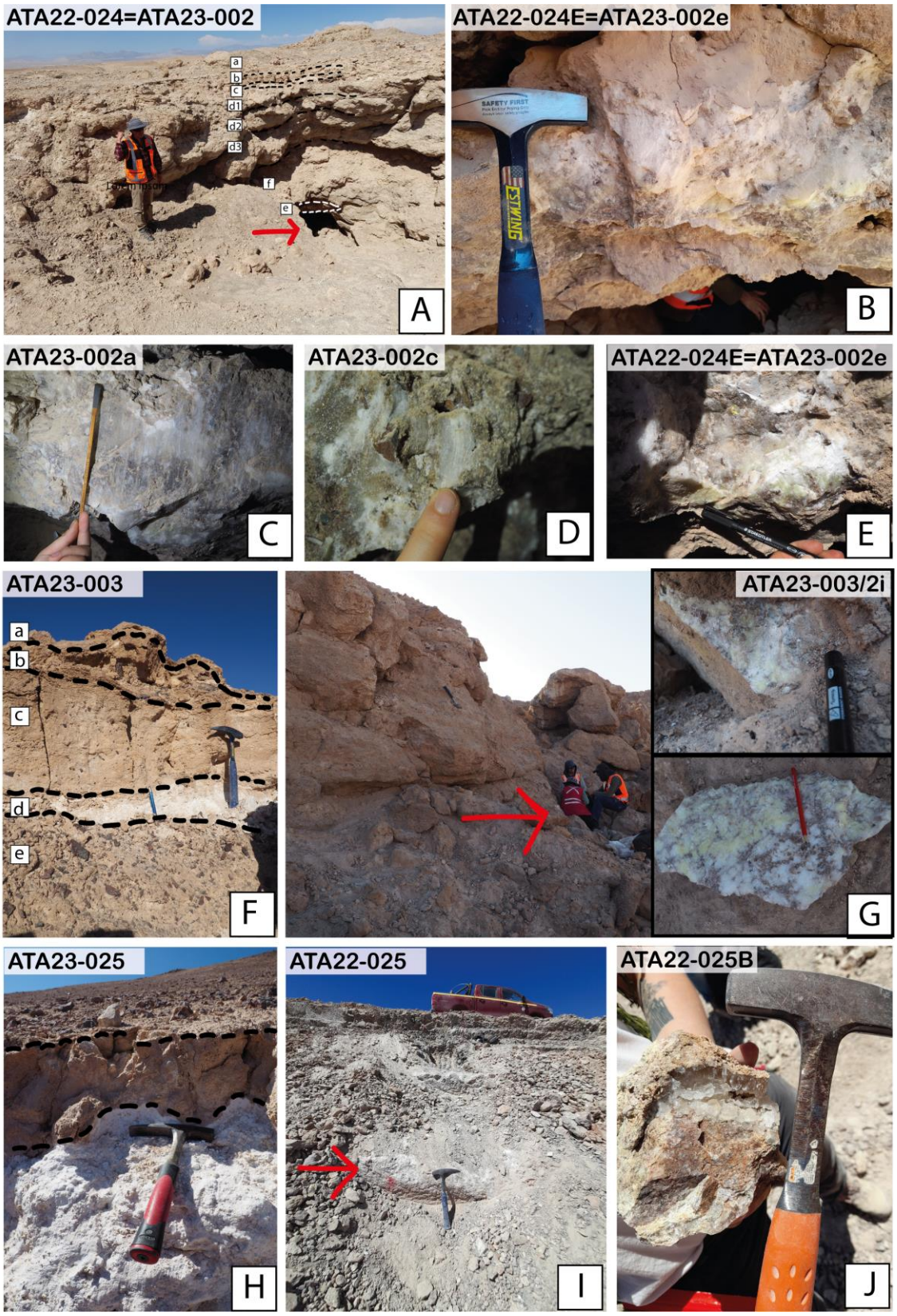

Figure 5.10: Types of nitrate deposits from the Aguas Blancas. A) Sedimentary deposit (type-i) showing the different layers of the sequence. The red arrow shows the entrance to the cave. B-E) Mantos of white caliche cutting the lower black caliche level from the sedimentary sequence in A (type-iia deposit). B and E show the same layer, C and D show manto layer inside the cave. F) Sedimentary sequence exposing surface crust (a), subsurface (b), chuca (c), thenardite (d), and costra layer(e). G) Sedimentary sequence cut by a manto of yellow and white caliche (red arrow). H) Sedimentary sequence showing surface crust, chuca, and thenardite layer. I-J) White crystalline caliche layer cutting an andesitic breccia.

- Depositional environment of the stratigraphic sequence: The La Negra volcanic rocks represent an ancient Jurassic volcanic arc, located within the present-day Coastal Cordillera, and generated through crustal contamination along the active continental margin. The breccias and sandstones represent a continental alluvial environment, where sediments were transported and reworked by high- to low-energy fluvial systems, reflecting the progressive uplift and erosion processes that affected the eastern Central Depression. The deposits document the response of the surface processes to the Andean tectonic uplift, recording alternating phases of sedimentation, incision, and chemical evaporation. They also represent paleodrainage systems that were active during the Miocene, later interrupted by aridification and tectonic faulting, which enhanced fluid migration and salt accumulation along fractures and permeable layers.

- Structural Geology of the area: The study area is strongly influenced by a NW-SE-oriented sinistral strike-slip system (Santiago fault), which controls the regional physiography and displaces the contact between the Middle and Upper Jurassic intrusive units and the volcanic rocks of the La Negra Formation by at least 4 km (Ferrando *et al*, 2013). This structure is interpreted as a major crustal discontinuity that accommodated both horizontal and vertical displacement during multiple tectonic phases. A second NW-SE oriented structure (Eugenia Fault) affects the alluvial deposits and intrusive rocks, while NNE-SW faults cut primarily the andesitic lava flows of the La Negra Formation (Lucero, 2023). These intersecting fault systems created a permeable structural network that facilitated the circulation of oxidized, saline fluids and the subsequent precipitation of nitrate and associated salts, particularly along fracture zones and contact planes.

6 Methodology

This chapter outlines the procedures used for the preparation and analysis of solid nitrate-bearing samples collected from different geological contexts and types of nitrate deposits (Table A1.1). The analytical methods employed include chemical and multi-isotopic composition ($\delta^{18}O$, $\Delta^{17}O$, $\delta^{15}N$, and $\delta^{34}S$), designed to characterize both, the primary and secondary processes influencing in nitrate formation and remobilization. In addition, the procedures data normalization, calibration, and evaluation of analytical reproducibility are described in detail to ensure the reliability and comparability on the results.

6.1 Sample Preparation and Leaching

All samples were first homogenized by grinding in a quartz mortar, followed by a sequential leaching procedure designed to separate highly soluble salts (e.g., nitrates, chlorides, Na-sulfates) from less soluble phases (e.g., Ca-sulfates, silicates, carbonates).

For the water-soluble salt analyses of major (Na, Cl, S, Ca, Mg, K and NO_3) and trace (As, Cr, I, Li, Sr, B, and Br) elements, approximately 100 mg of powdered sample was leached in 10 mL of deionized water (18.2 MΩ·cm), and shaken for 14 days at room temperature (~25°C) to achieve complete dissolutions of soluble salts. The leached was then separated from the residual solid by centrifugation (5 min at 3500 rpm). The supernatant was carefully pipetted off and retained for analysis. The remaining solid was rinsed three times with 1 mL of deionized water, with each rinse supernatant being combined with the initial leachate.

For less soluble salt phases, such as calcium sulfate (gypsum or anhydrite), Ca and S were analyzed by adding 10 mL of 0.01 M sodium carbonate solution in 100 mg of powdered sample, and shaken overnight at room temperature to promote the anion exchange reaction ($CaSO_4(s) + Na_2CO_3(aq) \rightarrow CaCO_3(s) + Na_2SO_4(aq)$) to extract the less-soluble sulfates for the analysis. The sulfate-rich supernatant was then separated via centrifugation and stored for analysis.

6.2 Chemical Composition Analysis

6.2.1 Nitrate Concentration via Spectrophotometry

Nitrate ($NO3^-$) concentrations in the water leachates were determined by spectrophotometry as nitrite (NO_2^-) using the vanadium (III) chloride reduction method and measured with Griess reagent (Miranda *et al.,* 2001). This method.

In a 96-well microplate, 180 µL of sample, standard, or blank was mixed with 150 µL of a freshly prepared colorimetric reagent. The reagent consisted of a 20:1:1 mixture of saturated vanadium (III) chloride (VCl_3), 2% (w/v) sulfanilamide (SULF) in 1.2 M HCl, and 0.1% (w/v) N-(1-Naphthyl) ethylenediamine dihydrochloride (NEDD). The plate was incubated for 60 minutes at 45°C, and the absorbance was measured at 540 nm using a Thermo Scientific Multiskan GO microplate reader.

A six-point calibration curve was generated daily using certified nitrate standard solutions, Certipur, Merck (0-100 µM). The method's accuracy was verified by analyzing a certified reference material (Anions-Whole Volume, Sigma-Aldrich) as an unknown sample, yielding a mean recovery of 113.5% (n = 90), within the certified range. Method precision was better than 8% RSD across the calibrated range. The measured values for the calibration range and reference material can be found in Table A2.1 from the appendix.

6.2.2 Major and Trace Element Analysis via ICP-OES

The concentration of major ions (Na, Cl, S, Ca, Mg, K, and NO3) and trace elements (As, Cr, I, Li, Sr, B, and Br) in water leachates and, and S in sodium carbonate leachates—for total sulfate — were determined by using inductively coupled plasma optical emission spectrometry (ICP-OES; SPECTRO ARCOS).

The leachates were diluted in 0.5 M ultrapure HNO_3 for all elements, to match the linear dynamic range of the instrument and to minimize matrix effects. Dilution factors were recorded for each sample for back-calculation.

A multi-element calibration was performed using certified single-element standard solutions (Merk). Five calibration points were used for each element, with a defined target concentration (Table A2.2). Instrumental drift was monitored and corrected for

by measuring a drift control solution (K03, K00, ATA-INT-1, and BATTLE-2 or BATTLE-19; Table A2.3) after every 6, 9, and 11 samples in the sequence. The validity of the calibration and sample analysis was confirmed by measuring a certified reference material (Table A2.2) as an unknown (Table A2.3). Reproducibility was typically better than ±0.18-13.29% SD for major elements and ±0.03-0.13% for trace elements, based on repeated measurements from different analytical sessions (Table A2.3).

6.3 Purification of Nitrate for Triple-Oxygen Isotope Analysis

The triple-oxygen isotope composition of nitrate was measured on purified silver nitrate ($AgNO_3$) precipitates. The purification procedure, modified from Silva *et al.* (2000) for low-nitrate concentrated samples and Klipsch *et al*. (2021) for high-nitrate concentrated samples, was designed to remove interfering anions, primarily chloride (Cl^-) and sulfate (SO_4^{-2}).

6.3.1 Low-NO_3 concentrated samples (1-6 %)

Water leachates of each sample with 200 µM of nitrate were prepared in 15 ml of deionized water (18.2 MΩ·cm; Silva *et al.*, 2000), shaken overnight, centrifuged, and pipette off.

Sulfate removal: The supernatant was treated with 0.5M Barium chloride dihydrate ($BaCl_2 \cdot 2H_2O$, VWR Chemicals) to precipitate sulfate as barite ($BaSO_4$). The amount of $BaCl_2 \cdot 2H_2O$ added slightly exceeded the molar concentration of SO_4^{-2} in the sample, ensuring complete precipitation. The solution was shaken overnight, centrifuged, and filtered with a 25mm Syringe Filter with a w/0.45µm polyethersulfone (VWR). The precipitated barite was stored for future sulfur isotope analysis (see Section 6.6)

Chlorine removal: The free-sulfate solution is loaded into an anion exchange column packed with AG 1-X8 Resin (100-200 mesh, Bio Rad) that has been pre-conditioned to the chloride (Cl^-) form, adding 1.5 ml of 5M HCl, and rinsing with 5 ml of deionized water to remove any Cl^- excess. As the sample passed through the resin, NO_3^- exchanges with Cl^-. The solution was rinsed with 15 ml 0.8 M HCl to collect the nitrate as HNO_3 eluent (Silva *et al.*, 2000).

Silver Nitrate generation: To generate $AgNO_3$ from the solution, 2g of Silver (I) Oxide (Ag_2O, Sigma Aldrich) is added, removing any residual Cl- as AgCl precipitate, following the reaction (Silva *et al.*, 2000): $HCl_{(aq)} + Ag_2O_{(s)} + HNO_{3(aq)} \rightarrow H_2O + AgNO_{3\,(aq)} + AgCl_{(s)}$, pH neutral. The solution was shaken overnight to promote AgCl precipitation, centrifuged, and the $AgNO_3$ solution was pipette off. The resulting $AgNO_3$ was dried in a vacuum centrifuge (Concentrator plus, Eppendorf) overnight (30°C), producing solid $AgNO_3$ ready to be used for isotope analysis.

6.3.2 High-NO_3 concentrated samples (6-100 %)

For high-NO_3 concentrated samples, 0.2M $NaNO_3$ of each sample was weighed into 5 ml of deionized water. In case of containing sediment, the aliquot was shaken overnight, centrifuged, and pipette off before concentrating 0.2M $NaNO_3$.

Sulfate removal: The collected supernatant was treated with around 0.1 ml of 5M $BaCl2{\cdot}2H_2O$ for most of the samples; nevertheless, the amount of $BaCl_2$ added was scaled to exceed the molar concentration of sulfate, ensuring complete precipitation (Gázquez & Claire, 2018). The solution was shaken overnight and centrifuged. The supernatant was pipetted of and filtered with a w/0.45µm polyethersulfone filter to remove the barite. The BaSO4 precipitate was stored for future sulfur isotope analysis (see Section 6.6), and the

Chlorine removal: The supernatant was loaded onto a cation exchange chromatography column packed with AG 50W-X8 resin (200-400 mesh, Bio-Rad) that had been pre-conditioned to the silver (Ag^+) form (modified from Klipsch *et al*., 2021). As the sample passed through the resin, Na^+ and other cations were exchanged for Ag^+, and chloride precipitated as insoluble AgCl within the column. The eluent, now a solution of pure $AgNO_3$, was collected.

Silver Nitrate generation: The $AgNO_3$ solution was dried in a vacuum centrifuge (Concentrator plus, Eppendorf) overnight at 30°C. The resulting pure $AgNO_3$ solid was stored in a desiccator until isotopic analysis to avoid water vapor being incorporated into the $AgNO_3$.

6.4 Triple-Oxygen Isotope Analysis

The triple oxygen isotope composition of nitrate ($\delta^{17}O_{NO3}$, $\delta^{18}O_{NO3}$, and $\Delta^{17}O_{NO3}$) was determined by pyrolysis of $AgNO_3$ in a high-temperature elemental analyzer coupled to a continuous flow isotope ratio mass spectrometer (CF-IRMS) at the University of Cologne, Germany. The method has been described by Schauer *et al*. (2012) and Klipsch *et al.* (2021), summarized in Figure 6.1.

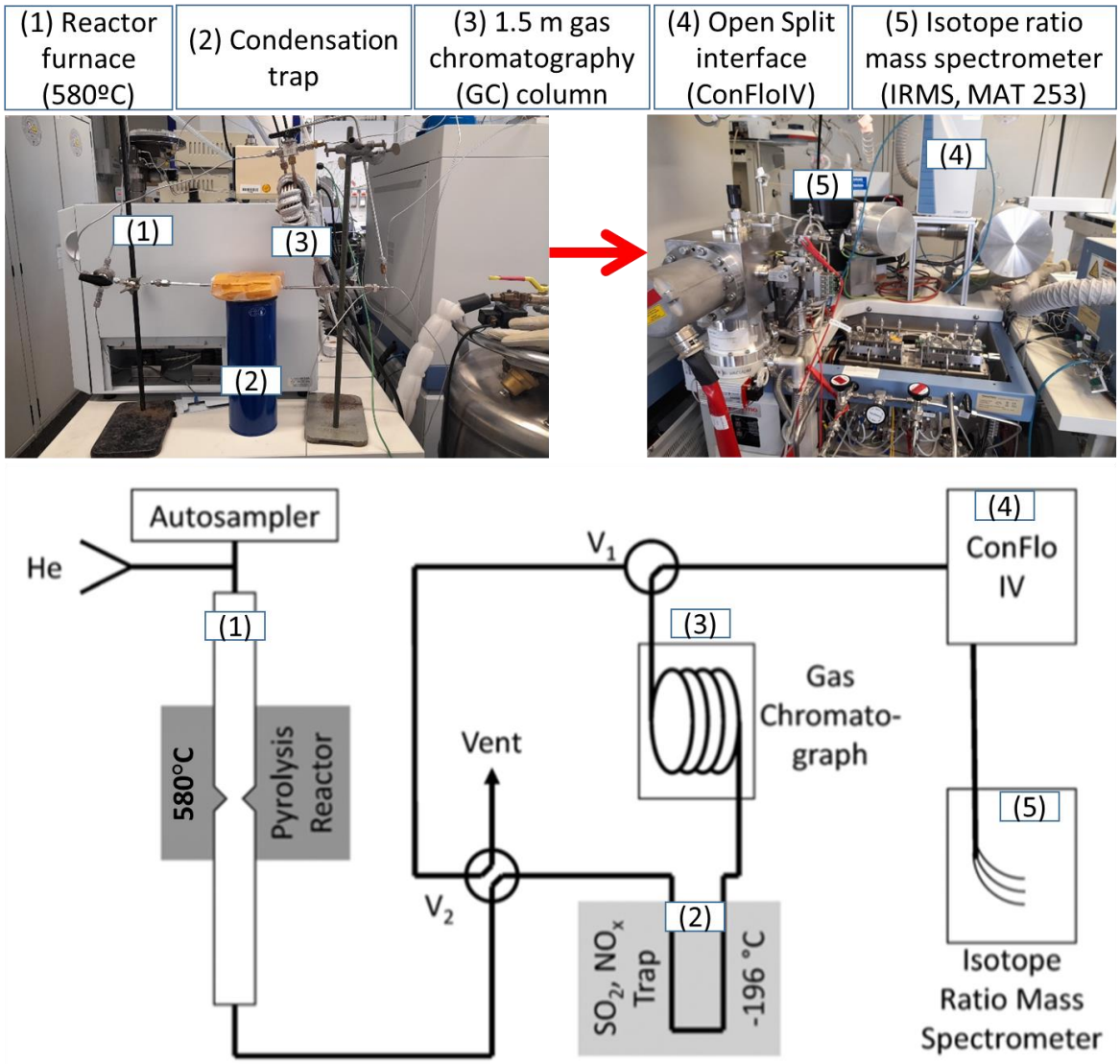

Figure 6.1: Summary steps of the $AgNO_3$ pyrolysis system for triple oxygen isotopes ($\delta^{18}O_{NO3}$ and $\Delta^{17}O_{NO3}$) measurements at the University of Cologne, Germany. Modified from Klipsch *et al.* (2021).

Procedure: Around 3 mg of $AgNO_3$ material was weighed into silver capsules (5 x 9 mm, HEKAtech GmbH, Germany) folded for each sample, and loaded in an autosampler (zero blank Vector SAS, EuroVector, Pavia, Italy), which were dropped into the pyrolysis reactor (quartz reactor tube) vertically positioned in an EA furnace (Euro EA 3000; EuroVector). The pyrolysis occurs at 580°C generating the thermal

decomposition of $AgNO_3$ ($AgNO_{3(s)} \rightarrow 1/2\ O_{2(g)} + NO_{2(g)} + Ag_{(s)} + N_{2(g)\,(trace)}$; Figure 6.1(1)). The gases produced by thermal decomposition (O2, NO2, N2, and NO) are transported by a continuous He flow at a rate of 120 mL min-1 through a cold trap filled with liquid nitrogen (-196°C) to remove NO_2 and NO (Figure 6.1(2)). Then the trace amounts of N_2 and CO, and other gases are separated from O_2 by passing through a GC (gas chromatography) column (1.5 m column packed with 5 Å molecular sieve) at room temperature (Figure 6.1(3)). Finally, the sample O_2 gas is introduced through an open split interface system (ConFlo IV, Thermo Fisher Scientific; Figure 6.1(4)) into an isotope ratio mass spectrometer (MAT 253; Thermo Fisher Scientific, Waltham, MA, USA; Figure 6.1(5)). The results of the isotope ratio O_2 of the sample are compared with a reference O_2 gas by measuring m/z 32, 33, and 34. The software's result shows two reference peaks and a third one that represents the sample peak.

Normalization and Reproducibility: To ensure traceability to international reference scales, oxygen isotope data ($\delta^{18}O_{NO3}$ and $\Delta^{17}O_{NO3}$) were normalized using internal laboratory reference materials previously calibrated against internationally recognized reference materials USGS34 and USGS35 (Böhlke *et al*., 2003, and Michalski *et al.*, 2002). Initially, two in-house nitrate standards (UoC-Nit-2 and UoC-Nit-3; see Appendix A2.1 for elaboration of standards) were calibrated against USGS34 ($\delta^{18}O$ = –27.9‰, $\Delta^{17}O$ = –0.1‰) and USGS35 ($\delta^{18}O$ = +57.5‰, $\Delta^{17}O$ = +21.6‰), following the normalization approach of Skrzypek (2012). A two-point linear regression was constructed for $\delta^{17}O$ and $\delta^{18}O$ separately (e.g., Figure 6.2), to calculate the slope and intercept between the measured (in-house standards) and accepted values (international reference materials). Measured standards values were then normalized by applying the regression line parameters for each analytical session.

The normalized $\Delta^{17}O$ values of UoC-Nit-2 ($\delta^{18}O$ = -9.6‰, $\Delta^{17}O$ = +19.2‰) and UoC-Nit-3 ($\delta^{18}O$ = -8.7‰, $\Delta^{17}O$ = +26.6‰) were then used to calibrate sample data, ensuring that all reported $\Delta^{17}O$ values are traceable to the VSMOW reference scale.

However, because UoC-Nit-2 and UoC-Nit-3 exhibited similar $\delta^{18}O$ values (~ -9‰), $\delta^{18}O$ normalization could not be accurately constrained during initial analyses. To address this, a second pair of in-house standards UoC-Nit-4 ($\delta^{18}O$ = +40‰, $\Delta^{17}O$ = 12.8‰) and UoC-Nit-5 ($\delta^{18}O$ = +70‰, $\Delta^{17}O$ = +21‰) were develop to extend the $\delta^{18}O$ range (see Appendix A2.1 for elaboration of standards). These standards were likewise normalized against USGS34 and USGS35 using the same regression approach (Figure

6.2) as described above for both $\delta^{18}O$ and $\Delta^{17}O$. This ensured consistent scale realization across both isotopic systems.

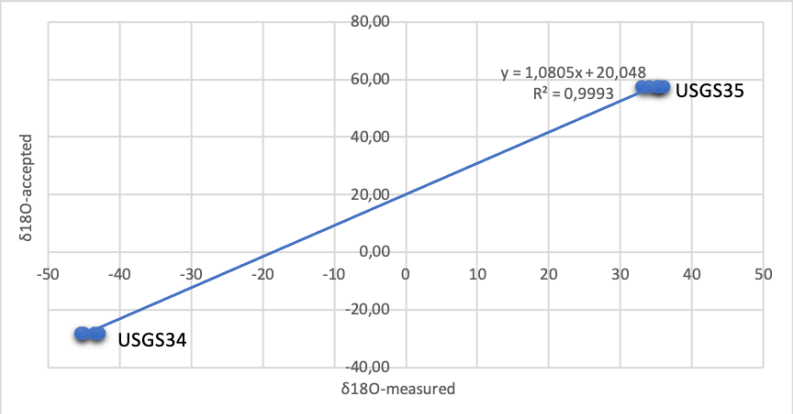

Figure 6.2: Example from a single session of a two-point normalization method utilizing linear regression ($y = ax + b$), with slope (a) and intercept (b) of 1.0805 and 20.048, respectively, for this case. Established based on two well-calibrated international standards for nitrate (USGS34 and USGS35), to recalculate the $\delta^{18}O$-measured/raw value of an internal standard (UoC-Nit-4 and UoC-Nit-5) to one of the international scale $\delta^{18}O$-accepted/VSMOW.

The external reproducibility (1σ) of the initial analysis, calibrated method with UoC-Nit-2 and UoC-Nit-3, is better than ±0.16‰ for $\Delta^{17}O$ after rejecting all data that differ more than 0.91‰ (3σ reproducibility), and was determined as the standard deviation of repeated measurements (n=481) of internal standards calibrated against external reference materials USGS-34 and USGS-35 (Böhlke *et al.*, 2003, and Michalski *et al.,* 2002). For the analysis calibrated with UoC-Nit-4 and UoC-Nit-5, the external reproducibility (1σ) is better than ±0.6‰ for $\delta^{18}O$ and ±0.1‰ for $\Delta^{17}O$ after rejecting all data that differ more than 3.1‰ for $\delta^{18}O$, and 0.4‰ for $\Delta^{17}O$ (3σ reproducibility), and was also determined as the standard deviation of repeated measurements (n=161) of internal standards calibrated against external reference materials. All isotope ratios are reported in per mil (‰) relative to VSMOW, and $\Delta^{17}O$ was calculated using equation 3.4, with $\lambda = 0.52$ (see Section 3.1.3).

To assess the consistency between the two normalization schemes (UoC-Nit-2/3 and UoC-Nit-4/5), $\Delta^{17}O$ values for replicate samples measured under both calibrations were statistically compared. Bland–Altman (B&A) analysis is used for assessing the method comparability, evaluating a bias between the mean differences (Bland and Altman, 1986; Giavarina, 2015). For the $\Delta^{17}O$ analysis under the two normalizations, the B&A analysis shows a mean difference of 0.095‰, with a paired t-test indicating no significant offset (p = 0.081) between methods (Figure 6.3A). Linear regression

yielded a slope of 0.956, an intercept of 0.710‰, and R^2 = 0.977 ($p < 0.001$), demonstrating near-unity proportionality and strong agreement (Figure 6.3B). These results confirm that both normalization schemes are analytically consistent within the uncertainty of $\Delta^{17}O$ measurements (typically ± 0.1–0.16‰), and data from the two methods can be confidently combined for interpretation.

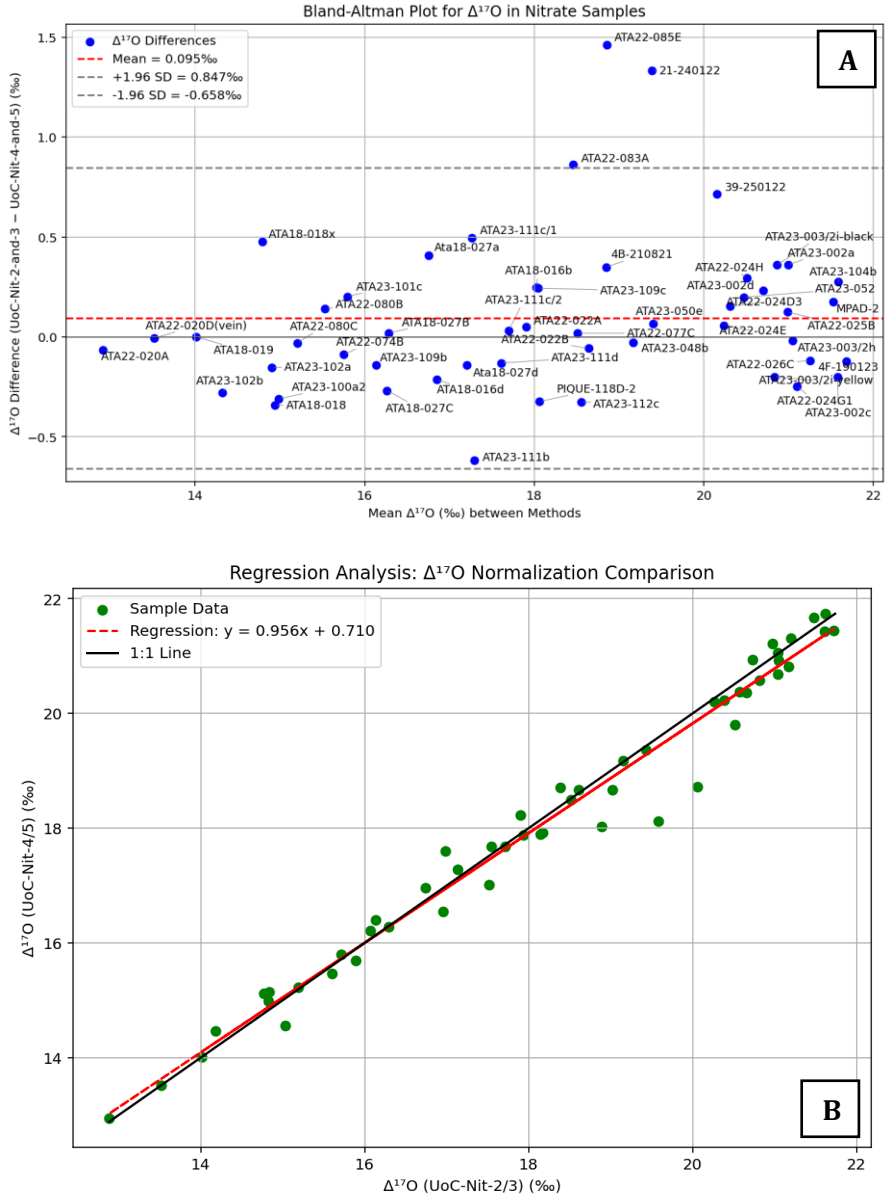

Figure 6.3: A) Bland-Altman plot comparing $\Delta^{17}O$ in nitrates normalized with UoC-Nit-2/3 versus UoC-Nit-4/5. The mean difference was 0.095‰ and with a p-value of 0.081(paired t-test), indicating no significant systematic bias. B) Regression plot comparing $\Delta^{17}O$ from the same normalization strategies in A). The regression line (y = ax + b) closely follows the 1:1 line, with R^2 = 0.977 and p-value <0.001, confirming strong agreement and linearity, with a relation between the two methods highly significant statistically.

The absence of a statistically significant bias between normalization schemes indicates that differences in the isotopic range of internal standards (UoC-Nit-2/3 vs. UoC-Nit-4/5) did not affect the scale realization for $\Delta^{17}O$. Therefore, all normalized data are considered directly comparable on the VSMOW reference scale. Finally, the $\Delta^{17}O$ normalized value was calculated with the average between the two methods for each sample.

For samples with multiple replicates, the mean and standard deviation (1σ) based on repeated analyses of each sample are reported. When only a single valid measurement was available (n = 1), the analytical uncertainty was estimated using the external reproducibility of the method, representing external analytical precision under identical instrumental conditions (Coplen, 2011; Paul *et al*., 2007). For combined $\Delta^{17}O$ datasets obtained from both normalization schemes (UoC-Nit-2/3 and UoC-Nit-4/5), the overall analytical precision was calculated using the pooled standard deviation, following McDonald (2014).

6.5 Nitrogen Isotope Analysis

For $\delta^{15}N$ analyses, approximately 50 mg of N—estimated from NO_3^- concentrations—from the homogenized sample powder was weighed into tin (Sn) capsules and combusted in a Thermo Scientific Flash EA Isolink Elemental Analyzer, interfaced via a Thermo Conflo IV split interface to a Thermo Finnigan MAT 253 isotope ratio mass spectrometer (IRMS) at the Leibniz Institute for Baltic Sea Research (IOW, Warnemünde, Germany). The evolved gases were carried in a continuous flow of high-purity helium (grade 5.0), with dinitrogen (N_2) used as both sample and reference gas (Pollmann *et al.,* 2021).

The nitrogen isotope ratios were expressed in conventional δ-notation relative to atmospheric N_2 (AIR). Calibration to the international AIR scale was achieved using the certified intercomparison materials IAEA-N-1 and IAEA-N-2. Analytical precision, determined from replicate analyses of standards and representative samples, was better than ± 0.15 ‰ for $\delta^{15}N$. The reported δ-values are given in per mil (‰), equivalent to milli-Urey (mUr; Brand and Coplen, 2012 *in* Pollmann *et al.,* 2021).

6.6 Sulfur Isotope Analysis

Sulfur isotope analyses were performed on sulfate species associated directly with the nitrate ores and thenardites from soil profiles of nitrate deposits. For $\delta^{34}S$ determinations, the precipitated barite ($BaSO_4$) obtained in the purification step of nitrate for triple oxygen isotopes (Section 6.3.1 and 6.3.2) was used. For thenardite samples, soluble sulfate was extracted and precipitated as barite by adding 2 ml of 0.5M $BaCl_2$ to ensure complete precipitation (Klipsch *et al.,* 2023). The barite precipitates were purified to remove residual by dissolving the $BaSO_4$ precipitate in DTPA–KOH solution and reprecipitating by adding HCl, following the procedure of Klipsch *et al.* (2023), then dried at 37°C overnight.

The purified and dried $BaSO_4$ samples were weighed into tin (Sn) capsules and combusted in a Thermo Scientific Flash EA Isolink Elemental Analyzer coupled via a Thermo Finnigan Conflo IV interface to a Thermo Finnigan MAT 253 IRMS at the Leibniz Institute for Baltic Sea Research (IOW, Warnemünde, Germany). The resulting sulfur dioxide (SO_2) was used as both sample and reference gas in a continuous stream of high-purity helium (5.0) (Pollmann *et al.,* 2021).

Sulfur isotope ratios were expressed in δ-notation relative to the Vienna Canyon Diablo Troilite (VCDT) scale. Calibration to the international scale was performed using the certified standards IAEA-S-2, IAEA-S-3, and NBS 127. The external reproducibility of $\delta^{34}S$ analyses was better than ± 0.1 ‰ (Klipsch *et al.,* 2023).

6.7 Raman Spectra Analysis

Raman spectra were obtained with a Renishaw InVia Qontor spectrometer by a frequency-doubled 532 nm Nd:YAG laser with 100 mW output energy in 180°C backscatter geometry with an 1800 lines/mm grating, a slit opening of 65 µm, a Rayleigh edge filter with a cut-off below approx. 50 cm^{-1} and a front-illuminated CCD Centrus detector. The estimated spectral resolution is about 0.4 cm^{-1}. Spectra were recorded with a transmission filter of 5% over 60 times 1 s for each the low and high wavenumber region of interest. The unknown oxide was measured with a transmission filter of 0.05 for 1000 times 1 s. Before measurements, the spectrometer was calibrated with a Si standard. All spectra were background-corrected with splines.

7 Results

This chapter presents the results of the geological and geochemical characterization of nitrate deposits from the Atacama Desert. The primary objective is to constrain the sources and formation processes of these deposits through their isotopic signatures and geological context. The results are organized by analytical approach, beginning with the oxygen isotopic composition of nitrate ($\delta^{17}O$, $\delta^{18}O$, and $\Delta^{17}O$), followed by nitrogen isotopes ($\delta^{15}N$) and sulfur isotopes ($\delta^{34}S$). Together, these results provide the basis for the interpretations and broader implications discussed in Chapter 8.

7.1 Triple Oxygen Isotopes

The triple oxygen isotopes ($\delta^{17}O$, $\delta^{18}O$, and $\Delta^{17}O$) of nitrate deposits from the Atacama Desert provide key insights into their sources and formation processes (see Section 3.2). Because oxygen in nitrate can originate from both atmospheric and secondary processes, the analysis of triple oxygen isotopes is particularly useful for distinguishing between primary atmospheric deposition and post-depositional alteration. This section presents the $\delta^{17}O$, $\delta^{18}O$, and $\Delta^{17}O$ data obtained from representative samples across different nitrate deposit types and localities. The results are compared with previously reported oxygen isotope values from atmospheric and water samples and interpreted in relation to the geological context of each deposit.

All samples analyzed from different types of nitrate deposits display a positive oxygen mass-independent fractionation, with $\Delta^{17}O$ values ranging from 13 to 22‰ (Figure 7.1A; Table A3.2). These values are consistent with those in previous studies of Atacama nitrates deposits (Böhlke *et al.,* 1997; Michalski *et al*., 2004; Melchiorre *et al.,* 2018; Figure 3.2), confirming a primary atmospheric deposition. However, those earlier studies did not describe the geological context of the various deposit types or referred to them collectively as sedimentary deposits (type-i). In this study, the geological setting of distinct deposit types is examined, revealing differences in their oxygen isotopic composition.

The ^{17}O-anomalies show no clear correlation with geographic location (Figure 7.1A) or elevation (Figure 7.2A) but vary systematically among the different deposit types.

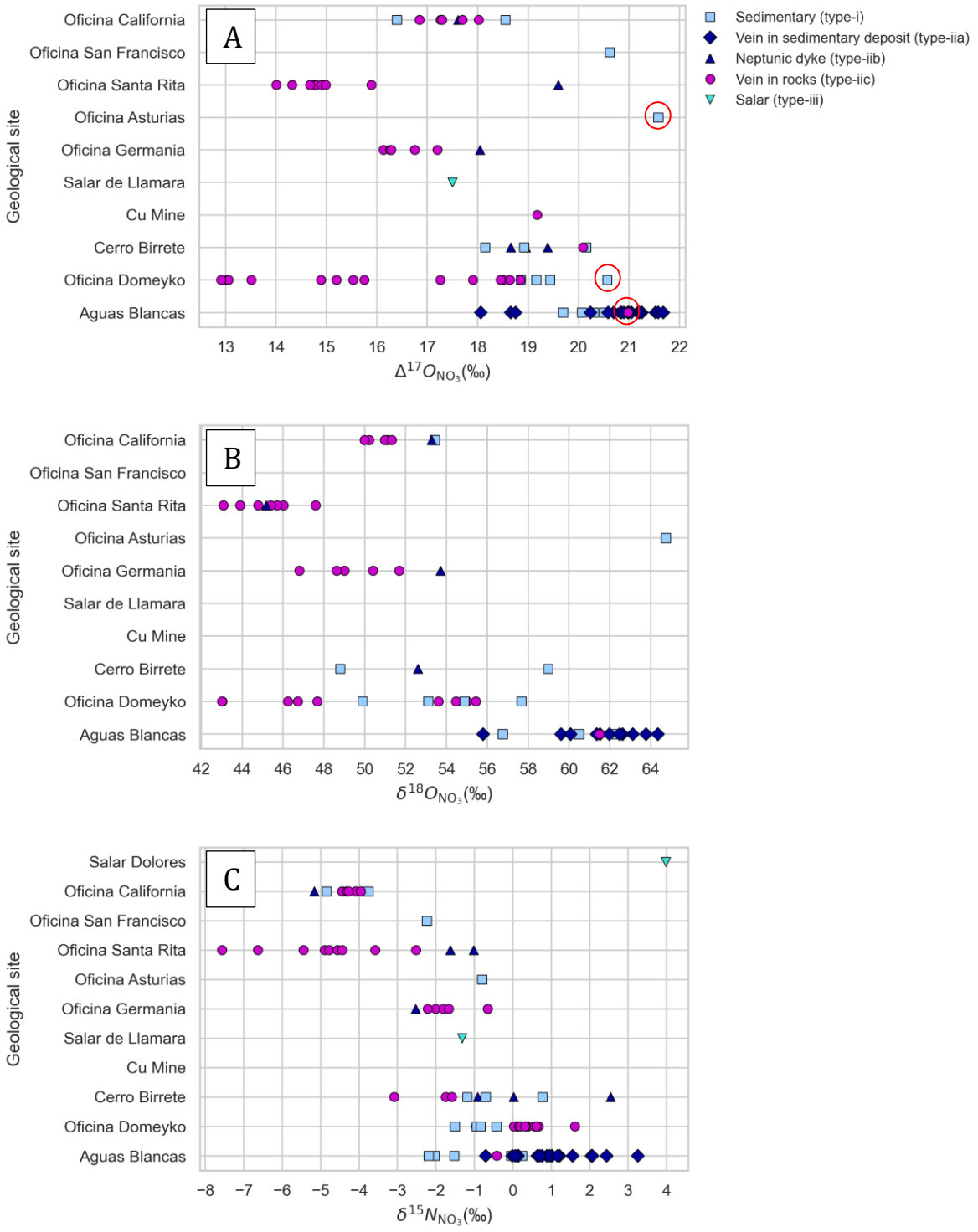

Figure 7.1: $\Delta^{17}O$ (A), $\delta^{18}O$ (B), and $\delta^{15}N$ (C) values in nitrate plotted against geological sites. Deposit types are distinguished by colors and symbols (see legend in panel A). Geological sites are arranged from north to south (top to bottom).

Type-iia deposits exhibit the highest anomalies, with $\Delta^{17}O$ values between 18 and 22 ‰, and occur exclusively within the Aguas Blancas District (Figure 7.1A). Type-i deposits show $\Delta^{17}O$ values between 16 and 22‰, with the lowest values (16 to 19‰) corresponding to samples from Oficina California, Cerro Birrete, and Oficina Domeyko,

and the highest values (20 to 22‰) recorded at Aguas Blancas, San Francisco, Oficina Asturias, Cerro Birrete, and Oficina Domeyko (Figure 7.1A). The single sample from Oficina Domeyko that falls within the upper range ($\Delta^{17}O$= 20.57‰) corresponds to the sample ATA23-052 (Figure 5.8 E-H), a yellow surface salt precipitated after recent rainfall (marked with a red circle in Figure 7.1A). Another sample, the ATA23-104b from Oficina Asturias, is a powdery salt collected from surface cracks within an alluvial deposit and shows the second-highest anomaly among all measured samples ($\Delta^{17}O$ = 21.58‰; red circle in Figure 7.1A). Although these two samples differ from the typical hard, black caliche of sedimentary deposits, they are classified as type-i deposits because their chemical composition—nearly pure nitrate (Table A3.1)—and are interpreted as products of modern atmospheric nitrate deposition.

For the type-iii deposits, only one sample was analyzed, showing a $\Delta^{17}O$ value of 18‰ (Figure 7.1A). These types of samples are more difficult to purify (see Section 6.3.1), due to their high NaCl content, which requires a more rigorous process to obtain pure $AgNO_3$. This aimed to include additional data for the salar-type samples; however, the combination of purification challenges and instrument failures during mass spectrometry prevented the desired number of analyses from being completed. Nevertheless, the available data are useful for identifying isotope fractionation associated with biological recycling processes.

Type-iic deposits exhibit the lowest measured $\Delta^{17}O$ value (13 to 21‰) compared with the other types (Figure 7.1A-7.2A-7.3). The highest $\Delta^{17}O$ signature within this group corresponds to the sample ATA23-025B from Aguas Blancas, marked with a red circle in Figure 7.1A). This sample represents the only type-iic occurrence identified in the Aguas Blancas District and is unique among the studied nitrate veins because it cuts a volcanic breccia rather than a caliche layer from an alluvial fan deposit. Its $\Delta^{17}O$ value of 20.99‰ further supports its distinction within this deposit category.

Figure 7.3A shows $\Delta^{17}O$ versus $\delta^{18}O$ for nitrate samples analyzed in this study, covering different deposit types: sedimentary deposit (type-i, light blue squares), veins in sedimentary deposits (type-iia, dark blue diamonds), neptunic dykes (type-iib, dark blue triangles), and veins in rocks (type-iic, magenta circles). Atmospheric nitrate is included for comparison (small light blue crosses; Patris *et al.*, 2007; Morin *et al.*, 2009; and Savarino *et al.*, 2013).

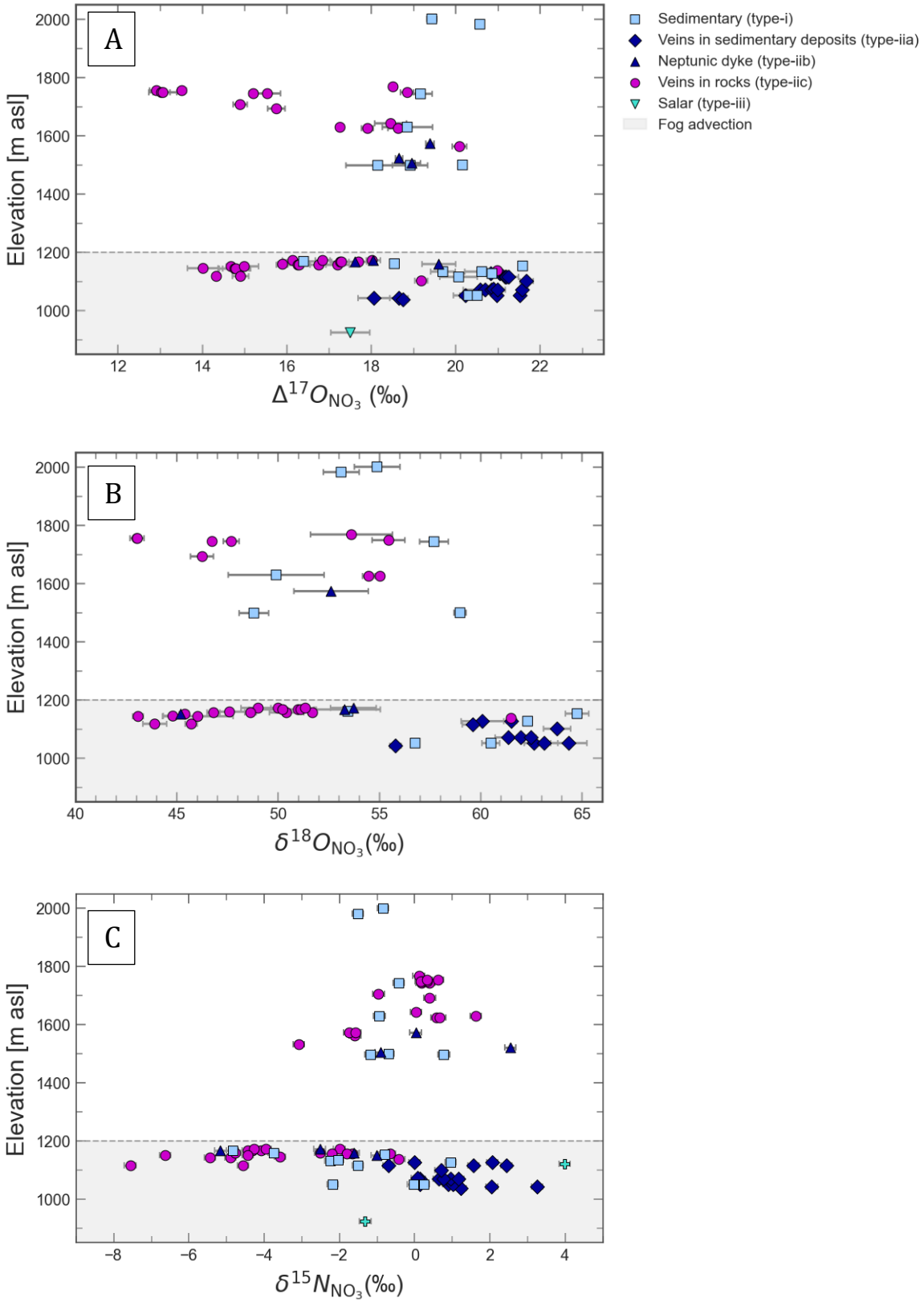

Figure 7.2: $\Delta^{17}O$ (A), $\delta^{18}O$ (B), and $\delta^{15}N$ (C) values versus elevation [m a.s.l.] for nitrate deposits. Colors and symbols represent different deposit types (see legend in panel A). Error bars indicate 1σ standard deviation of $\Delta^{17}O$ and $\delta^{18}O$ for each sample (see Table A3.2), and the external reproducibility of $\delta^{15}N$ measurements, which is 0.15‰. The gray shaded area marks the altitude range of advective fog, with its maximum altitude at 1200 [m a.s.l.] (Cereceda *et al.,* 2002; 2008).

The spread in $\Delta^{17}O$ values (Figure 7.3A) highlights isotopic variability among deposit types, suggesting subtle differences in formation or preservation conditions

Oxygen isotope composition of water from the Atacama Desert is also shown, including rainwater (light blue), groundwater (dark blue), and fossil hydrothermal water (magenta), with both individual measurements (small hexagons) and averages (large hexagons). Rainwater data are from Fritz *et al*. (1981); Aravena *et al*. (1999); Uribe *et al*. (2015); Jordan *et al*. (2018); Surma *et al*. (2018); groundwater from Magaritz *et al*. (1989); Fritz *et al*. (1981); Cortecci *et al*. (2005); Cervetto (2012); CMDIC (2012); Lopez *et al*. (2014); Uribe *et al*. (2015); Jayne *et al*. (2016); Scheihing *et al*. (2017); Surma *et al*. (2018); and fossil hydrothermal water from Leybourne & Cameron (2006). For unanalyzed water samples, $\Delta^{17}O$ is assumed to be 0‰, consistent with previous studies reporting near-zero $\Delta^{17}O$ in Atacama waters (Surma *et al*., 2018; Voigt *et al*., 2021). Average $\delta^{18}O$ values are -13.34‰, -10.44‰, and 2.89‰ for rainwater, groundwater, and fossil hydrothermal water, respectively. Dotted lines represent linear regressions: the blue line for atmospheric and sedimentary nitrates, the black line for all nitrate deposits measured in this study, and the magenta line for the veins in rocks, with corresponding equations shown in the figure legend.

The inclusion of isotopic data from various hydrological reservoirs provides a broader geochemical framework to interpret the relationship between nitrates and water-rock interaction processes across different depositional environments. These water signatures serve as key isotopic baselines for understanding mixing mechanisms and potential hydrothermal overprinting in the nitrate system.

A positive correlation between $\delta^{18}O$ and $\Delta^{17}O$ is observed in the analyzed samples (black dotted line). Type-iic deposits exhibit relatively low $\delta^{18}O$and $\Delta^{17}O$ values, whereas type-i and type-iia deposits display high $\delta^{18}O$ and $\Delta^{17}O$ values, close to the atmospheric nitrate signature. Type-iib shows intermediate values for both isotopes. This progressive isotopic shift among deposit types likely reflects differences in depositional or post-depositional environments, such as variable degrees of fluid interaction or microbial mediation. The decreasing isotopic signature observed in type-iic deposits suggests a mechanism related to their specific geological context that modifies the oxygen isotope composition.

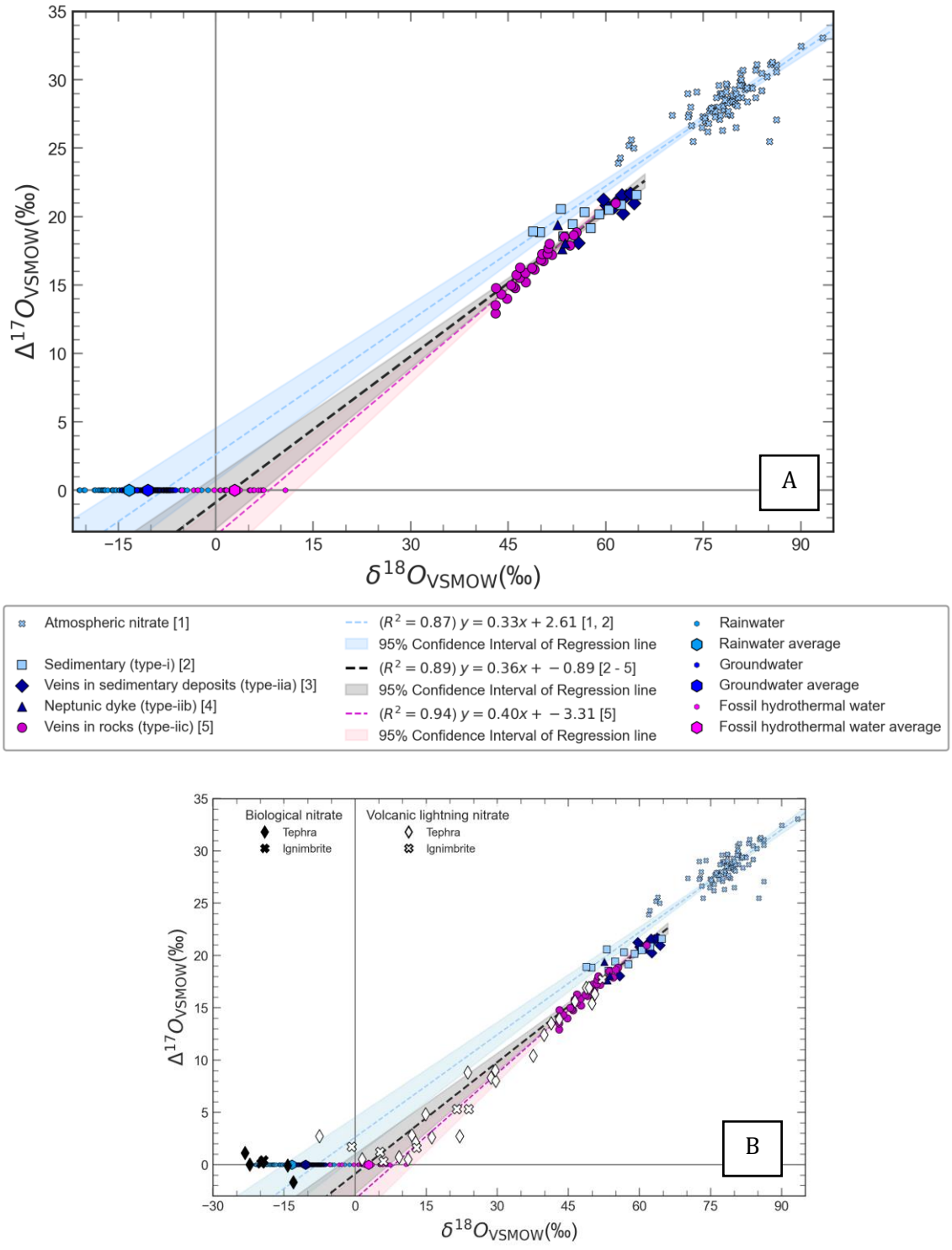

Figure 7.3: A) $\Delta^{17}O$ versus $\delta^{18}O$ for nitrates analyzed in this study: sedimentary deposits (type-i, n=16), veins in sedimentary deposits (type-iia, n=18), neptunic dykes (type-iib, n=6), and veins in rocks (type-iic, n=35). Also shown are atmospheric nitrate (n=90), and local waters—rainwater (n=61), groundwater (n=293), and fossil hydrothermal water (n=33). Dotted lines indicate linear regressions: blue for atmospheric and type-i deposit, black for all nitrate deposits measured in this study, and magenta for the type-iic deposit. B) Same as A but including volcanic lightning and biological nitrate from volcanic deposits. Data sources: Atmospheric nitrate from Patris *et al.* (2007), Morin *et al.* (2009) and Savarino *et al.* (2013); rainwater from Fritz *et al.* (1981); Aravena *et al.* (1999); Uribe *et al.* (2015);

Jordan *et al*. (2018); Surma *et al*. (2018); groundwater from Magaritz *et al*. (1989); Fritz *et al*. (1981); Cortecci *et al*. (2005); Cervetto (2012); CMDIC (2012); Lopez *et al*. (2014); Uribe *et al*. (2015); Jayne *et al*. (2016); Scheihing *et al*. (2017); Surma *et al*. (2018); fossil hydrothermal water from Leybourne & Cameron (2006); and volcanic lightning and biological nitrate from Aroskay *et al* (2024). Volcanic lightning nitrates can be generated by NOx oxidation via ozone, or via an atmospheric oxidant with $\Delta^{17}O=0$.

Using the regression equation for all nitrate samples (black dotted), $\delta^{18}O$ can be extrapolated to $\Delta^{17}O$ is 0‰. For Atacama nitrates, this value is $\delta^{18}O$ = 2.47‰, which closely matches the average $\delta^{18}O$ of fossil hydrothermal ($\delta^{18}O$ = 2.89‰; Figure 7.3A). This supports the influence of water-nitrate exchange in shaping the isotopic composition. The blue regression line (Figure 7.3A) represents the correlation between atmospheric nitrate and sedimentary deposits (type-i). When is extrapolated to $\Delta^{17}O$ is 0‰, it matches close to the groundwater average (big blue diamond), reinforcing the water-nitrate exchange. The magenta line (Figure 7.3A) represents the regression line only for type-iic deposits and would fit in a much-enriched fossil hydrothermal water, a possible endmember of hydrothermal water from the past. This water-nitrate exchange reflects a dynamic interplay between atmospheric deposition, subsurface water circulation, and post-depositional hydrothermal overprinting that shaped their present isotopic characteristics.

Figure 7.3B shows the same data as Figure 7.3A but adding volcanic lightning and biological nitrate from Aroskay *et al.* (2024). They study nitrates in volcanic deposits (tephra and ignimbrite) from the Neogene caldera-forming eruptions. According to their data, the triple-oxygen isotope composition of the nitrates reveals that they are the final product of atmospheric nitrogen fixation driven by volcanic lightning (positive $\Delta^{17}O$; Figure 7.3B). This finding supports the hypothesis that volcanic lightning can serve as a transient but significant source of atmospheric nitrate formation during periods of intense volcanic activity. The alignment of volcanic lightning-derived nitrates with the regression line of Atacama samples (Figure 7.3B) further strengthens the interpretation that episodic volcanic events may have contributed to the overall nitrate budget in the desert through atmospheric deposition. In contrast, the field of biologically derived nitrates (black symbols in Figure 7.3B) plots distinctly away from the Atacama trend, confirming that biological activity had only a minor or localized influence on the formation of these deposits.

7.2 Nitrogen Isotopes

The nitrogen isotopes ($\delta^{15}N$) of nitrate provide insights into nitrogen sources, post-depositional modification and microbial processes such as nitrification, denitrification, and ammonia volatilization. In the Atacama Desert, microbial activity appears to exert only a minor influence on $\delta^{15}N$ values; instead, $\delta^{15}N$ primarily reflects post-depositional alteration of an original atmospheric nitrogen source (Böhlke *et al*., 1997; Melchiorre *et al*., 2017; and Reich and Bao, 2018).

The nitrogen isotopic composition ($\delta^{15}N$) of the analyzed nitrate samples ranges from approximately -8 to 4‰ (Figure 7.4), which is slightly lower than $\delta^{15}N$ measured in previous studies of the Atacama nitrate (-5 to +5‰; Böhlke *et al*., 1997, Melchiorre *et al*., 2017), and it displays a systematic variation among deposit types and geological contexts (Figure 7.1C-7.2C). When plotted against geological context, $\delta^{15}N$ values tend to show an enrichment of -3 to +4 ‰ in samples from the Central Depression of the Antofagasta Region (Cerro Birrete, Oficina Domeyko and Aguas Blancas District), and depletion to -8 to -3 ‰ in samples form Tarapacá Region, especially those in the Coastal Cordillera and near Salar Dolores (Oficina California and Santa Rita), with an exception at Salar Dolores, which exhibits the highest value among all measured samples. Samples from the Central Depression in the Tarapacá Region (Oficina San Francisco, Asturias, Germania, and Salar de Llamara) show intermediate values of -3 to 0‰ (Figure 7.1C; Figure 2.1). This correlation is also evident when $\delta^{15}N$ is plotted against elevation [m a.s.l.]. $\delta^{15}N$ values of -8 to -3 ‰, in samples from the Tarapacá Coastal Cordillera, occur exclusively within the advective-fog belt (Figure 7.2C), which may reflect secondary alteration processes rather than the primary nitrogen source.

The most pronounced differences observed are between type-iic and type-iia deposits. Type-iic deposits show $\delta^{15}N$ values approximately between -8 and +1‰, and type-iia range from around -1 to +4‰. Type-i, type-iib, and type-iii deposits show values in between, from -5 to +1‰; -5 to+2‰; and -1 to +4‰, respectively. However, for the type-iii there are only two samples measured, the lowest from Salar de Llamara ($\delta^{15}N \approx$ -1‰), and the highest from Salar Dolores ($\delta^{15}N \approx +4$‰; Figure 7.1C).

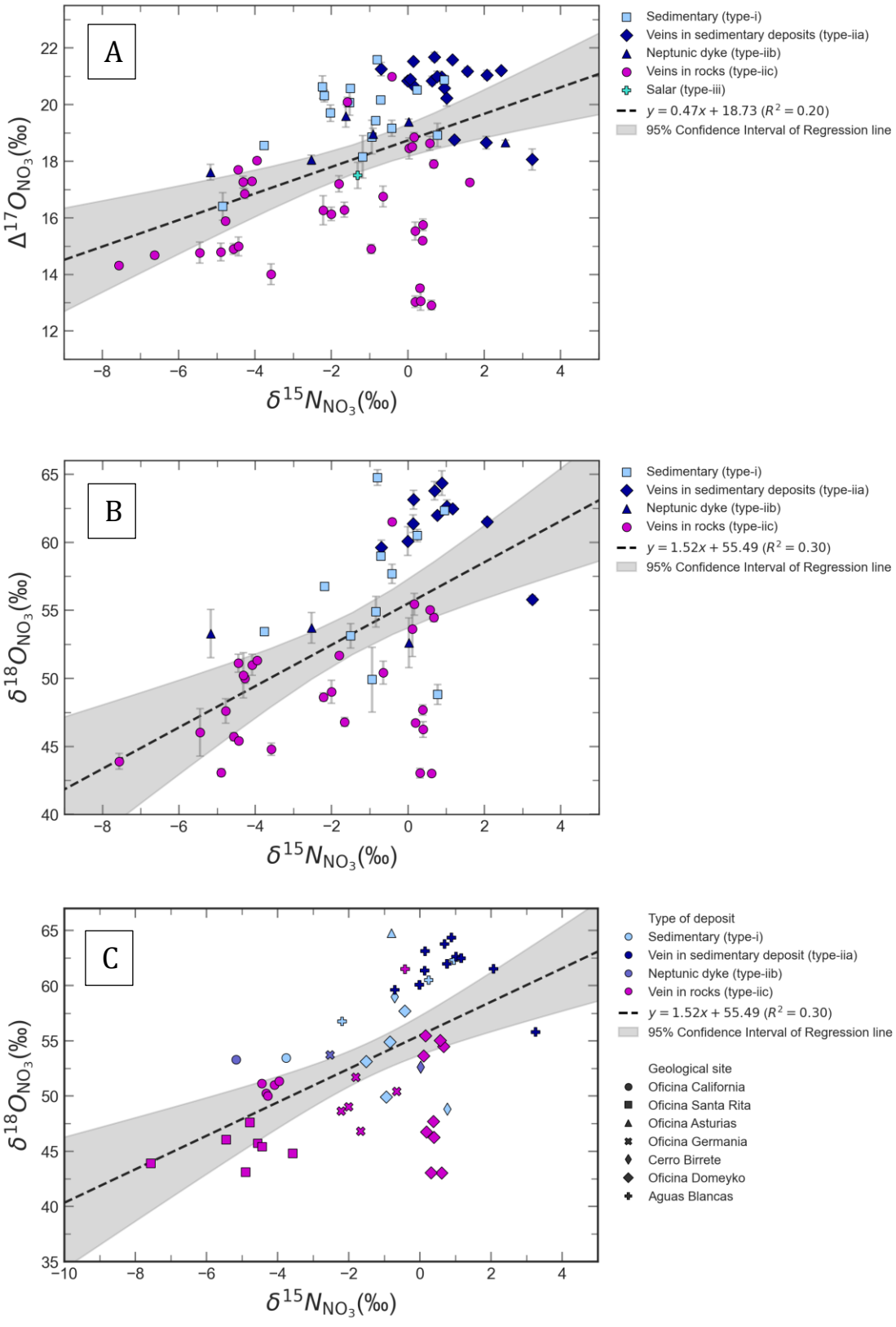

Figure 7.4: A) $\Delta^{17}O$ versus $\delta^{15}N$; B) $\delta^{18}O$ versus $\delta^{15}N$ in nitrate samples. Different colors and symbols represent the distinct deposit types (same as figure 7.1- 7.3). The black dotted line shows the linear regression for all data, with its 95% confidence interval shaded in gray. The regression equation is provided in the legend. C) Same as panel B, but with symbols distinguishing individual geological sites.

Figure 7.4 examines the relationships between $\Delta^{17}O$ and $\delta^{15}N$ and between $\delta^{18}O$ and $\delta^{15}N$. In general, the regressions for all analyzed samples (black dotted line; 95% CI shaded) indicate a weak positive correlation (R^2=0.2 and 0.3 for $\Delta^{17}O$ vs $\delta^{15}N$, and $\delta^{18}O$ vs $\delta^{15}N$, respectively). This pattern is consistent with the results of Böhlke *et al.* (1997), who also reported positive correlations in Atacama nitrate, but contrasts with Melchiorre *et al*. (2018), who found a negative correlation in their samples. However, the latter analyzed horizontally stratified sedimentary sequences not directly comparable with our dataset, which does not include isotope analysis from vertical sedimentary profiles. Even so, their caliche layer samples from the Antofagasta Region, with $\delta^{15}N$ values from -1 to +1‰, are comparable to the type-i deposits analyzed here.

Samples with higher $\Delta^{17}O$ (closer to atmospheric values) systematically exhibit higher $\delta^{15}N$, whereas samples with reduced $\Delta^{17}O$ show lower $\delta^{15}N$; the same relationship holds between $\delta^{18}O$ and $\delta^{15}N$. This pattern implies that the processes that preserve the atmospheric $\Delta^{17}O$ signature—limited water exchange—are associated with relatively enriched $\delta^{15}N$ values. Conversely, samples that have undergone greater post-depositional alteration (lower $\Delta^{17}O$ and $\delta^{18}O$; Figure 7.3) display lighter nitrogen isotopic compositions, consistent with isotope exchange and/or fractionating processes operating during remobilization. Samples from Oficina Santa Rita clearly show the general $\delta^{15}N$-$\delta^{18}O$ trend; however, not all samples follow this pattern. Samples from Oficina Domeyko are the exception, exposing little $\delta^{15}N$ variation despite large variability of $\delta^{18}O$ (Figure 7.4C), suggesting local nitrogen recycling reactions controlled by geological context. Hence, spatially variable $\delta^{15}N$–$\delta^{18}O$–$\Delta^{17}O$ relationships across the study area highlight the importance of local geological and hydrogeological controls in shaping the isotopic evolution of nitrate deposits in the Atacama Desert.

Figure 7.5 compares Atacama nitrate $\delta^{15}N$-$\delta^{18}O$ data with atmospheric, volcanic-lightning, and biological nitrate compositions (Patris *et al.,* 2007; Morin *et al*., 2009; Savarino *et al*., 2013; and Aroskay *et al.,* 2024). Atmospheric nitrate shows low $\delta^{15}N$ and high $\delta^{18}O$ values, biological nitrate the opposite, and volcanic-lightning nitrates fall between both. In contrast, Atacama nitrates lack the negative $\delta^{15}N$-$\delta^{18}O$ mixing trend typical of mixing between atmospheric-biological interactions (e.g., Jackson *et al*., 2015) and differ from the marine-influenced signatures of coastal soils in the Antofagasta Region (Ewing *et al.,* 2007).

Instead, the positive $\delta^{15}N$-$\delta^{18}O$ correlation observed indicates minimal biological cycling and isotopic compositions dominated by non-biological oxidation pathways. Figure 7.5B is essential for this comparison, as it directly contrasts our data with Ewing *et al.* (2007) and Jackson *et al.* (2015), clearly demonstrating the absence of a microbial mixing trend and supporting the interpretation of restricted biological influence during nitrate formation in the Atacama Desert.

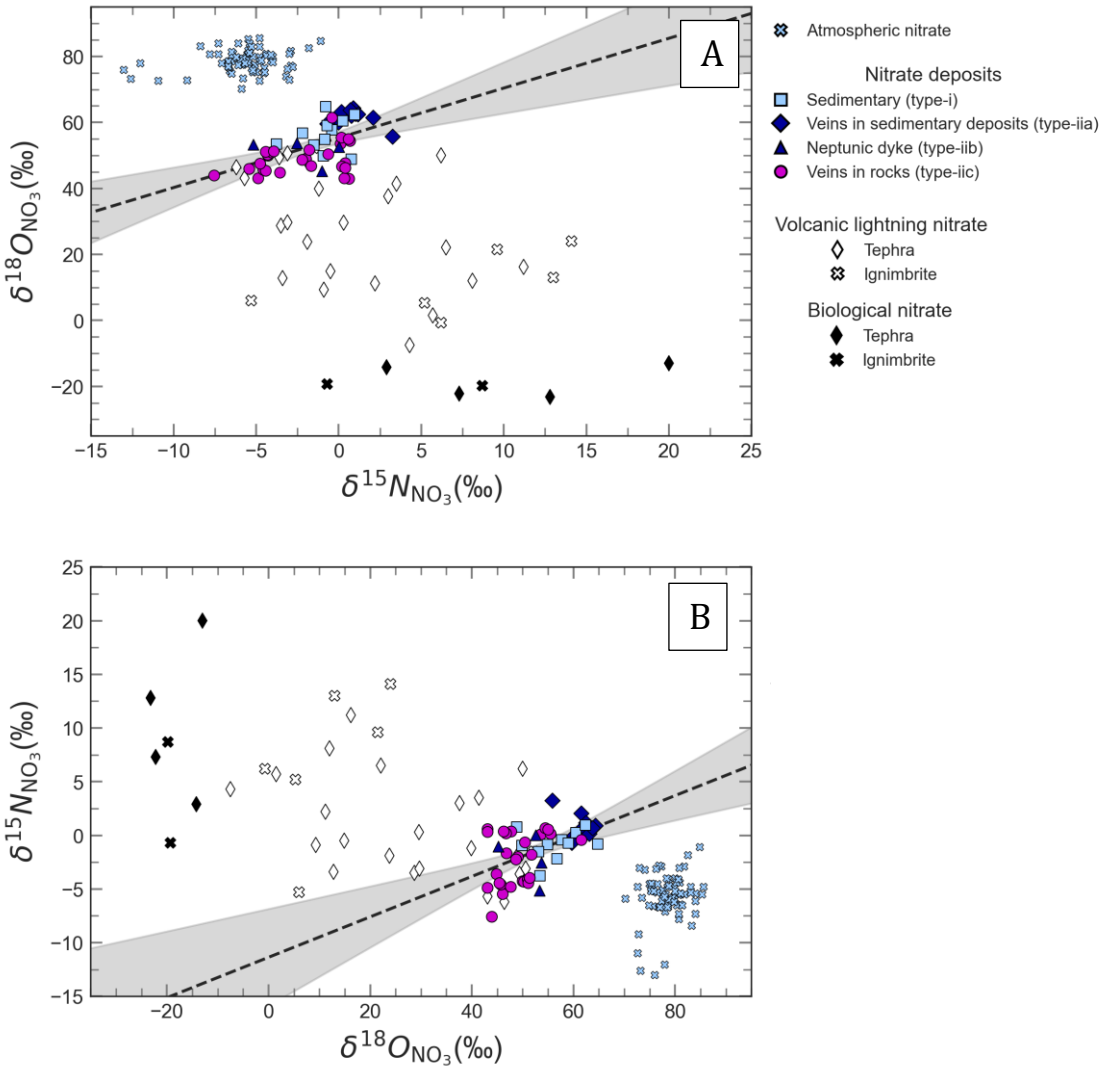

Figure 7.5: A) $\delta^{18}O$ versus $\delta^{15}N$, and B) $\delta^{15}N$ versus $\delta^{18}O$ in nitrate deposits (this study), atmospheric (Patris *et al.*, 2007; Morin *et al.*, 2009; and Savarino *et al.*, 2013), volcanic lighting and biological nitrate Aroskay *et al.*, 2024). The black dotted line shows the linear regression for nitrate deposits, with its 95% confidence interval shaded in gray. The regression equation is provided in the legend of Figure 7.4.

7.3 Sulfur Isotopes

The sulfur isotope composition ($\delta^{34}S$) of sulfates associated with nitrate deposits exhibits values between -2.1 and +9.8‰ (Figure 7.6-7.7). The $\delta^{34}S$ values show no systematic correlation with elevation (Figure 7.6) or latitude/Geological site (Figure 7.7). However, a subtle but interpretable pattern is observed within the thernardite (Na_2SO_4) samples. Thenardite is characteristic of type-i deposits, which occur in the upper part of the sedimentary sequence (Figure 2.2). These samples cover the full $\delta^{34}S$ range observed in the analyzed sulfates (-2.1 to +9.8‰; Figure 7.7), with the highest values occurring in the north (Oficina California) and the lowest in the south (Aguas Blancas). While the number of northern samples is insufficient to define a robust spatial trend, field observations indicate that thenardite becomes progressively less abundant northward into the Tarapacá Region, suggesting a geological control on its formation and preservation.

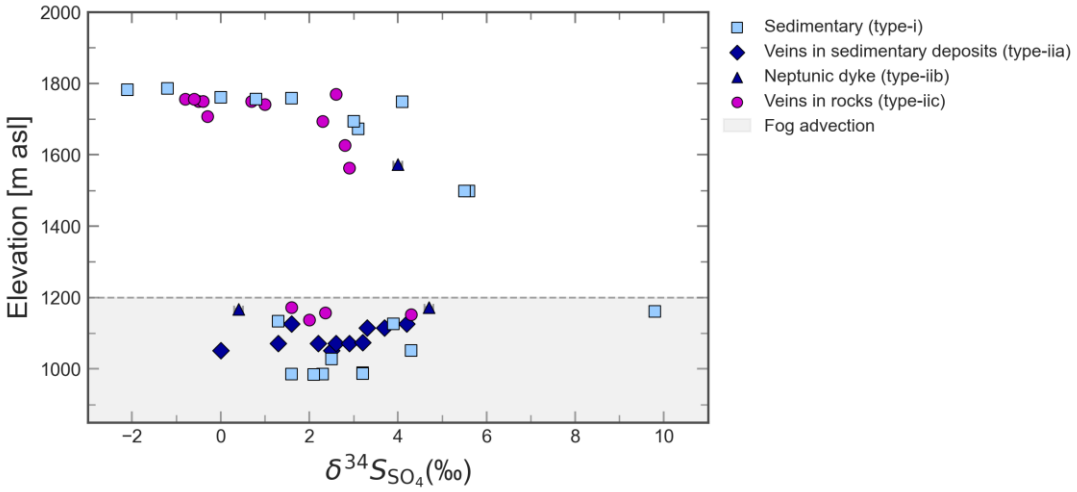

Figure 7.6: $\delta^{34}S$ values versus elevation [m a.s.l.] for sulfates associated with nitrate deposits. Error bars represent 1σ external reproducibility of $\delta^{34}S$ measurements (0.10‰) and are generally smaller than the symbols. The gray shaded area marks the elevation belt influenced by advective fog (up to ~1200 m a.s.l.; Cereceda *et al.,* 2002; 2008).

The $\delta^{34}S$ values of the thenardites from Aguas Blancas and Oficina Domeyko overlap with those reported by Klipsch *et al.* (2023). They proposed that thenardite composition between -0.9 and +5.2‰ reflects mixing toward a hydrothermal endmember represented by El Tatio hot spring ($\delta^{34}S \approx -5$‰). The similarity between the range measured in this study (-2 to +4‰; Figure 7.7) and the values reported by Klipsch *et al.* (2023) suggests that thenardites in nitrate deposits may follow the same

geochemical pathway, trending toward this hydrothermal signature. In particular, the relatively low $\delta^{34}S$ values at Aguas Blancas (down to -2‰) provide additional support for this idea, as they fall even closer to the inferred hydrothermal endmember. Such depleted sulfur isotope values are consistent with the incorporation of hydrothermal fluids that interact with the surface environment, either by redissolving atmospheric sulfates already present in the soils or by introducing hydrothermally leached sulfur transported upward through fault-controlled fluid pathways. These fluids could subsequently infiltrate through the sedimentary profiles, where evaporation and saline concentration favor the precipitation of thenardite layers (Klipsch *et al.,* 2023).

Veins (type-iic deposits) from Oficina Domeyko—containing both nitrate and sulfates (Table A3.1)—show $\delta^{34}S$ values between −0.30‰ and −0.80‰, closely matching the $\delta^{34}S$ of the local rhyolitic host rock (−0.60‰; Figure 7.7). This correlation further reinforces the influence of hydrothermal processes, as the isotopic similarity indicates that sulfur may be directly sourced from the host lithology. Under hydrothermal conditions, water–rock reactions efficiently mobilize sulfur-bearing minerals and leach sulfate or sulfide ions into circulating saline fluids, enhancing their contribution to near-surface geochemical systems (Leybourne & Cameron, 2006). Together, these observations suggest that hydrothermal inputs—either from deep-seated fluids or from rock-derived sulfur—play a significant role in controlling the sulfur isotope composition of sulfates associated with nitrate deposits in the Atacama Desert.

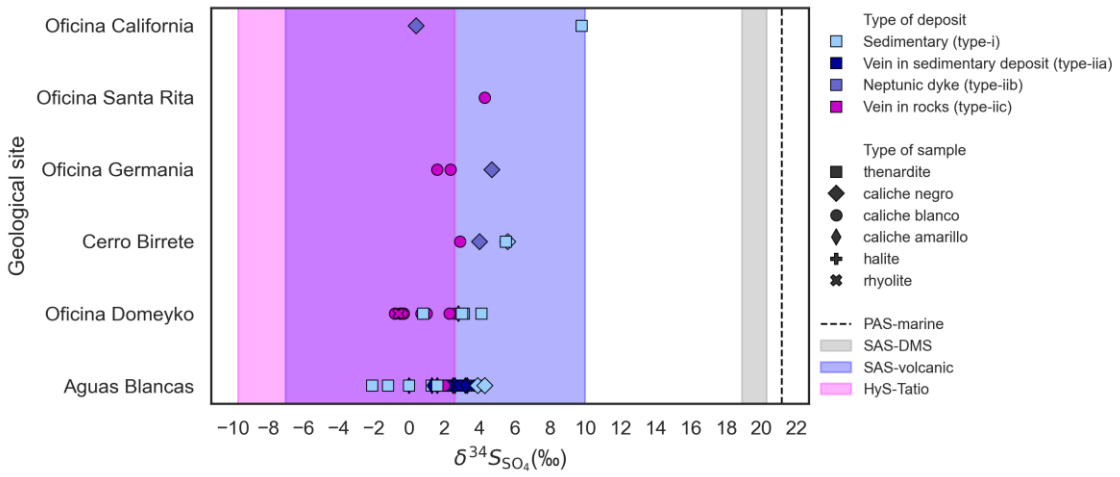

Figure 7.7: $\delta^{34}S$ values versus geological site. Different $\delta^{34}S$ values of sulfate sources are indicated: The vertical black dotted line represents the primary atmospheric sulfate (PAS-marine = +21.15‰; Johnston *et al*., 2014), the gray shaded area represents the secondary atmospheric sulfate from marine sources (SAS-DMS = +18.9 to 20.30‰; Klipsch *et al*., 2023), the blue shaded area is the secondary atmospheric sulfate from volcanic sources (SAS-volcanic = -7 to +10‰; Klipsch *et al*., 2023), and the hydrothermal sulfate from El Tatio hot spring (HyS = -9.7 to +2.6‰; Cortecci *et al.,* 2005; Klipsch *et al*., 2023).

7.4 Raman Spectra

Raman analysis was applied to an exsolution from the rhyolitic host rock of the type-iic deposits at Oficina Domeyko. The exsolution exhibits a distinctive zonation, consisting of a white core surrounded by black material, which in turn is enclosed by a thin white halo. Raman measurements were performed on both the core and the black zone. The core contains nitratine ($NaNO_3$) together with epsomite ($MgSO_4 \cdot 7H_2O$), whereas the black material is dominated by an unidentified oxide phase and erdite ($NaFeS_2 \cdot 2H_2O$; Figure 7.6). Oxides are difficult to characterize, as even low laser power can trigger a phase transition (Christoph Lenting, *pers. comm*.).

Exsolution textures generally record the trapping of fluids or gases trapped during late-magmatic crystallization or during subsequent hydrothermal alteration (Edmonds and Wallace, 2017; Miami and Geshi, 2025). In this case, the observed amygdaloidal texture—the white halo surrounding the black and white infill— within the exsolution texture corresponds to alteration minerals filling the vesiculation voids in volcanic host rocks, a texture commonly associated with hydrothermal pore-filling processes rather than magmatic vapor exsolution (Miami and Geshi, 2025).

These observations—the mineral assemblage of nitratine, epsomite, and erdite; and the correspondence of amygdaloidal texture with hydrothermal alteration— provide convergent evidence that the texture feature formed through post-depositional hydrothermal alteration rather than late-magmatic crystallization. This interpretation supports the broader conclusion that hydrothermal fluids have participated in the recycling and mobilization of nitrate deposits at Oficina Domeyko.

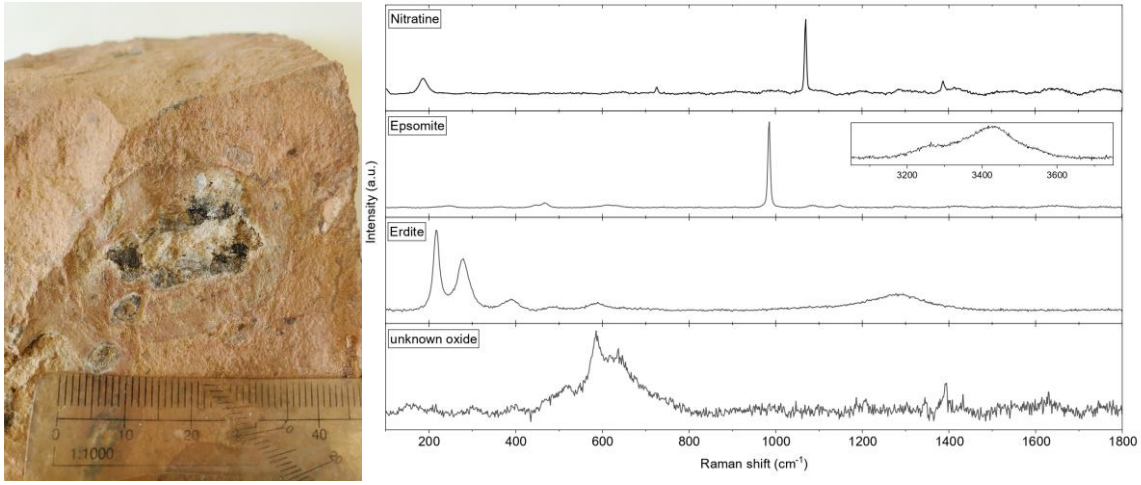

Figure 7.6: Raman spectra analyses in exsolution from rhyolites of Oficina Domeyko (ATA25-031A).

8 Discussion

This chapter integrates the geological and isotopic results presented in Chapter 5 and 7 to interpret the formation mechanism of Atacama Desert Nitrate Deposits. The isotopic compositions of oxygen ($\Delta^{17}O$, $\delta^{18}O$), nitrogen ($\delta^{15}N$), and sulfur ($\delta^{34}S$) provide robust constraints on the sources and post-depositional processes that shaped these deposits. The discussion is organized into three main sections: (1) the atmospheric contribution, which dominates the nitrate input; (2) potential volcanic sources that may have contributed to reactive nitrogen and sulfur species; and (3) post-depositional recycling processes involving biological activity, meteoric waters, and hydrothermal systems. Together, these insights allow a comprehensive reconstruction of the geochemical pathways responsible for the exceptional preservation of nitrates in the hyperarid Atacama environment.

8.1 Atmospheric Source

Nitrate can be naturally produced via atmospheric chemistry (oxidation of NO_x by O_3 and other oxidants) or microbial processes (ammonia oxidation and nitrification). These processes do not necessarily chemically change the nitrate in a system, but they reveal distinct isotope composition ($\Delta^{17}O$, $\delta^{18}O$, and $\delta^{15}N$) that reflect their formation pathways (Böhlke *et al*., 1997; Michalski *et al*., 2003, 2004; Morin *et al.,* 2007; Kaneko & Poulson, 2013; Savarino *et al.,* 2013; Reich and Bao, 2018).

The oxygen isotope composition of most terrestrial materials typically follows mass-dependent fractionation (MDF; $\Delta^{17}O$ = 0‰; equation 3.3), such that $\delta^{17}O$ and $\delta^{18}O$ covary along the terrestrial fractionation line (TFL) with a slope of ~0.52 (Figure 3.1). In contrast, the pioneering experiments of Thiemens & Heidenreich (1983) demonstrate that ozone formation can produce mass-independent fractionation (MIF; $\Delta^{17}O \neq 0$‰; equation 3.4), generating triple oxygen isotope signatures with slopes near 1—similar to those observed in meteorites—rather than to the TFL. This discovery established the basis for using ^{17}O-anomalies ($\Delta^{17}O$) to trace MIF in natural systems.

A significant consequence of this photochemically induced MIF is that atmospheric ozone acquires a large positive ^{17}O-anomaly, and any oxygen transferred from O_3 into

secondary products inherits part of this fingerprint $\Delta^{17}O$ enrichment. In the NO_x-NO_3 system, photochemical oxidation pathways involving ozone and its radicals in both the stratosphere and troposphere, produce NO_3 with positive $\Delta^{17}O$, with upper limits approaching the $\Delta^{17}O$ of bulk or transferrable ozone (on the order of +26 to +39‰; Thiemens & Heidenreich, 1983; Vicars and Savarino, 2014).

Nitrate produced by microbial processes (e.g., ammonia oxidation and nitrification), necessarily involves interaction with water to sustain microbial activity. Because the oxygen reservoir in water is much larger than that in nitrate, the oxygen isotope composition of microbially produced nitrate equilibrates with the MDF-controlled isotopic signature of the local water (Casciotti, 2009; Kaneko & Poulson, 2013). Consequently, biologically produced nitrate follows MDF and plots near the TFL ($\Delta^{17}O \approx 0$‰).

Thus, the sign and magnitude of $\Delta^{17}O$ in nitrate provide a direct test of whether its oxygen budget is dominated by atmospheric photochemistry or by biological processes.

Previous studies of oxygen isotopic composition in the Atacama nitrate deposits have demonstrated that nitrate preserves a large positive MIF signal ($\Delta^{17}O_{NO3}$ typically ~+14 to +21‰), consistent with an origin by long-term atmospheric deposition under hyperarid conditions (Böhlke *et al*., 1997; Michalski *et al*., 2004; Melchiorre *et al.,* 2018). Our new dataset falls within, and slightly extends this range, showing $\Delta^{17}O_{NO3}$ values that span from +13‰ to +22‰ (Figure 7.3A). Such elevated $\Delta^{17}O$ values clearly record a mass-independent oxygen anomaly of nitrate produced by photochemical reactions involving ozone (Equations 3.5-5.9; Thiemens & Heidenreich, 1983; Böhlke *et al*., 1997; Michalski *et al*., 2003, 2004; Morin *et al.,* 2007; Savarino *et al.,* 2013). Therefore, the observed anomalies confirm the primary atmospheric origin of oxygen incorporated into the Atacama nitrate.

The $\delta^{18}O$ signatures also provide information on the oxygen sources of nitrate, which can come mainly from ozone (Michalski *et al*., 2003, 2014). The tropospheric ozone carries bulk and transferable $\delta^{18}O$ values of ~115‰ and ~130‰ respectively (Vicars and Savarino, 2014), therefore, if nitrate is produced via ozone oxidation in the atmosphere will carry the large isotope signature of its precursor, as have been shown in the Atacama Desert with reported positive $\delta^{18}O_{NO3}$ values up to 61‰ (Böhlke *et al*., 1997; Michalski *et al*., 2004; Melchiorre *et al.,* 2018). Our data show $\delta^{18}O_{NO3}$ values that

range between 43 and 65‰ (Figure 7.3A), overlapping and slightly extending the previously reported Atacama range. When evaluated together, $\Delta^{17}O_{NO3}$ and $\delta^{18}O_{NO3}$ show a positive correlation and large oxygen signatures—such as those produce by ozone oxidation in the atmosphere—which further support the atmospheric origin of the nitrates.

However, the oxygen isotope composition of nitrate can be systematically modified by biological and hydrological activity. As we saw above, the oxygen exchange between intermediate N-species (NO_x) and water will overprint the isotope signature during microbial activity, equilibrating with the local water. Under these conditions, post-depositional nitrate produced or recycled through microbial pathways is expected to exhibit $\Delta^{17}O \approx 0‰$, and relative low, often negative values for $\delta^{18}O$, because local waters in the Atacama typically have negative $\delta^{18}O$ (Fritz *et al*., 1981; Aravena *et al*., 1999; Uribe *et al*., 2015; Jordan *et al*., 2018; Surma *et al*., 2018; Magaritz *et al*., 1989; Fritz *et al*., 1981; Cortecci *et al*., 2005; Cervetto, 2012; CMDIC, 2012; Lopez *et al*., 2014; Uribe *et al*., 2015; Jayne *et al*., 2016; Scheihing *et al*., 2017; Surma *et al*., 2018; Figure 7.3A).

We observe that the modification in triple-oxygen isotope signature in Atacama nitrates varies depending on the type of nitrates deposit (Figure 7.3A). Type-i and type-iia deposits exhibit $\Delta^{17}O$ and $\delta^{18}O$ values close to those of atmospheric nitrate, consistent with the dominant direct accumulation of atmospheric nitrate and minimal post-depositional modification. In contrast, type-iib and type-iic deposits show slightly lower $\Delta^{17}O$ and $\delta^{18}O$ values, consistent with partial isotopic exchange with local waters and/or hydrothermal fluids in geologically active settings such as Oficina Domeyko, Santa Rita, and Germania (Figures 7.1A-B; 7.3). Viewed within the framework above, the most parsimonious explanation for these systematic offsets is best explained by progressive overprinting of an originally atmospheric nitrate signal by local water–nitrate interaction in more dynamic, hydrothermally influenced settings. These post-depositional modifications are discussed below in detail in section 8.3.

Nitrogen isotopes ($\delta^{15}N$) provide an additional constraint on nitrate sources and post-depositional processes. Atmospheric N_2 is defined at $\delta^{15}N=0‰$ (Hoefs, 2018; Li, 2024), while atmospheric nitrate typically ranges from about -15 and -1‰ at mid and tropical latitudes, with occasional values up to +10‰ (Patris *et al.*, 2007; Morin *et al.*, 2009; Savarino *et al.*, 2013; Reich and Bao, 2018). NO_x produced by lightning in volcanic

plumes spans $\delta^{15}N$ values from -6 to +15‰ (Aroskay *et al*., 2024). In contrast, nitrate produced or recycled by microbial processes (e.g., denitrification, nitrification) commonly reaches positive $\delta^{15}N$ values up to +30‰, except for the final step of nitrification (nitrite oxidation), which can generate relatively low $\delta^{15}N$ down to -13‰, due to inverse kinetic isotope effects (Casciotti, 2009; Hoefs, 2018).

Previous works on Atacama nitrates reported $\delta^{15}N$ between -5 and +5‰, interpreted as reflecting limited microbial consumption under strongly oxidizing, organic-poor conditions (Böhlke *et al*., 1997; Melchiorre *et al.,* 2018; Reich and Bao, 2018). Our data fall within and slightly extend this range, with $\delta^{15}N$ values between −8‰ and +4‰ (Figure 7.4-7.5). $\delta^{15}N$ correlates positively with $\delta^{18}O$, in contrast to the negative mixing trends expected where atmospheric nitrate is substantially overprinted by biological cycling (e.g., Jackson *et al*., 2015) and differs from the marine-influenced signatures of coastal soils in the Antofagasta Region (Ewing *et al.,* 2007). These values are distinctly lower than those typical of denitrified or strongly recycled nitrate (+10 to +30; Casciatti, 2009; Hoefs, 2018; Reich and Bao, 2018) and instead lie within the envelope of atmospheric nitrate and lightning-derived NO_x (Figure 7.5).

Volcanic lightning could, in principle, generate light $\delta^{15}N$ signals, but if it were a dominant nitrate source, its isotopic fingerprint should be expressed both in veins-type deposits (type-iic) and in sedimentary deposits (type-i; Figure 7.3B), because nitrate originally hosted in tephra would be leached and redistributed into the aquifer, subsequently concentrating in alluvial deposits (type-i). This pattern of low $\delta^{15}N$ values is not observed in sedimentary deposits, indicating that volcanic lightning is unlikely to be the primary explanation for the light $\delta^{15}N$ signatures in the type-iic deposits.

Rather, the study by Aroskay *et al*. (2024) highlights the large natural variability in atmospheric nitrate $\delta^{15}N$, suggesting that the light nitrogen isotopic values in the type-iic deposits may reflect past variability in atmospheric sources or oxidation pathways, rather than volcanic inputs.

Taken together, the coexistence of high $\Delta^{17}O$ anomalies (+13 to +22‰) and relatively light $\delta^{15}N$ (−8 to +4‰) across all deposit types indicates that the Atacama nitrate was derived predominantly from the photochemical oxidation of atmospheric NO_x—possibly including a minor contribution from lightning-generated NO_x during episodes

of enhanced volcanic activity—and then preserved under long-term hyperarid conditions with negligible biological overprinting (Figures 7.2–7.5).

8.2 Volcanic Source

While the oxygen and nitrogen isotopic composition of the Atacama nitrates clearly demonstrates a predominantly atmospheric origin, the geological record preserves evidence for additional processes that modified, concentrated, or remobilized these deposits. Among them, volcanic and hydrothermal systems appear to have played a secondary but significant role in introducing and redistributing nitrate within the crust. The following discussion examines the volcanic contribution, which also provides a natural link to the subsequent hydrothermal recycling mechanisms discussed in Section 8.3.

Although the isotopic evidence discussed above supports a dominantly atmospheric origin for the Atacama nitrate deposits, field observations, mineralogical data, and isotopic compositions collectively suggest that volcanic and hydrothermal activity contributed to the formation, recycling, and redistribution of nitrate.

Field observations indicate multiple structures and alteration features in the host rock and veins that are consistent with hydrothermal activity. In the Tarapacá Region, Oficina Santa Rita (Figure 5.2) shows intensive oxidation and fracturing of the host rock, whereas Oficina Germania (Figure 5.5) displays advanced hydrothermal alteration characterized by strong red coloration, complete weathering of the andesite host rock, and fibrous nitrate veins (Figure 5.5 I-J). The presence of oxidized vents at the surface (Figure 5.5 M-O) indicates the location of former hydrothermal conduits.

In the Antofagasta Region, Cerro Birrete provides a clear example of synchronic volcanic activity with lacustrine sedimentation (lacustrine sediments underlying andesitic lava). The red coloration of lacustrine sediments due to oxidation (Figure 5.6-5.7), the occurrence of volcanic bombs deforming the host sediments (Figure 5.7B), inverse faults produced by loading pressure from overlying andesitic lava (Figure 5.7C), pillow-lava morphologies (Figure 5.6 A, E-F; 5.7A), thick travertine veins cutting the lacustrine sequences (Figure 5.7A), and the paleo-conduits generated by faulting that allowed hydrothermal fluids to circulate (Figure 5.6 F) collectively demonstrated

that the lake was contemporaneous with volcanic activity during at least the Late Cretaceous-Palaeocene (Chong *et al.,* 1994; Riffo, 2020).

The measured nitrate concentration—14 mg/g in red shale from Cerro Birrete's lacustrine sedimentary sequence and 30-50 mg/g associated conglomerates and sandstone (Table A3.1)—indicates a substantial nitrate input into the central depression before the Cretaceous-Palaeocene transition, likely associated with synchronic volcanic activity. Additionally, the presence of nitrate-bearing (Figure 5.9) within Paleocene-Eocene rhyolites (Marinovic, 2007) from Oficina Domeyko, containing up to 16 mg/g nitrate (Table A3.1), provides further evidence for nitrate deposition during periods of active volcanism.

Raman spectroscopy analyses reveal nitratine ($NaNO_3$), epsomite ($MgSO_4 \cdot 7H_2O$), and minor Fe-oxide/erdite ($NaFeS_2 \cdot 2H_2O$) as exsolution or alteration phases within rhyolitic host rocks from Oficina Domeyko (Figure 7.6). This alteration texture and mineral assemblage implies that nitrate-bearing fluids or gases were present either (1) during late-magmatic crystallization, trapped within an exsolved vapor phase (Edmonds and Wallace, 2017), or (2) during subsequent hydrothermal alteration (Miami and Geshi, 2025).

Such occurrences suggest that magmatic degassing released oxidized nitrogen and sulfur species, which subsequently combined with oxygen-bearing volatiles to condensate as nitrate and sulfate during cooling and exsolution (Edmonds and Wallace, 2017). Alternatively, nitrate minerals have precipitated at the interface between rhyolitic host rock and circulating hydrothermal fluid under hydrostatic or near-surface conditions after volcanic rocks were emplaced (Miami and Geshi, 2025).

Importantly, fixed-nitrogen species are demonstrably present in Andean volcanic plumes: HNO_3 in the vapor phase has been measured at Villarrica and Lascar volcanoes, with HNO_3/SO_2 ratios up to 0.07, providing a nitrate precursor near vents (Mather *et al.,* 2004). However, the absence of NO_3^- in natural glasses or melts indicates that direct emission of nitrate from a magmatic phase is unlikely; molecular N_2 is the dominant magmatic nitrogen species. The observed HNO_3 is therefore best interpreted as the oxidation product of NO formed by high temperature reactions between atmospheric or magmatic N_2 and O_2 (Mather *et al.,* 2004).

The associated Mg-sulfate (epsomite; Figure 7.6) is consistent with acid-sulfate alteration and condensation regimes typical of shallow hydrothermal–fumarolic

systems in northern Chile (Tassi *et al*., 2010; Minami & Geshi, 2025). Hence, the nitratine found as exsolution within rhyolitic rocks at Oficina Domeyko most likely formed through precipitation from hydrothermal, nitrate-rich fluids under near-surface atmospheric conditions, rather than direct magmatic degassing.

Sulfur isotope data ($\delta^{34}S$) further support a volcanic sulfur contribution. The $\delta^{34}S$ values of thenardite (Na_2SO_4) from Aguas Blancas (−1 to −2‰), sulfate from associated nitrate-veins in Oficina Domeyko (−0.30 to −0.80‰), and the rhyolitic host rock (−0.60‰) are significantly lighter than typical marine sulfate values (+21‰), or oxidized DMS sources (+18.9 to +20.3‰). Instead, they are consistent with volcanic SO_2 degassing and subsequent oxidation (-7 to +10‰), like the isotopic composition observed in the El Tatio geothermal field (-9.7 to 4.4‰) and the Thenardites from Atacama Desert soils (-0.9 to +5.2; Figure 7.5; Klipsch *et al*., 2023). The sulfur isotopic coherence among nitrate, sulfate, and rhyolite therefore indicates a volcanic influence within the Atacama nitrate cycle.

However, the isotopic signatures of the nitrates themselves—$\delta^{15}N$ = −8‰ to +4‰ and $\Delta^{17}O$ = +13‰ to +22‰—cannot be explained solely by volcanic emission or in situ lightning fixation. The strong positive $\Delta^{17}O$ anomalies observed in the Atacama samples can only result from photochemical oxidation of NO_x in the atmosphere, mediated by ozone (O_3) and other oxidants (Thiemens & Heidenreich, 1983; Michalski *et al*., 2003; Morin *et al.,* 2007; Savarino *et al*., 2013). Thus, even if volcanic emissions supplied the NO_x precursors, the formation of nitrate occurred through atmospheric photochemical reactions rather than direct magmatic processes.

Volcanic outgassing and lightning fixation likely served as episodic atmospheric sources of reactive nitrogen during periods of intense volcanism (Oyarzún and Oyarzún, 2007; Mather *et al.,* 2004; Aroskay *et al*., 2024). Elkins *et al.* (2006) demonstrated that nitrogen isotopes in volcanic and geothermal volatiles from the Nicaraguan volcanic front record variable contributions from mantle and sedimentary nitrogen, with $\delta^{15}N$ values from −3‰ to +7‰ depending on sediment input. This isotopic variability mirrors the low $\delta^{15}N$ values found in the Atacama vein deposits and supports the interpretation that volcanic-sourced NO_x mixed with atmospheric species before deposition.

While the isotopic evidence in the Atacama does not indicate a dominant volcanic signature, mechanisms such as volcanic lightning fixation and plume-derived HNO_3

production could have contributed to episodic NO_x enrichment in the atmosphere, enhancing the nitrate cycle over geological time.

Finally, the relationship between $\Delta^{17}O$ and $\delta^{18}O$ (Figure 7.3) indicates post-volcanic recycling of atmospheric nitrate by fossil hydrothermal fluids. In vein-type deposits (type-iic), $\Delta^{17}O$ values are slightly lower than those of primary atmospheric nitrate and trend toward the isotopic composition of fossil hydrothermal waters (black regression line in Figure 7.3). This pattern suggests partial oxygen isotope exchange between pre-existing atmospheric nitrate and hydrothermal fluids circulating through host rocks. The same fluids may have remobilized and reprecipitated nitrate, forming the observed nitratine-bearing assemblages while preserving the original atmospheric $\Delta^{17}O$ and light $\delta^{15}N$ signatures.

This isotopic and mineralogical evidence bridges the volcanic contribution with the subsequent hydrothermal reworking of nitrate deposits, which is discussed in detail in the following section.

8.3 Hydrothermal Recycling

Although the primary isotopic signatures point to an atmospheric source (Section 8.1), post-depositional hydrothermal processes may have partially modified the oxygen isotope composition, particularly in the vein-type deposits hosted in volcanic and sedimentary rocks (type-iic). This possibility is examined below.

Two processes can deplete $\Delta^{17}O$ values from their atmospheric signature after deposition. (1) Microbial denitrification reduces $\Delta^{17}O$ toward 0‰ as oxygen atoms in nitrate are exchanged or lost through stepwise reduction, leaving the residual nitrate enriched in ^{15}N (Reich and Bao, 2018). In arid environments, this effect is limited by water availability but may occur episodically in porewaters or shallow groundwater. (2) Nitrate-water oxygen isotope exchange, which partly equilibrates $\delta^{18}O$ in nitrate with the $\delta^{18}O$ of water. This exchange is negligible near 25°C and neutral pH but accelerates under acidic and higher-temperature conditions (Kaneko and Poulson, 2013)—conditions typical of hydrothermal (Aguilera, 2008; Tassi *et al*., 2010; Aguilera *et al.,* 2016) and porphyry-Cu systems in the Atacama Desert (Sillitoe, 2010).

The nitrogen isotopic composition ($\delta^{15}N$ = −8‰ to +4‰; Figure 7.4) varies systematically with deposit type, showing a marked depletion in $\delta^{15}N$ for type-iic

deposits. This pattern excludes microbial denitrification as the dominant fractionating process and is instead consistent with abiotic oxygen exchange without major nitrogen loss (Shen *et al*., 2022), possibly coupled with limited nitrification/denitrification cycles in transient, thin water films. Similar isotopic behavior has been reported in other Atacama profiles where $\delta^{15}N$ stratifies with leaching and remobilization under scarce meteoric recharge rather than sustained microbial processing (Melchiorre *et al*., 2018).

A positive correlation between $\delta^{18}O$ and $\Delta^{17}O$ defines a positive correlation for all deposit types (Figure 7.3). Type-iic deposits display lower $\delta^{18}O$ and $\Delta^{17}O$ values than atmospheric or sedimentary nitrate (type-i and type-iia), requiring interaction with a reservoir having $\Delta^{17}O \approx 0‰$ and variable $\delta^{18}O$, such as local Atacama waters (Fritz *et al.* 1981; Magaritz *et al.* 1989; Aravena *et al*. 1999; Cortecci *et al.* 2005; Leybourne & Cameron, 2006; Cervetto, 2012; CMDIC, 2012; Lopez *et al.*, 2014; Uribe *et al.*, 2015; Jayne *et al.*, 2016; Scheihing *et al.,* 2017; Jordan *et al*. 2018; Surma *et al.* 2018; Voigt *et al*., 2021).

Modern meteoric Atacama waters (rain, fog, and groundwater) yield negative $\delta^{18}O$; while fossil hydrothermal waters associated with porphyry systems are ^{18}O-enriched relative to the meteoric waters (Figure 7.3). Groundwaters from northern Chile, such as those in the Spence porphyry district, show Na–Cl composition, high salinity (≥25 g/L up to 145 g/L, in exceeding seawater), and isotopic displacement from the local meteoric water line toward heavier $\delta^{18}O$ —diagnostic of mixing and prolonged high-temperature water–rock interaction along deep faults (Leybourne & Cameron, 2006).

Crucially, the trend observed in nitrate samples (Figure 7.3) converges toward the isotopic field of fossil hydrothermal waters (Leybourne & Cameron, 2006). This convergence implies oxygen isotope exchange between the nitrate and the circulating hydrothermal fluids, likely during reprecipitation or recrystallization. Using the regression equation for all data (Figure 7.3), $\delta^{18}O$ extrapolates to ~2.5‰ when $\Delta^{17}O$ = 0‰—closely matching the average $\delta^{18}O$ of fossil hydrothermal waters (2.9‰)—further supporting the role of hydrothermal water–rock–nitrate interaction in modifying the bulk isotopic composition.

The rate of oxygen exchange between nitrate and water increases sharply with temperature and acidity; at ~25 °C and neutral pH it is negligible on geological timescales but becomes significant under low pH and elevated temperatures (Kaneko

and Poulson, 2013). Fluid geochemistry across northern Chile shows discharges up to ~270ºC from magmatically influenced brine reservoirs, with total dissolved solid (TDS) up to 10 g/L (Tassi *et al.,* 2010). Experimental work further demonstrates that boiling of H_2O–NaCl brines drives salt hydrolysis, partitioning HCl into vapor and generating condensates with pH ≈ 2–3 (Ballhaus *et al.,* 2019). Such high salinity, low pH, and elevated temperature provide the conditions necessary to accelerate nitrate-water O-exchange, allowing type-iic veins to shift toward the fossil hydrothermal $\delta^{18}O$ field while $\Delta^{17}O$ is simultaneously suppressed (Figure 7.3).

Fumarolic and volatile-rich hydrothermal systems in volcanic zones are known to generate salt-bearing sublimates and associated alteration (Aguilera *et al*., 2016). Although direct evidence of nitratine exsolution from magmatic or fumarolic melts is rare, Raman data from Ocidina Domeyko in this study reveal nitratine exsolution within rhyolitic host rock (Figure 7.6), suggesting that nitrate-bearing hydrothermal fluids or melts may indeed have been present in the Atacama nitrate cycle.

Geological field observations further support hydrothermal recycling in type-iic deposits. Nitrate veins cutting volcanic and sedimentary rocks occur in altered zones (Figure 5.2; 5.5), locally forming stalactitic morphologies within cavities (Figure 5.9)—features consistent with fracture-controlled fluid circulation and pulsed mineral deposition. Ductile textures and internal lamination within type-iic veins (Figure 5.9) indicate multi-event filling and recrystallization, compatible with thermal and chemical oscillations during fluid ingress. The proximity of nitrate vein deposits to Cu-Au deposits of the Paleocene-Eocene Metallogenic belt (Figure 2.1; Kojima and Campos, 2011) reinforces this interpretation. The zoned sequence of nitrate, Ca-sulfates, Na-chlorides, and Na-sulfates (Table A3.2) reflects precipitation from saline oxidized hydrothermal solutions under near-surface conditions (Leybourne & Cameron, 2006), following solubility trends comparable to those in hydrothermal ore zoning (Crerar *et al.,* 1985).

Collectively, the isotopic, mineralogical, and field evidence converge on a consistent interpretation: fracture-controlled, hot, and saline fluids intermittently circulated through nitrate-bearing bedrock, dissolving, transporting, and reprecipitating pre-existing atmospheric nitrate. The observed isotopic trends, vein textures, and structural relationships are precisely those expected if hydrothermal fluids acted as agents of redistribution rather than as sources of new nitrate formation. During their

circulation, these fluids partially equilibrated the oxygen isotopic composition of nitrate with the isotopically heavier hydrothermal water, lowering $\Delta^{17}O$ and shifting $\delta^{18}O$ toward values characteristic of the fluid.

This post-depositional hydrothermal recycling provides a coherent explanation for the spatial and isotopic diversity among Atacama nitrate deposit types. Sedimentary deposits (type-i) preserve the most pristine atmospheric signal; type-iia and type-iib deposits represent limited remobilization by meteoric waters, whereas vein-type deposits (type-iic) record a mixed atmospheric–hydrothermal signature resulting from fluid-mediated reprecipitation in tectonically active zones. The persistence of nitrate–sulfate–chloride assemblages demonstrates that hydrothermal fluids did not destroy nitrate but rather concentrated and stabilized it through mineral precipitation under oxidizing, hyperarid conditions.

In summary, hydrothermal recycling emerges as a secondary yet fundamental process in the geological evolution of the Atacama nitrate system—responsible for the isotopic modification, local enrichment, and mineral reorganization of an originally atmospheric nitrate reservoir within volcanic and structurally dynamic terrains.

9 Conclusions: The Geological Super-Cycle of Atacama Nitrates

The isotopic, mineralogical, and geological evidence presented in this study defines a two-stage model for the formation and evolution of nitrate deposits in the Atacama Desert. This cycle integrates primary atmospheric deposition and secondary hydrothermal recycling, which together account for the spatial, mineralogical, and isotopic diversity of the nitrate-bearing formations across northern Chile.

(1) Primary atmospheric deposition.

Nitrogen was accumulated in the atmosphere through geological time, fixed as NO_x by electrical discharges (storm and volcanic lightning; Aroskay *et al*., 2024) and locally via atmospheric oxidation of volcanic or magmatic gases (e.g., HNO_3; Elkins *et al.*, 2006), generating an abiotic atmospheric print in Atacama nitrates ($\delta^{15}N$ = −8‰ to +4‰). NO_x species will follow different oxidation pathways during day or night (Equations 3.5 – 3.9; Michalski *et al*., 2003; Morin *et al*., 2007; Savarino *et al.,* 2013), depending on the atmospheric composition. If atmospheric nitrate is derived from photochemical oxidation of NO_x by O_3, it will carry a MIF highly enriched in $\Delta^{17}O$ (Michalski *et al*., 2003; Patris *et al.,* 2007; Morin *et al.,* 2009; Savarino *et al*., 2013; Reich and Bao, 2018). Whereas if atmospheric nitrate is generated via NO_x oxidation by OH or another tropospheric radical carrying $\Delta^{17}O \approx 0‰$, then the generated nitrate will also carry a $\Delta^{17}O \approx 0‰$ (Aroskay *et al.,* 2024). The Atacama Desert Nitrate Deposits present high $\Delta^{17}O$ anomalies (+13‰ to +22‰; Figure 7.3) in all deposit types, confirming a mass-independent oxygen isotopic signature derived from photochemical oxidation of NO_x by ozone in the atmosphere, as suggested by other authors before (Böhlke *et al.,* 1997; Michalski *et al*., 2004; Melchiorre *et al.,* 2018). This atmospheric deposition will be followed by progressive precipitation in the high Andes, triggering groundwater transportation, dissolution, and infiltration in shallow aquifers, generating evaporative enrichment through capillarity in an endorheic basin (Central Depression); triggered by increasing aridity and tectonic uplift (Pérez-Fodich *et al.* 2014; Reich and Bao, 2018).

This mechanism led to the formation of sedimentary (type-i) nitrate deposits, which preserve the original atmospheric isotopic signal. Progressively, with meteoric water circulation the nitrates were locally redistributed, generating pure nitrate mantos

cutting the sedimentary nitrate (type-iia; Figure 7.3), carrying similar isotopic signatures to the type-I deposit. Tectonic activity concurrent with meteoric water circulation would then generate neptunic-dykes (type-iib deposits), with their shared atmospheric source reflected in their isotopic signatures.

These deposits represent the primary geochemical sink of atmospheric nitrate in hyperarid continental settings, their preservation facilitated by the extreme climatic stability and minimal biological activity of the Atacama Desert.

(2) Secondary hydrothermal recycling and volcanic activity.

Post-depositional volcanic/magmatic activity during the Paleocene-Eocene (Chong, 1994; Marinovic, 2007; Chong *et al.,* 2020) generated hot, saline hydrothermal fluids that were circulated through fault systems. These Na–Cl–rich waters, with average $\delta^{18}O \approx +2.9‰$ and high TDS (Leybourne & Cameron, 2006), dissolved and reprecipitated pre-existing atmospheric nitrate in fractures and cracks from volcanic or sedimentary host rocks, generating the veins type-iic deposits.

The positive correlation between $\delta^{18}O$ and $\Delta^{17}O$ in all nitrate types and the convergence of nitrate $\delta^{18}O$–$\Delta^{17}O$ values toward those of fossil hydrothermal waters (Figure 7.3), indicates oxygen isotope exchange between nitrate and ^{18}O-enriched hydrothermal waters during recycling. The occurrence of nitratine exsolution within rhyolites (Figure 7.6), and the low $\delta^{34}S$ values in associated sulfates (Figure 7.5) all point to the participation of deep-seated, possibly magmatic–hydrothermal systems. Such fluids acted as agents of redistribution rather than generation, modifying the oxygen isotope composition through partial exchange while concentrating nitrate in tectonically controlled vein systems.

Together, these processes define a two-mechanism geological cycle for nitrate formation in the Atacama Desert.

Primary atmospheric deposition and preservation of photochemically produced nitrate under extreme aridity, forming sedimentary (type-i) deposits (Figure 8.1A).

Secondary remobilization and reprecipitation by hydrothermal fluids, modifying the isotopic signature and concentrating nitrate into structural traps (type-iic). Alternatively, a minor contribution from volcanic lightning during volcanic activity (Figure 8.1B).

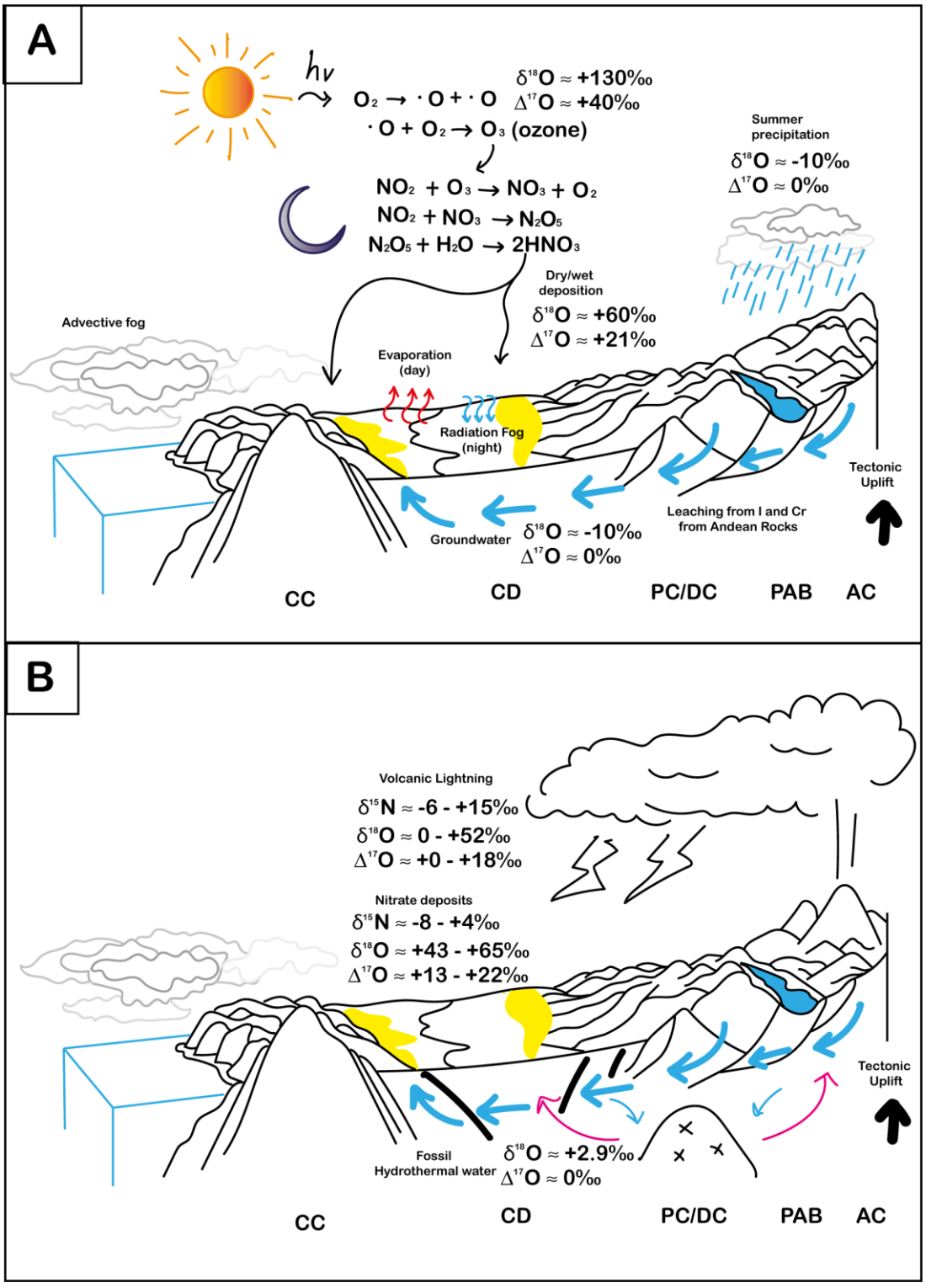

Figure 8.1: Conceptual model for the formation and modification of Atacama nitrate deposits. (A) Primary atmospheric deposition and preservation of photochemically produced nitrate under long-term hyperaridity, leading to the accumulation of sedimentary type-i deposits. (B) Secondary remobilization and reprecipitation by hydrothermal fluids, which alter isotopic signatures and concentrate nitrate within structural traps to form type-iic deposits; a minor contribution from volcanic lightning during periods of volcanic activity is also possible. Nitrate deposits are shown in yellow. CC: Coastal Cordillera, CD: Central Depression, PD/DC: Precordillera/Domezko Cordillera, PAB: Pre-Andean basins, AC: Andes Cordillera.

This two-mechanism framework reconciles the isotopic, mineralogical, and spatial diversity of the Atacama nitrate deposits. It demonstrates that the world's largest nitrate accumulations record not only atmospheric chemistry but also the tectonic and magmatic evolution of the Andean margin — a coupled surface–deep Earth process that has operated since at least the late Cenozoic.

10 Outlook and Future Research directions

Although this study has established a two-stage geological model cycle for the formation of Atacama nitrate deposits —combining primary atmospheric deposition and secondary hydrothermal recycling— several key questions remain unresolved, offering opportunities for future investigation.

Besides the geological observations and stable isotope analysis, timing and rates of nitrate deposition and recycling remain poorly constrained. The chronological framework for nitrate accumulation and subsequent hydrothermal modification could be determined by high-precision geochronology (e.g., U–Th/He, (U–Th)/He, $^{40}Ar/^{39}Ar$, or U–Pb dating) in the different deposit types, especially type-i and type-iic. This information could help understand whether hydrothermal remobilization occurred synchronously with Paleocene–Eocene magmatism or as a younger reactivation event. The age of nitrate deposits also has paleoclimatic implications, since the accumulation of nitrate is reflected in a long-term hyperaridity (Voigt *et al*., 2020). Coupled radiogenic and stable isotope studies would clarify the tempo of nitrate deposition versus recycling, and the onset of the Atacama hyperaridity.

Despite the clear atmospheric origin of the Atacama nitrates, the exact climatic and atmospheric conditions that allowed their long-term preservation under hyperaridity remain debated. Coupled atmospheric–geochemical modeling (e.g., Michalski *et al*., 2003), integrating $\Delta^{17}O$–$\delta^{15}N$–$\delta^{18}O$ systematics, could reconstruct the evolution of tropospheric chemistry, lightning frequency, and volcanic emissions. Together with geochronology, it would help to reconstruct the atmospheric dynamics of nitrogen-bearing compounds in the past.

To understand the proportion of nitrogen fixation by long-term atmospheric deposition and volcanic lightning fixation (Contamine *et al*., 2025), it is fundamental to analyze the chemical and isotopic composition of ash layers in the Atacama Desert in the same basin as nitrate deposits. In that case, we can differentiate nitrate deposits from volcanic fixation and nitrate deposits from long-term atmospheric deposition. It could also be interesting to do the study in a more recent volcanic deposit and quantify the actual abiotic nitrate fixation in the present-day Atacama Desert.

The study of isotopic composition ($\Delta^{17}O$–$\delta^{34}S$–$\delta^{18}O$) on sulfates associated with nitrate deposits would contribute to the understanding of the sulfate source contributions and detect low water availability in nitrate deposits, also to identify in-situ biological activity (Klipsch *et al.,* 2023). Especially, the knowledge of the $\delta^{18}O$ values of two cogenetic phases, in this case nitrate and sulfates, allow to determine the temperature of formation (Sharp, 2017), thus contributing to the understanding of hydrothermal fluids that recycle the nitrates.

Chemical and isotopic studies from groundwaters associated with nitrate deposits would help to constrain the water sources and water-rock reaction, and their role in the distribution and concentration of nitrates (Leybourne & Cameron, 2006). Additionally, the limited water resources in the Atacama Desert for drinking water would also be a motivation for hydrological studies for better management of water resources in the Atacama Desert.

Petrographic, Raman, and in situ isotopic mapping at the microscale could resolve whether isotopic heterogeneities within type-iic veins reflect sequential fluid pulses or partial equilibration within a single hydrothermal episode. Further studies on fluid inclusions would provide a better characterization of the composition and origin of the hydrothermal fluids.

Petrological studies on the exsolution from Oficina Domeyko rhyolites could help in better understanding the role of volcanic/magmatic activity in nitrates recrystallization, and micro to macro scale processes of nitrate redistribution.

References

Aguilera, F. (2008). *Origen y naturaleza de los fluidos en los sistemas volcánicos, geotermales y termales de baja entalpía de la Zona Volcánica Central (ZVC) entre los 17°43'S y 25°10'S. Chile*: [PhD thesis]. Universidad Católica del Norte.

Aguilera, F., Layana, S., Rodríguez-Díaz, A., González, C., Cortés, J., & Inostroza, M. (2016). Hydrothermal alteration, fumarolic deposits and fluids from Lastarria Volcanic Complex: A multidisciplinary study. *Andean Geology, 43*(2), 166–196.

Amedro, D., Berasategui, M., Bunkan, A. J. C., Pozzer, A., Lelieveld, J., & Crowley, J. N. (2020). Kinetics of the OH + NO2 reaction: effect of water vapour and new parameterization for global modelling. *Atmospheric Chemistry And Physics, 20*(5), 3091-3105.

Amilibia, A., Sàbat, F., McClay, K. R., Muñoz, J. A., Roca, E., & Chong, G. (2008). The role of inherited tectono-sedimentary architecture in the development of the central Andean mountain belt: Insights from the Cordillera de Domeyko. *Journal of Structural Geology*, *30*(12), 1520-1539.

Aravena, R., Suzuki, O., Peña, H., Pollastri, A., Fuenzalida, H., & Grilli, A. (1999). Isotopic composition and origin of the precipitation in Northern Chile. *Applied Geochemistry*, *14*(4), 411-422

Aroskay, A., Martin, E., Bekki, S., Pennec, J. L., Savarino, J., Temel, A., Manrique, N., Aguilar, R., Rivera, M., Guillou, H., Balcone-Boissard, H., Phelip, O., & Szopa, S. (2024). Geological evidence of extensive N-fixation by volcanic lightning during very large explosive eruptions. *Proceedings Of The National Academy Of Sciences, 121*(7).

Baeza, L., & Astudillo, N. (2019). *Carta Pedro de Valdivia, Región de Antofagasta* [Geological map, 1:100,000]. Servicio Nacional de Geología y Minería (SERNAGEOMIN). Carta Geológica de Chile, Serie Geología Básica, 206.

Ballhaus, C., Gäb, F., Garbe-Schönberg, D., & Staubwasser, M. (2019). Effect of boiling on the acidity of hydrothermal solutions. *Contributions to Mineralogy and Petrology, 174*(1).

Bland, J. M., & Altman, D. G. (1986). Statistical methods for assessing agreement between two methods of clinical measurement. *The Lancet, 327*(8476), 307–310.

Böhlke, J.K., Ericksen, G.E., and Revesz, K. (1997). Stable isotope evidence for an atmospheric origin of desert nitrate deposits in northern Chile and southern California, USA: *Chemical Geology*, v. *136*, p. 135–152.

Böhlke, J. K., Mroczkowski, S. J., & Coplen, T. B. (2003). Oxygen isotopes in nitrate: new reference materials for 18O:17O:16O measurements and observations on nitrate-water equilibration. *Rapid Communications In Mass Spectrometry, 17*(16), 1835-1846.

Casciotti, K. L. (2009). Inverse kinetic isotope fractionation during bacterial nitrite oxidation. *Marine Chemistry and Geochemistry, Woods Hole Oceanographic Institution*.

CMDIC (2012) Estudio de los tiempos de residencia del agua subterránea en el entorno de la Compañía Minera Doña Inés de Collahuasi.

Cereceda, P., Larrain, H., Osses, P., Farías, M., Egaña, I. (2008). The spatial and temporal variability of fog and its relation to fog oases in the Atacama Desert, Chile. *Atmos. Res. 87*, 312–323.

Cereceda, P., Osses, P., Larrain, H., Farías, M., Lagos, M., Pinto, R., Schemenauer, R.S. (2002). Advective, orographic and radiation fog in the Tarapacá region, Chile. *Atmos. Res*. *64*, 261–271.

Cervetto, M. (2012). *Caracterización Hidrogeológica e Hidrogeoquímica de las Cuencas: Salar de Aguas Calientes 2, Puntas Negras, Laguna Tuyajto, Pampa Colorada, Pampa las Tecas y Salar el Laco, II Región, Chile.* [Tésis para optar al título de Geólog, Universidad de Chile]. https://repositorio.uchile.cl/handle/2250/112067

Chong, G., Demergasso, C., Urrutia, J., Vargas, A. (2020). El "dominio salino" del Norte de Chile y sus yacimientos de minerales industriales. *Boletín de la Sociedad Geológica Mexicana*, *72*(3), A020720. http://dx.doi.org/10.18268/BSGM2020v72n3a020720.

Chong. C. (1994). The nitrate deposits of Chile. *Tectonics of the Southern Central Andes: Structure and Evolution of an Active Continental Margin*, 303-316.

Contamine, D., Martin, E., Aroskay, A., Bekki, S., Bindeman, I., Savarino, J., & Szopa, S. (2025). Geological record of atmospheric nitrogen fixation during explosive supereruptions: The case of Tecopa Basin, California*. Journal of Geophysical Research: Solid Earth.*

Coplen, T. B. (2011). Guidelines and recommended terms for expression of stable-isotope-ratio and gas-ratio measurement results*. Rapid Communications in Mass Spectrometry, 25(17), 2538–2560.*

Cortecci, G., Boschetti, T., Mussi, M., Lameli, C. H., Mucchino, C., & Barbieri, M. (2005). New chemical and original isotopic data on waters from El Tatio geothermal field, northern Chile. *Geochemical Journal*, *39*(6), 547-571.

Crerar, D. A., Wood, S., Brantley, S., & Bocarsly, A. B. (1985). Chemical controls on solubility of ore-forming minerals in hydrothermal solutions. *Canadian Mineralogist, 23*(3), 333-352.

Dunai, T. J., López, G. A. G., & Juez-Larré, J. (2005). Oligocene–Miocene age of aridity in the Atacama Desert revealed by exposure dating of erosion- sensitive landforms. *Geology*, *33*(4), 321-324.

Edmonds, M., & Wallace, P. J. (2017). Volatiles and Exsolved Vapor in Volcanic Systems. *Elements, 13*(1), 29–34.

Elkins, L. J., Fischer, T., Hilton, D. R., & Walker, J. (2006). Tracing nitrogen in volcanic and geothermal volatiles from the Nicaragua volcanic front. *Geochimica et Cosmochimica Acta, 70*(20), 5215–5235.

Ericksen, G.E. (1981). Geology and Origin of the Chilean Nitrate Deposits. *Geological survey professional paper*, 1-37.

Ericksen, G.E. (1983). The Chilean Nitrate Deposits. *American Scientist*, *71*(3), 366-374.

Evenstar, L.A., Hartley, A.J., Stuart, F.M., Mather, A.E., Rice, C.M., Chong, G. (2009). Multiphase development of the Atacama Planation Surface recorded by cosmogenic 3He exposure ages: Implications for uplift and Cenozoic climate change in Western South America. *Geology 37*, 27–30.

Evenstar, L.A., Mather, A.E., Hartley, A.J., Stuart, F.M., Sparks, R.S.J., Cooper, F.J. (2017). Geomorphology on geologic timescales: Evolution of the late Cenozoic Pacific paleosurface in Northern Chile and Southern Peru. *Earth- Science Rev*. *171*, 1–27.

Ewing, S. A., Michalski, G., Thiemens, M., Quinn, R. C., Macalady, J. L., Kohl, S., Wankel, S. D., Kendall, C., McKay, C. P., & Amundson, R. (2007). Rainfall limit of the N cycle on Earth. *Geophysical Research Letters, 34*(L11814).

Ferrando, R., Espinoza, F., Matthews, S., Cornejo, P., & Arévalo, C. (2013).0 *Carta Aguas Blancas, Región de Antofagasta* [Geological map, 1:100,000]. Servicio Nacional de Geología y Minería (SERNAGEOMIN). Carta Geológica de Chile, Serie Geología Básica, 160.

Fritz, P., Suzuki, O., Silva, C., & Salati, E. (1981). Isotope hydrology of groundwaters in the Pampa del Tamarugal, Chile. Journal Of Hydrology, *53*(1-2), 161-184.

Gázquez, F., & Claire, M. W. (2018). Triple oxygen isotope analysis of nitrate using isotope exchange – cavity ring-down laser spectroscopy. *Rapid Communications in Mass Spectrometry, 32*(22), 1949–1961.

Giavarina, D. (2015). *Understanding Bland Altman analysis. Biochemia Medica, 25*(2), 141–151.

Hartley, A. J., & Chong, G. (2002). Late Pliocene age for the Atacama Desert: implications for the desertification of western South America. *Geology*, *30*(1), 43-46.

Hartley, A.J., Chong, G., Houston, J., Mather, A.E. (2005). 150 million years of climatic stability: evidence from the Atacama Desert, northern Chile. *J. Geol. Soc. London*. *162*, 421–424.

Hayes, J. (2004). *An Introduction to Isotopic Calculations*. https://doi.org/10.1575/1912/27058.

Hoefs, J. (2018). Stable isotope Geochemistry. In *Springer textbooks in earth sciences, geography and environment*. https://doi.org/10.1007/978-3-319-78527-1.

Houston, J. (2006). Variability of precipitation in the Atacama Desert: Its causes and hydrological impact. *Int. J. Climatol*. *26*, 2181–2198.

Houston, J., Hartley, A.J. (2003). The central andean west-slope rainshadow and its potential contribution to the origin of hyper-aridity in the Atacama Desert*. Int. J. Climatol*. *23*, 1453–1464.

Jackson, W. A., Böhlke, J. K., Andraski, B. J., Fahlquist, L., and Bexfield, L. (2015). Global patterns and environmental controls of perchlorate and nitrate co-occurrence in arid and semi-arid environments. *Geochimica et Cosmochimica Acta, 74*(13), 3962–3981.

Jayne, R. S., Pollyea, R. M., Dodd, J. P., Olson, E. J., & Swanson, S. K. (2016). Spatial and temporal constraints on regional-scale groundwater flow in the Pampa del Tamarugal Basin, Atacama Desert, Chile. *Hydrogeology Journal*, *24*(8), 1921-1937.

Johnston, D. T., Gill, B. C., Masterson, A., Beirne, E., Casciotti, K. L., Knapp, A. N., & Berelson, W. (2014). Placing an upper limit on cryptic marine sulphur cycling. *Nature, 513*(7519), 530–533.

Jordan, T. E., Herrera, C., Godfrey, L. V., Colucci, S. J.,Gamboa., C., Urrutia, J.,González, G., & Paul, J. F. (2018). Isotopic characteristics and paleoclimate implications of the extreme precipitation event of March 2015 in northern Chile. *Andean Geology*, *46*(1), 1.

Kaneko, M., & Poulson, S. R. (2013). The rate of oxygen isotope exchange between nitrate and water. *Geochimica Et Cosmochimica Acta, 118*, 148-156.

Kendall, C., & Caldwell, E. A. (1998). Fundamentals of Isotope Geochemistry. In *Elsevier eBooks* (pp. 51-86). https://doi.org/10.1016/b978-0-444-81546-0.50009-4.

Klipsch, S. (2021). *Identifying Sulfate Sources and Recycling Processes in The Atacama Desert With Sulfur, Strontium , and Triple Oxygen Isotopes*. [PhD thesis]. Universität zu Köln. https://kups.ub.uni-koeln.de/63930/.

Klipsch, S., Herwartz, D., & Staubwasser, M. (2021). Optimizing sulfate pyrolysis triple oxygen isotope analysis for samples from desert environments. *Rapid Communications in Mass Spectrometry*, *35*(14).

Klipsch, S., Herwartz, D., Voigt, C., Münker, C., Chong, G., Böttcher, M. E., & Staubwasser, M. (2023). Sulfate sources, biologic cycling, and mobility in Atacama Desert soils revealed by isotope signatures. *Global And Planetary Change, 230,* 104290.

Kojima, S., & Campos, E. (2011). An overview of Chilean economic deposits. *SGA News,* (29), 1–16.

Koprivova, A., Kopriva, S. (2016). Sulfation pathways in plants. *Chem. Biol. Interact. 259*,23–30.

Leybourne, M. I., & Cameron, E. M. (2006). Composition of groundwaters associated with porphyry-Cu deposits, Atacama Desert, Chile: Elemental and isotopic constraints on water sources and water–rock reactions. *Geochimica Et Cosmochimica Acta*, *70*(7), 1616-1635.

Li, Y. (2024). *The origin and evolution of Earth's nitrogen. National Science Review, 11*(6), nwae201.

Lopez, L.; Cifuentes, J.; Cervetto, M.; Feuker, P.; Neira, H.; Troncoso, R.; Espinoza, C. (2014). Estudio Hidrogeológico de la Pampa del Tamarugal y cuencas vecinas, Región de Tarapacá. Servicio Nacional de Geología y Minería. Informe Registrado IR-14-58, 400 p., 1 Vol., 1 DVD anexo. Santiago.

Lucero, F. (2023). *Geología de los Yacimientos de Nitratos y Yodo del Sector de Aguas Blancas, Región de Antofagasta (387.475 mE - 393.846 mE y 7.747.782 mN – 7.768.636 mN)*. [Tesina para optar al grado de Geólogo no publicada]. Universidad Católica del Norte, Departamento de Ciencias Geológicas, Antofagasta.

Magaritz, M., Aravena, R., Peña, H., Suzuki, O., & Grilli, A. (1989). Water chemistry and isotope study of streams and springs in northern Chile. *Journal Of Hydrology*, *108*, 323-341.

Marinovic, N. (2007). *Carta Oficina Domeyko, Región de Antofagasta* [Geological map, 1:100,000]. Servicio Nacional de Geología y Minería (SERNAGEOMIN). Carta Geológica de Chile, Serie Geología Básica, XX.

Mather, T. A., Allen, A. G., Davison, B., Pyle, D. M., Oppenheimer, C., & McGonigle, A. J. S. (2004). Nitric acid from volcanoes. *Earth and Planetary Science Letters, 218*(1–2), 17–30.

McDonald, J. H. (2014). *Handbook of biological statistics (3rd ed.). Baltimore, MD: Sparky House Publishing.*

McKinney, C.R., McCrea, J.M., Epstein, S., Allen, H.A., Urey, H.C. (1950). Improvements in Mass Spectrometers for the Measurement of Small Differences in Isotope Abundance Ratios. *Rev. Sci. Instrum*. 21.

Melchiorre, E. B., Sickman, J. O., Talyn, B. C., & Noblet, J. (2017). Isotope stratigraphy: Insights on paleoclimate and formation of nitrate deposits in the Atacama Desert, Chile. *Journal Of Arid*

Environments, 148, 45-53.

Michalski, G., Savarino, J., Böhlke, J. K., & Thiemens, M. (2002). Determination of the Total Oxygen Isotopic Composition of Nitrate and the Calibration of a Δ17O Nitrate Reference Material. *Analytical Chemistry*, *74*(19), 4989-4993.

Michalski, G., Scott, Z., Kabiling, M., & Thiemens, M. H. (2003). First measurements and modeling of Δ17O in atmospheric nitrate. *Geophysical Research Letters*, *30*(16).

Michalski, G., Böhlke, J. K., & Thiemens, M. (2004). Long term atmospheric deposition as the source of nitrate and other salts in the Atacama Desert, Chile: New evidence from mass-independent oxygen isotopic compositions. *Geochimica et Cosmochimica Acta*, *68*(20), 4023-4038.

Minami, Y., & Geshi, N. (2025). Origins and significance of alteration textures in hydrovolcanic products from active volcanoes. *Earth, Planets and Space,* 77, 39.

Miranda, K.M., Espey, M.G., Wink, D.A. (2001). A rapid, simple spectrophotometric method for simultaneous detection of nitrate and nitrite. *Nitric Oxide Biol. Chem*. *5*, 62–71.

Morin, S., Savarino, J., Bekki, S., Gong, S., & Bottenheim, J. W. (2007). Signature of Arctic surface ozone depletion events in the isotope anomaly (Δ17O) of atmospheric nitrate. *Atmospheric Chemistry And Physics, 7*(5), 1451-1469.

Morin, S., Savarino, J., Frey, M. M., Domine, F., Jacobi, H., Kaleschke, L., & Martins, J. M. F. (2009). Comprehensive isotopic composition of atmospheric nitrate in the Atlantic Ocean boundary layer from 65°S to 79°N. *Journal Of Geophysical Research Atmospheres*, *114*(D5).

Oyarzun, J., & Oyarzun, R. (2007). Massive volcanism in the Altiplano-Puna volcanic plateau and formation of the huge Atacama Desert nitrate deposits: A case for thermal and electric fixation of atmospheric nitrogen. *International Geology Review, 49*(10), 962–968..

Patris, N., Cliff, S. S., Quinn, P. K., Kasem, M., & Thiemens, M. H. (2007). Isotopic analysis of aerosol sulfate and nitrate during ITCT-2k2: Determination of different formation pathways as a function of particle size. *Journal Of Geophysical Research Atmospheres*, *112*(D23)

Paul, D., Skrzypek, G., & Fórizs, I. (2007). Normalization of measured stable isotopic compositions to isotope reference scales — a review. *Rapid Communications in Mass Spectrometry, 21,* 3006–3014.

Pérez-Fodich, A., Reich, M., Álvarez, F., Snyder, G. T., Schoenberg, R., Vargas, G., Muramatsu, Y. & Fehn, U. (2014). Climate change and tectonic uplift triggered the formation of the Atacama Desert's giant nitrate deposits. *Geology*, *42*(3), 251-254.

Pollmann, T., Böttcher, M. E., & Giani, L. (2021). Young soils of a temperate barrier island under the impact of formation and resetting by tides and wind. *Catena,* 202, 105275.

Reich, M., & Bao, H. (2018). Nitrate deposits of the Atacama Desert: A marker of long-term hyperaridity. *Elements: An International Magazine of Mineralogy, Geochemistry, and Petrology, 14*(4), 251-256.

Riffo, C. (2020). *Nuevos Antecedentes Geológicos del Cretácico Superior-Paleógeno en la Depresión Central de la Región de Antofagasta. El caso de Cerro Birrete (7.447.300-7.456.000 mN y 427.600-441.100 mE), Norte de Chile*. [Tesina para optar al grado de Geóloga no publicada]. Universidad Católica del Norte, Departamento de Ciencias Geológicas, Antofagasta.

Ritter, B., Stuart, F.M., Binnie, S.A., Gerdes, A., Wennrich, V., Dunai, T.J. (2018). Neogene fluvial landscape evolution in the hyperarid core of the Atacama Desert. *Sci. Rep*. *8*, 1–16.

Savarino, J., Morin, S., Erbland, J., Grannec, F., Patey, M. D., Vicars, W., Alexander, B., & Achterberg, E. P. (2013). Isotopic composition of atmospheric nitrate in a tropical marine boundary layer. *Proceedings Of The National Academy Of Sciences*, *110*(44), 17668-17673.

Schauer, A. J., Kunasek, S. A., Sofen, E. D., Erbland, J., Savarino, J., Johnson, B. W., Amos, H. M., Shaheen, R., Abaunza, M., Jackson, T. L., Thiemens, M. H., & Alexander, B. (2012). Oxygen isotope exchange with quartz during pyrolysis of silver sulfate and silver nitrate. *Rapid Communications In Mass Spectrometry*, *26*(18), 2151-2157.

Scheihing, K., Moya, C., Struck, U., Lictevout, E., & Tröger, U. (2017). Reassessing Hydrological Processes That Control Stable Isotope Tracers in Groundwater of the Atacama Desert (Northern Chile). *Hydrology, 5*(1), 3.

Schween, J.H., Hoffmeister, D., Löhnert, U. (2020). Filling the observational gap in the Atacama Desert with a new network of climate stations. *Glob. Planet. Change, 184*, 103034.

SERNAGEOMIN, S. (2003). Mapa Geológico de Chile: versión digital. Servicio Nacional de Geología y Minería, Publicación Geológica Digital, 4.

Sepúlveda, F. A., Vásquez, P., & Quezada, A. (2014). *Cartas Patillos y Oficina Victoria, Región de Tarapacá* [Geologic map, 1:100,000]. Servicio Nacional de Geología y Minería. Serie Geología Básica No. 167-168.

Shen, J., Zerkle, A. L., & Claire, M. W. (2022). Nitrogen Cycling and Biosignatures in a Hyperarid Mars Analog Environment. *Astrobiology, 22*(2), 127-142.

Sharp, Z. (2017). *Principles of Stable Isotope Geochemistry, 2nd Edition*.

Sillitoe, R. H. (2010). Porphyry copper systems. *Economic Geology, 105*(1), 3–41.

Silva, L. I. (1977). *Geología de las Hojas Pisagua y Zapiga, I Región, Tarapcá, Chile* [Geologic map, 1:100,000]. Instituto de Investigaciones Geológicas. Carta Geológica de Chile No. 24.

Silva, S. R., Kendall, C., Wilkison, D. H., Ziegler, A. C., Chang, C. C. Y., & Avanzino, R. J. (2000). A new method for collection of nitrate from fresh water and the analysis of nitrogen and oxygen isotope ratios. Journal of Hydrology, 228(1–2), 22–36.

Skrzypek, G. (2012). Normalization procedures and reference material selection in stable H, C, N, O, S isotope analyses: An overview. *Rapid Communications in Mass Spectrometry, 26*(21), 2359–2379.

Surma, J., Assonov, S., Herwartz, D., Voigt, C., & Staubwasser, M. (2018). The evolution of 17O-excess in surface water of the arid environment during recharge and evaporation. *Scientific Reports*, *8*(1).

Tassi, F., Aguilera, F., Darrah, T., Vaselli, O., Capaccioni, B., Poreda, R. J., & Delgado Huertas, A. (2010). Fluid geochemistry of hydrothermal systems in the Arica-Parinacota, Tarapacá and Antofagasta regions (northern Chile). *Journal of Volcanology and Geothermal Research, 192*, 1–15..

Thiemens, M. H., & Heidenreich, J. E. (1983). The Mass-Independent Fractionation of Oxygen: A Novel Isotope Effect and Its Possible Cosmochemical Implications. *Science, 219*(4588), 1073-1075.

Thiemens, M. H. (1999). Mass-Independent Isotope Effects in Planetary Atmospheres and the Early Solar System. *Science, 283*(5400), 341-345. https://doi.org/10.1126/science.283.5400.341.

Thiemens, M. H. (2006). History and Applications of Mass-Independent Isotope Effects. *Annual Review Of Earth And Planetary Sciences*, *34*(1), 217-262.

Uribe, J., Muñoz, J. F., Gironás, J., Oyarzún, R., Aguirre, E., & Aravena, R. (2015). Assessing groundwater recharge in an Andean closed basin using isotopic characterization and a rainfall-runoff model: Salar del Huasco basin, Chile. *Hydrogeology Journal*, *23*(7), 1535-1551.

Vásquez, P., & Sepúlveda, F. (2013). *Cartas Iquique y Pozo Almonte, Región de Tarapacá* [Geological map, 1:100,000]. Servicio Nacional de Geología y Minería (SERNAGEOMIN). Carta Geológica de Chile, Serie Geología Básica, 162-163.

Vásquez, P., Sepúlveda, F. A., Quezada, A., Aguilef, S., Franco, C., & Blanco, N. (2018). *Cartas Guanillos del Norte y Salar de Llamara, Regiones de Tarapacá y Antofagasta* [Geological map, 1:100,000]. Servicio Nacional de Geología y Minería (SERNAGEOMIN). Carta Geológica de Chile, Serie Geología Básica, 195-196.

Vicars, W. C., & Savarino, J. (2014). Quantitative constraints on the 17O-excess (Δ17O) signature of surface ozone: Ambient measurements from 50°N to 50°S using the nitrite-coated filter technique. *Geochimica Et Cosmochimica Acta, 135*, 270-287.

Vicencio, J. V., Böhm, C., Schween, J. H., Löhnert, U., & Crewell, S. (2024). The Overlooked Role of Moist Northerlies as a Source of Summer Rainfall in the Hyperarid Atacama Desert. *Journal Of Geophysical Research Atmospheres*, *129*(21).

Voigt, C., Klipsch, S., Herwartz, D., Chong, G., & Staubwasser, M. (2020). The spatial distribution of soluble salts in the surface soil of the Atacama Desert and their relationship to hyperaridity. *Global and Planetary Change, 184*, 103077.

Voigt, C., Herwartz, D., Dorador, C., & Staubwasser, M. (2021). Triple oxygen isotope systematics of evaporation and mixing processes in a dynamic desert lake system. *Hydrology And Earth System Sciences, 25*(3), 1211-1228

Wankel, S.D., Bradley, A.S., Eldridge, D.L., Johnston, D.T. (2014). Determination and application of the equilibrium oxygen isotope effect between water and sulfite. *Geochim. Cosmochim*. Acta 125, 694–711.

White, W. M. (2015). *Isotope Geochemistry*. John Wiley & Sons.

Appendix

A.1 Supplementary material to Chapter 5

Table A1.1: Samples description and location.

sample name	*type of deposit*	*type of sample*	*comment*	*geological site*	*latitude*	*longitude*	*elevation [m asl]*
01B-190122	Vein in rocks (type-iic)	caliche blanco	massive vein	Cerro Birrete	22,93	69,71	1563
06-190122	Neptunic dyke (type-iib)	caliche negro		Cerro Birrete	22,89	69,73	1506
21-240122	Neptunic dyke (type-iib)	caliche negro		Cerro Birrete	22,99	69,72	1573
22-240122	Vein in rocks (type-iic)	salt crust		Cerro Birrete	22,99	69,72	1573
25-240122	Vein in rocks (type-iic)	salt crust		Cerro Birrete	22,99	69,72	1573
28-240122	Neptunic dyke (type-iib)	caliche negro		Cerro Birrete	23,01	69,73	1523
39-250122	Sedimentary (type-i)	caliche negro		Cerro Birrete	22,91	69,77	1500
40C-250122	Sedimentary (type-i)	thenardite		Cerro Birrete	22,91	69,77	1498
40D-250122	Sedimentary (type-i)	caliche negro		Cerro Birrete	22,91	69,77	1498
40E-250122	Sedimentary (type-i)	caliche negro		Cerro Birrete	22,91	69,77	1498
4B-210821	Vein in rocks (type-iic)	caliche blanco	fibrous vein	Oficina Domeyko	23,81	69,35	1749
4F-180123	Vein in sedimentary deposit (type-iia)	caliche blanco		Aguas Blancas	24,16	69,89	1101
54-260122	Vein in rocks (type-iic)	black mineral	massive	Cerro Birrete	23,04	69,67	1534
ATA17-034d	Salar (type-iii)	salar surface		Salar de Llamara	21,06	69,65	925
ATA18-016b	Vein in rocks (type-iic)	caliche blanco	massive vein	Oficina California	19,68	70,06	1172
ATA18-016d	Vein in rocks (type-iic)	caliche blanco	massive vein	Oficina California	19,68	70,06	1172
ATA18-017	Sedimentary (type-i)	caliche negro		Oficina California	19,68	70,06	1169
ATA18-018	Vein in rocks (type-iic)	caliche azul	massive vein	Oficina Santa Rita	19,70	69,97	1144
ATA18-018x	Vein in rocks (type-iic)	caliche azul	massive vein	Oficina Santa Rita	19,70	69,97	1144
ATA18-019	Vein in rocks (type-iic)	caliche blanco	massive vein	Oficina Santa Rita	19,71	69,97	1145
ATA18-027a	Vein in rocks (type-iic)	caliche blanco	massive vein	Oficina Germania	19,89	69,79	1157
ATA18-027b	Vein in rocks (type-iic)	caliche blanco	massive vein	Oficina Germania	19,89	69,79	1157
ATA18-027c	Vein in rocks (type-iic)	caliche amarillo	massive vein	Oficina Germania	19,89	69,79	1157

ATA18-027d	Vein in rocks (type-iic)	caliche blanco	massive vein	Oficina Germania	19,89	69,79	1157
ATA22-007	Vein in rocks (type-iic)	caliche blanco	massive vein	Cu Mine	21,10	69,89	1102
ATA22-020A	Vein in rocks (type-iic)	caliche blanco	fibrous vein	Oficina Domeyko	23,81	69,35	1756
ATA22-020D/R	Vein in rocks (type-iic)	rhyolite		Oficina Domeyko	23,81	69,35	1756
ATA22-020D/V	Vein in rocks (type-iic)	caliche blanco	fibrous vein	Oficina Domeyko	23,81	69,35	1756
ATA22-020G	Sedimentary (type-i)	thenardite		Oficina Domeyko	23,81	69,35	1756
ATA22-022A	Vein in rocks (type-iic)	caliche blanco	fibrous vein	Oficina Domeyko	23,79	69,40	1626
ATA22-022B	Vein in rocks (type-iic)	caliche amarillo	massive vein	Oficina Domeyko	23,79	69,40	1626
ATA22-024D3	Sedimentary (type-i)	caliche negro		Aguas Blancas	24,16	69,89	1052
ATA22-024E	Vein in sedimentary deposit (type-iia)	caliche amarillo	massive vein	Aguas Blancas	24,16	69,89	1052
ATA22-024F	Sedimentary (type-i)	caliche negro		Aguas Blancas	24,16	69,89	1052
ATA22-024G1	Vein in sedimentary deposit (type-iia)	caliche amarillo	massive vein	Aguas Blancas	24,16	69,89	1052
ATA22-024H	Sedimentary (type-i)	caliche negro		Aguas Blancas	24,16	69,89	1052
ATA22-025B	Vein in rocks (type-iic)	caliche blanco	massive vein	Aguas Blancas	24,17	69,91	1137
ATA22-026A1	Vein in sedimentary deposit (type-iia)	caliche blanco	massive vein	Aguas Blancas	24,15	69,91	1115
ATA22-026A2	Vein in sedimentary deposit (type-iia)	caliche blanco	fibrous vein	Aguas Blancas	24,15	69,91	1115
ATA22-026B	Sedimentary (type-i)	caliche negro		Aguas Blancas	24,15	69,91	1115
ATA22-026C	Vein in sedimentary deposit (type-iia)	caliche amarillo	massive vein	Aguas Blancas	24,15	69,91	1115
ATA22-066A	Vein in rocks (type-iic)	caliche blanco	fibrous vein	Oficina Domeyko	23,81	69,35	1749
ATA22-066H	Vein in rocks (type-iic)	caliche blanco	fibrous vein	Oficina Domeyko	23,81	69,35	1749
ATA22-067	Vein in rocks (type-iic)	caliche blanco	massive vein	Oficina Domeyko	23,81	69,35	1741
ATA22-074B	Vein in rocks (type-iic)	caliche blanco		Oficina Domeyko	23,79	69,37	1693
ATA22-074D	Sedimentary (type-i)	thenardite		Oficina Domeyko	23,79	69,37	1693
ATA22-075	Vein in rocks (type-iic)	caliche blanco	fibrous vein	Oficina Domeyko	23,79	69,37	1707
ATA22-077C	Vein in rocks (type-iic)	halite	stalactite	Oficina Domeyko	23,79	69,37	1769
ATA22-080B	Vein in rocks (type-iic)	halite	massive vein	Oficina Domeyko	23,79	69,36	1745
ATA22-080C	Vein in rocks (type-iic)	halite	stalactite	Oficina Domeyko	23,79	69,36	1745
ATA22-082A	Vein in rocks (type-iic)	caliche blanco	massive vein	Oficina Domeyko	23,80	69,39	1630
ATA22-083A	Vein in rocks (type-iic)	caliche blanco	massive vein	Oficina Domeyko	23,80	69,38	1643
ATA22-085E	Sedimentary (type-i)	caliche negro		Oficina Domeyko	23,80	69,38	1630
ATA22-090A	Vein in sedimentary deposit (type-iia)	caliche amarillo	massive vein	Aguas Blancas	24,16	69,89	1073
ATA23-002a	Vein in sedimentary deposit (type-iia)	caliche blanco	massive vein	Aguas Blancas	24,16	69,89	1071
ATA23-002c	Vein in sedimentary deposit (type-iia)	caliche blanco	fibrous vein	Aguas Blancas	24,16	69,89	1071
ATA23-002d	Vein in sedimentary deposit (type-iia)	caliche amarillo	massive vein	Aguas Blancas	24,16	69,89	1071

ATA23-002e	Vein in sedimentary deposit (type-iia)	caliche amarillo	massive vein	Aguas Blancas	24,16	69,89	1071
ATA23-002f/2	Vein in sedimentary deposit (type-iia)	caliche blanco	massive vein	Aguas Blancas	24,15	69,91	1071
ATA23-003/1d	Sedimentary (type-i)	thenardite		Aguas Blancas	24,15	69,91	1134
ATA23-003/1g	Sedimentary (type-i)	caliche negro		Aguas Blancas	24,15	69,91	1134
ATA23-003/2h	Vein in sedimentary deposit (type-iia)	caliche blanco	massive vein	Aguas Blancas	24,15	69,91	1126
ATA23-003/2i-b	Sedimentary (type-i)	caliche negro		Aguas Blancas	24,15	69,91	1126
ATA23-003/2i-y	Vein in sedimentary deposit (type-iia)	caliche amarillo	massive vein	Aguas Blancas	24,16	69,92	1126
ATA23-007/1c	Sedimentary (type-i)	thenardite		Aguas Blancas	24,07	69,89	990
ATA23-008c	Sedimentary (type-i)	thenardite		Aguas Blancas	24,08	69,87	986
ATA23-008h	Sedimentary (type-i)	thenardite		Aguas Blancas	24,08	69,87	986
ATA23-009c	Sedimentary (type-i)	thenardite		Aguas Blancas	24,07	69,89	987
ATA23-010c	Sedimentary (type-i)	thenardite		Aguas Blancas	24,10	69,90	1028
ATA23-013	Sedimentary (type-i)	thenardite		Aguas Blancas	24,11	69,90	984
ATA23-018	Sedimentary (type-i)	thenardite		Aguas Blancas	24,41	69,60	1758
ATA23-024c	Sedimentary (type-i)	thenardite		Aguas Blancas	24,59	69,59	1761
ATA23-025a	Sedimentary (type-i)	thenardite		Aguas Blancas	24,59	69,59	1782
ATA23-026	Sedimentary (type-i)	thenardite		Aguas Blancas	24,59	69,59	1786
ATA23-045	Sedimentary (type-i)	thenardite		Oficina Domeyko	23,79	69,38	1673
ATA23-046b	Sedimentary (type-i)	thenardite		Oficina Domeyko	23,77	69,40	1749
ATA23-048b	Sedimentary (type-i)	caliche negro		Oficina Domeyko	23,77	69,35	1743
ATA23-050e	Sedimentary (type-i)	caliche negro		Oficina Domeyko	23,82	69,29	2001
ATA23-052	Sedimentary (type-i)	soluble salt		Oficina Domeyko	23,82	69,29	1983
ATA23-100a2	Vein in rocks (type-iic)	caliche blanco	massive vein	Oficina Santa Rita	19,71	69,97	1152
ATA23-100b2	Vein in rocks (type-iic)	caliche amarillo	massive vein	Oficina Santa Rita	19,71	69,97	1152
ATA23-100d	Neptunic dyke (type-iib)	caliche negro		Oficina Santa Rita	19,71	69,97	1152
ATA23-101a	Vein in rocks (type-iic)	calcihe blanco	fibrous vein	Oficina Santa Rita	19,71	69,97	1159
ATA23-101c	Vein in rocks (type-iic)	caliche azul	massive vein	Oficina Santa Rita	19,71	69,97	1159
ATA23-101d	Neptunic dyke (type-iib)	caliche negro		Oficina Santa Rita	19,71	69,97	1159
ATA23-102a	Vein in rocks (type-iic)	caliche blanco	massive vein	Oficina Santa Rita	19,71	69,97	1118
ATA23-102b	Vein in rocks (type-iic)	caliche azul	massive vein	Oficina Santa Rita	19,71	69,97	1118
ATA23-103	Sedimentary (type-i)	caliche negro		Oficina San Francisco	19,70	69,93	1134
ATA23-104b	Sedimentary (type-i)	powdery nitrate		Oficina Asturias	19,82	69,87	1153
ATA23-109b	Vein in rocks (type-iic)	caliche blanco	massive vein	Oficina Germania	19,89	69,79	1173
ATA23-109c	Neptunic dyke (type-iib)	caliche negro		Oficina Germania	19,89	69,79	1173

Appendix

ATA23-110a	Salar (type-iii)	caliche negro		Salar Dolores	19,68	70,02	1121
ATA23-111a	Neptunic dyke (type-iib)	caliche negro		Oficina California	19,68	70,06	1168
ATA23-111b	Vein in rocks (type-iic)	caliche blanco		Oficina California	19,68	70,06	1168
ATA23-111c/1	Vein in rocks (type-iic)	caliche blanco		Oficina California	19,68	70,06	1168
ATA23-111c/2	Vein in rocks (type-iic)	caliche blanco		Oficina California	19,68	70,06	1168
ATA23-111d	Neptunic dyke (type-iib)	caliche negro		Oficina California	19,68	70,06	1168
ATA23-112a	Sedimentary (type-i)	thenardite		Oficina California	19,68	70,06	1160
ATA23-112c	Sedimentary (type-i)	caliche negro		Oficina California	19,68	70,06	1160
ATA23-OD	Vein in rocks (type-iic)	caliche blanco	fibrous vein	Oficina Domeyko	23,81	69,35	1749
ATA25-031A	Vein in rocks (type-iic)	exsolution		Oficina Domeyko	23,81	69,35	1757
MP19-D	Vein in sedimentary deposit (type-iia)	caliche blanco	massive vein	Aguas Blancas	24,13	69,91	1038
MPAD-2	Vein in sedimentary deposit (type-iia)	caliche blanco	stalactite	Aguas Blancas	24,16	69,89	1052
Pique-118D	Vein in sedimentary deposit (type-iia)	caliche blanco	massive vein	Aguas Blancas	24,13	69,92	1042
Pique-118D-2	Vein in sedimentary deposit (type-iia)	caliche blanco	stalactite	Aguas Blancas	24,13	69,92	1042

A.2 Supplementary material to Chapter 6

A2.1 Internal Standards from the University of Cologne (UoC-Nit-3, 4, and 5)

The generation of UoC-Nit-3 was made for Swea Klipsch before the start of this thesis, and the protocol is described as follows:

Generation of $NaNO_3$ with ^{17}O-anomalie:

- 10ml 14M HNO3 (65%) in Nalgene bottle

UoC-Nit-3 add 90ml H2O and 0.35ml solution ε*

- Leave for 7 days at 80°C in the oven to equilibrate
- Titrate the acid (beaker cooled with ice bath) with 10M NaOH (burette) until neutral pH ~7. HNO3 + NaOH NaNO3 + H2O
- Evaporate H2O to get NaNO3 standard

* Solution ε = 34.5ml 17O water I + 103.5ml VE water

17O water I = 1ml 70% 17O water + 50ml VE water

solution ε ≈ 0.6765ml 70% 17O water + 137.3235ml VE water

For the UoC-Nit-4 and UoC-Nit-5, 2 samples from the field campaign were used:

ATA22-020A for UoC-Nit-4, and ATA23-002d for the UoC-Nit-5. They were chosen because ATA22-020A represents the lower value for $\delta^{18}O$, and ATA23-002d the highest value; therefore, they can be used as internal standards for all the rest of the samples for the normalization procedure of $\delta^{18}O$.

Table A2.1: Analytical precision and accuracy for nitrate (NO_x) quantification by spectrophotometry. Cal 1 to 5 are the calibration range, and RM refers to the reference material (Anions-Whole Volume, Sigma-Aldrich).

ID	Target concentration [µM]	Mean measured value [µM]	Standard deviation [µM]	RSD %	Recovery %
Cal 1	5	4.66	0.35	7.48	93.22
Cal 2	10	9.76	0.40	4.09	97.65
Cal 3	25	25.30	0.71	2.81	101.19
Cal 4	50	50.61	1.00	1.98	101.23
Cal 5	100	99.66	1.54	1.54	99.66
RM	59.21	67.19	5.13	7.64	113.47

Table A2.2: Target concentration from calibration range (K01 – K04) and certified reference materials (CRM: ATA_INT-1, I-1, and Li-1, BATTLE_2, BATTLE_19, SPS-SW, WP-500) for ICP-OES analysis. K0, the 0 [mg/l] value for each element, is not shown in the table. ATA_INT-1, I-1, and Li-1 are internal CRM from the University of Cologne. BATTLE_2 and BATTLE_19 are from Environment and Climate Change Canada, SPS-SW2 is from Spectrapure Standards, and WP-500 is from Sigma-Aldrich.

	I [mg/l]	*Sr* [mg/l]	*Br* [mg/l]	*As* [mg/l]	*Cr* [mg/l]	*Ca* [mg/l]	*K* [mg/l]	*Cl* [mg/l]	*S* [mg/l]	*Mg* [mg/l]	*Na* [mg/l]	*B* [mg/l]	*Li* [mg/l]
ATA_INT-1-						13.63	4.2	120	52.89	5.45	75.85		
BATLLE_2-						25	5.52	42.5	28.22	21.7	163	0.263	
Bt-19-						30.6	4.23	16.8	84.4	17.1	70.7		
I-0.1-	1												
K01	0.1	0.1	0.1	0.1	0.1	4	0.1	4	4	0.1	2.5	0.1	0.1
K02	0.2	0.2	0.2	0.2	0.2	8	0.2	8	8	0.2	5	0.2	0.2
K03	0.4	0.4	0.4	0.4	0.4	12	0.4	12	12	0.4	7.5	0.4	0.4
K04	1.6	1.6	1.6	1.6	1.6	16	1.6	16	16	1.6	10	1.6	1.6
Li-0.1-													1
SPS-W2-		0.25		0.05	0.01	10	1		10	2	10	0.25	
WP-500-			3.25					123	18.54				

Table A2.3: Analytical precision and accuracy for element concentration quantified by ICP-OES. K01 to K04 are the calibration range.

Standards	*Statistics*	*I* [mg/l]	*Sr* [mg/l]	*Br* [mg/l]	*As* [mg/l]	*Cr* [mg/l]	*Ca* [mg/l]	*K* [mg/l]	*Cl* [mg/l]	*S* [mg/l]	*Mg* [mg/l]	*Na* [mg/l]	*B* [mg/l]	*Li* [mg/l]
ATA_INT-1	MEAN						12.48	2.74	94.03	53.73	5.15	68.63		
BATLLE_2	MEAN						23.50	3.92	43.62	49.43	22.27	151.37	0.25	
BATTLE-19	MEAN						31.17	3.07	-1.87	29.11	18.49	67.68		
I-1	MEAN	0.97												
K01	MEAN	0.07	0.09	0.46	0.08	0.08	3.49	0.09	3.46	3.34	0.08	2.08	0.08	0.08
K02	MEAN	0.16	0.16	0.79	0.17	0.16	6.60	0.16	6.56	8.14	0.17	4.05	0.16	0.16
K03	MEAN	0.46	0.40	1.97	0.41	0.41	11.97	0.39	12.03	12.07	0.41	7.62	0.40	0.41
K04	MEAN	1.59	1.60	8.01	1.60	1.60	16.00	1.60	16.05	15.87	1.60	9.87	1.60	1.60
Li-1	MEAN													0.98
SPS-SW2	MEAN		0.24	0.10	0.05	0.01	9.90	0.72		10.70	2.00	9.49	0.21	
WP-500	MEAN			3.69					106.13	20.91				
ATA_INT-1	SD						0.40	0.19	43.78	0.97	0.14	2.18		
BATLLE_2	SD						0.71	0.24	5.43	2.03	0.93	5.93	0.15	
BATTLE-19	SD						0.36	0.05	0.08	0.20	0.17	0.47		
I-1	SD	0.08												
K02	SD	0.05	0.04	0.18	0.04	0.04	1.73	0.03	1.66	1.69	0.04	0.99	0.04	0.04
K03	SD	0.08	0.08	0.34	0.08	0.08	3.25	0.07	3.13	0.06	0.08	1.96	0.08	0.08
K04	SD	0.09	0.01	0.04	0.01	0.00	0.20	0.00	0.28	0.20	0.01	0.08	0.03	0.01
K05	SD	0.02	0.00	0.01	0.00	0.00	0.16	0.00	0.21	0.15	0.00	5.48	0.00	0.00
Li-1	SD													0.05
SPS-SW2	SD		0.01	0.03	0.00	0.00	0.22	0.01		0.40	0.06	0.25	0.06	
WP-500	SD			0.17					51.76	0.76				
	REPRODUCIBILITY	0.06	0.03	0.13	0.03	0.03	0.88	0.07	13.29	0.72	0.18	2.17	0.06	0.04

A.3 Supplementary material to Chapter 7

Table A3.1: Chemical composition data of all samples. Total SO_4 corresponds to samples leached with sodium carbonate, and SO_4 leached with water.

Sample name	*NO3 [mg/g]*	*total SO4 [mg/g]*	*SO4 [mg/g]*	*Na [mg/g]*	*Cl [mg/g]*	*Ca [mg/g]*	*K [mg/g]*	*Mg [mg/g]*	*I [ppm]*	*Sr [ppm]*	*Br [ppm]*	*As [ppm]*	*Cr [ppm]*	*B [ppm]*	*Li [ppm]*
01B-190122	109,43	125,57	85,17	48,74	30,14	39,31	2,63	0,34	1259,14	923,63	<	<	4,86	476,80	<
06-190122	149,18	63,15	64,29	71,25	44,32	11,47	6,50	9,64	1588,08	104,29	<	<	1,89	1482,41	10,46
21-240122	131,15	201,96	199,98	184,09	118,03	18,37	10,54	2,66	192,74	64,44	<	<	<	571,33	<
22-240122	274,64		9,97	236,47	206,89	5,38	0,41	0,05	1562,39	31,17	<	<	<	94,17	<
25-240122	395,52		9,05	237,89	159,96	6,52	1,75	0,09	2312,13	38,59	<	<	<	106,46	<
28-240122	127,03	51,26	56,89	64,93	39,04	19,79	1,55	0,38	<	74,91	<	<	<	168,45	<
39-250122	252,16	23,49	21,35	122,97	75,73	4,53	5,52	0,29	1478,11	88,42	<	<	<	613,39	<
40C-250122	21,02	497,19	544,21	227,27	5,54	18,99	0,66	0,85	13,67	530,62	<	39,54	<	57,16	<
40D-250122	196,74	124,89	122,54	131,05	121,08	18,69	13,28	13,59	289,22	195,38	<	16,05	2,42	470,65	29,92
40E-250122	148,65	347,47	325,66	171,28	11,80	21,10	3,64	2,12		67,33	<	<	<	4921,36	7,38
4B-210821	676,09	4,09	3,83	239,96	50,92	0,42	<	<	63,68	<	<	<	<	<	<
4F-180123	675,32	5,01	60,32		12,23		1,27	1,99	577,40	98,92	<	<	<	300,60	<
54-260122	45,90		19,33	29,20	21,33	6,53	2,11	0,26	191,46	124,21	<	<	4,01	1044,76	<
ATA17-034d	56,22		23,07	157,16	265,09	10,94	2,53	0,45	83,83	54,09	<	<	<	50,26	0,40
ATA18-016b	589,91	4,08	2,98	260,37	163,48	0,52	2,07	0,01	253,93	<	<	<	<	8,76	<
ATA18-016d	530,93	4,74	4,22	259,81	213,54	1,94	0,13	0,03	183,58	71,23	<	<	<	35,02	<
ATA18-017	39,89		196,36	73,57	101,44	26,20	16,50	23,67	1292,04	172,86	<	<	<	144,32	7,33
ATA18-018	598,75	20,73	16,27	205,06	122,26	0,09	48,59	0,79	733,10	<	<	<	<	184,41	0,61
ATA18-018x	565,29	24,36	18,54	213,78	143,59	0,10	35,35	0,05	541,69	2,30	145,62	<	<	499,84	<
ATA18-019	500,13	8,88	7,19	276,45	226,67	0,87	0,10		<	<	<	<	<	0,99	<
ATA18-027a	428,49	72,85	66,39	262,38	219,36	<	0,58	9,08	61,76	5,67	<	<	<	1,16	<
ATA18-027b	279,60	124,03	124,84	257,02	252,75	<	2,86	14,00	93,03	<	<	<	<	182,40	4,70
ATA18-027c	249,30	105,56	103,10	268,81	301,00	<	2,26	13,34	1282,15	<	<	<	25,12	214,93	<
ATA18-027d	354,13	68,33	70,77	282,53	272,87	<	0,76	3,69	339,82	0,57	<	<	<	43,10	<
ATA22-007	214,11		22,87	242,86	332,01	8,77	1,34	1,73	<	7,83	<	851,24	<	21,32	<
ATA22-020A	187,71	34,36	32,58	275,90	347,10	<	<	0,04	<	0,67	113,07	<	<	<	<

Appendix

ATA22-020D/R	15,78	10,12	9,79	9,16	<	0,11	0,20	1,34	582,47	0,42	<	<	1,99	138,77	<
ATA22-020D/V	174,91	73,30	0,00			0,54	<	0,04	111,23	1,02	<	<	<	<	<
ATA22-020G	0,74	545,76	605,02	251,93	1,95	9,86	1,64	0,51	<	439,56	<	21,01	<	7,07	<
ATA22-022A	435,83	0,82													
ATA22-022B	400,63	126,91	148,99	224,19	78,94	1,26	0,08	6,15	3256,98	18,23	<	<	4,55	<	<
ATA22-024D3	108,00	80,14	83,98	63,17	62,05	14,50	11,61	6,42	1073,26	206,75	<	<	4,03	97,12	<
ATA22-024E	384,82	55,93	62,07	239,84	144,17	0,50	2,68	5,03	2244,72	10,89	99,68	<	22,91	1501,36	<
ATA22-024F	12,24	44,05	46,79	244,08	359,66	6,67	0,35	0,87	78,17	63,46	<	<	<	100,95	<
ATA22-024G1	164,49	44,37	49,47	282,87	322,99	0,55	0,49	2,15	587,67	11,76	<	<	4,02	332,34	<
ATA22-024H	204,39	128,95	114,93	130,85	70,20	26,24	3,23	1,37	328,62	159,76	<	<	18,95	185,03	<
ATA22-025B	251,10	14,68	16,12	278,06	289,57	1,22	0,13	0,03	2816,02	11,74	<	<	<	72,05	<
ATA22-026A1	393,04	21,93	21,98	257,82	191,80	1,45	0,08	0,00	892,16	24,82	<	<	<	36,86	<
ATA22-026A2	100,99	9,51	9,33	296,67	376,64	1,52	0,08	0,01	<	5,61	<	<	<	<	<
ATA22-026B	23,54	267,42	265,29	94,06	38,39	34,71	3,49	7,61	907,02	102,00	<	<	<	299,70	<
ATA22-026C	517,01	15,26	14,29	237,64	116,60	1,01	4,72	0,55	1914,29	28,37	<	<	11,74	419,43	<
ATA22-066A	217,16	50,70	62,73	264,91	261,70	1,22	<	6,18	<	6,99	123,46	<	<	<	<
ATA22-066H	102,16	46,94	47,23	292,33	346,47	0,03	<	0,00	<	<	97,39	<	<	<	<
ATA22-067	159,78	212,54	234,83	261,96	160,75	2,35	<	0,38	295,77	9,98	<	<	<	43,93	<
ATA22-074B	168,27	265,96	257,62	255,45	131,97	0,11	0,06	0,74	167,04	<	<	<	<	<	<
ATA22-074D	5,16	566,93	618,91	250,29	3,58	5,94	0,33	0,64	<	215,55	<	<	<	20,82	<
ATA22-075	124,55	114,67	94,13	279,32	282,31	<	0,10	1,04	<	<	127,35	<	<	<	<
ATA22-077C	125,02	140,28	137,30	273,51	304,95	1,44	0,11	0,25	<	15,92	<	<	<	55,08	<
ATA22-080B	215,97	161,07	149,48	255,51	178,39	0,13	1,75	1,81	601,08	1,99	<	<	<	276,53	13,54
ATA22-080C	130,46	132,00	128,58	272,83	304,94	0,16	0,88	1,66	525,22	0,55	<	<	<	443,33	0,72
ATA22-082A	236,42	41,42	42,73	264,31	319,62	4,88	0,54	1,73	<	20,25	<	<	<	<	<
ATA22-083A	229,11	284,09	293,36	152,32	88,30	1,57	1,93	51,94	904,42	14,17	<	<	<	206,90	19,40
ATA22-085E	31,35		218,18	61,84	31,16	55,17	3,10	30,02	57,54	419,68	<	<	<	517,82	<
ATA22-090A	506,29	41,36	38,83	231,83	107,08	0,39	6,44	2,66	500,93	11,36	<	<	29,74	1045,02	<
ATA23-002a	113,69	45,03	44,10	405,22		0,52	0,66	1,01	572,52	14,60	<	<	<	223,65	<
ATA23-002c	454,69	42,26	43,35	271,74	180,24	1,11	4,32	6,81	1126,03	10,75	<	<	1,34	186,95	<
ATA23-002d	469,39	49,99	50,62	255,01	165,66	0,14	5,93	6,90	899,41	1,42	<	<	7,92	754,77	<
ATA23-002e	394,97	53,79	58,84	255,18	208,80	0,09	2,37	6,29	1732,15	9,00	<	<	33,17	2068,66	<
ATA23-002f/2	145,20	198,78	224,00	86,61	61,39	74,15	4,07	6,57	249,27	476,77	<	<	<	919,52	<
ATA23-003/1d	0,60	586,72	609,71	253,19	1,34	8,77	0,18	4,45	<	214,00	<	<	<	14,43	<

ATA23-003/1g	66,72	340,46	381,34	106,07	25,22	61,58	19,26	9,18	537,94	144,21	<	<	18,14	719,64	<
ATA23-003/2h	265,96	15,11	13,36	284,12	362,99	1,99	0,15	0,00	189,26	14,46	<	<	<	<	<
ATA23-003/2i-b	517,01	13,71	16,89	222,85	156,64	0,80	7,86	0,76	2342,64	28,03	<	<	35,17	602,32	<
ATA23-003/2i-y	521,08	17,70	13,17	235,95	147,77	3,84	1,34	0,19	375,78	29,42	<	<	<	1715,84	<
ATA23-048b	159,45		0,00		0,43		1,85	0,04	299,51	549,63	<	<	<	72,28	<
ATA23-050e	292,73														
ATA23-052	483,08	5,85	6,14			3,94	15,52	0,05	16673,54	156,59	<	<	114,70	<	<
ATA23-100a2	454,86	62,34	76,21			28,62	13,46	0,17	198,02	92,16	<	<	<	<	0,94
ATA23-100b2	533,20	11,98	11,77			0,66		0,90	5873,21	<	<	<	29,19	<	29,88
ATA23-100d	57,11	127,16	124,71	60,65		21,37	11,20	6,86	332,57	139,97	<	<	<	<	7,22
ATA23-101a	1,32	11,60													
ATA23-101c	545,22	10,78	10,44			0,37	51,73	0,05	1773,81	5,75	<	<	1,54	<	<
ATA23-101d	25,73	132,53	127,36			17,68	2,92	0,37	196,41	77,93	<	<	<	<	11,16
ATA23-102a	491,37	9,57	8,71		11,44	0,71	3,24	0,00	820,94	34,90	<	<	<	<	<
ATA23-102b	606,86	-0,11	0,92			<		0,00	<	<	<	<	<	<	<
ATA23-103	21,26	42,93	43,84	61,88		10,89	2,87	0,09	134,98	59,66	<	<	<	<	4,87
ATA23-104b	409,42	27,91	27,82		15,93	15,20		0,03	<	146,16	<	<	<	75,24	<
ATA23-109b	304,89	95,78	90,11		18,14	<		12,44	217,24	2,92	<	<	4,46	<	<
ATA23-109c	250,37	70,82	0,00		10,03	5,62			405,95	26,02	<	<	<	228,71	31,89
ATA23-110a	5,11	216,71	215,02		25,66	41,71	17,68	7,01	<	702,39	<	17,46	<	<	476,69
ATA23-111a	66,77	85,06	83,44			14,03		11,54	336,31	49,23	<	<	<	<	6,99
ATA23-111b	476,31	5,87	5,88		13,77	2,21		0,02	86,85	80,09	<	<	<	<	<
ATA23-111c/1	478,07	13,08	10,87		12,96	2,00		0,01	156,67	19,26	<	<	<	<	<
ATA23-111c/2	290,99	70,29	66,41			15,20	1,43	0,57	983,55	93,62	<	<	0,57	<	<
ATA23-111d	195,06	178,36	0,00		5,22			0,69	622,51	74,21	<	<	6,53	926,23	<
ATA23-112a															
ATA23-112c	126,46	140,60	4,56		2,49	1,23	0,15	0,07	5,67	13,19	<	<	<	13,42	<
ATA23-OD	321,43	55,99	61,81	372,04		1,82	0,11	6,49	398,06	30,46	<	<	<	59,01	<
MP19-D	500,34	8,65	0,00		15,37					216,01	<	<	5,36	1053,12	10,26
MPAD-2	500,72	9,96	10,40		18,80	0,59	1,59	0,40	2120,06	39,52	<	<	7,12	761,76	<
Pique-118D	510,75	9,65													
Pique-118D-2	514,33	15,25													

Table A3.2: Isotope data of all samples. Oxygen isotope data are reported relative to the VSMOW, sulfur isotopes relative to the VCDT, and nitrogen isotopes relative to AIR.

Sample name	*$\Delta^{17}O_{NO3}$ (‰)*	*1σ SD (‰)*	*$\delta^{18}O_{NO3}$ (‰)*	*1σSD (‰)*	*$\delta^{15}N_{NO3}$ (‰)*	*1σSD (‰)*	*$\delta^{34}S_{SO4}$ (‰)*	*1σSD (‰)*
01B-190122	20,09	0,17			-1,59	0,15	2,90	0,10
06-190122	18,96	0,21			-0,91	0,15		
21-240122	19,39	0,10	52,61	1,83	0,03	0,15	4,00	0,10
22-240122					-1,74	0,15		
25-240122					-1,58	0,15		
28-240122	18,66	0,08			2,55	0,15		
39-250122	20,16	0,08	58,98	0,29	-0,71	0,15		
40C-250122							5,50	0,10
40D-250122	18,92	0,41	48,80	0,73	0,77	0,15	5,60	0,10
40E-250122	18,15	0,75			-1,18	0,15		
4B-210821	18,85	0,16	55,45	0,81	0,16	0,15		
4F-180123	21,68	0,16	63,77	0,67	0,69	0,15		
54-260122					-3,08	0,15		
ATA17-034d	17,50	0,46			-1,32	0,15		
ATA18-016b	18,02	0,10	51,33	0,05	-3,95	0,15		
ATA18-016d	16,85	0,17	50,00	0,36	-4,27	0,15		
ATA18-017	16,40	0,48			-4,85	0,15		
ATA18-018	14,77	0,37	46,03	1,74	-5,44	0,15		
ATA18-018x	14,79	0,31	43,09	0,26	-4,89	0,15		
ATA18-019	14,01	0,36	44,79	0,45	-3,58	0,15		
ATA18-027a	16,75	0,37	50,41	0,85	-0,65	0,15		
ATA18-027b	16,29	0,26	46,80	0,32	-1,66	0,15	2,36	0,10
ATA18-027c	16,26	0,51	48,63	0,29	-2,21	0,15		
ATA18-027d	17,20	0,28	51,69	0,20	-1,80	0,15		
ATA22-007	19,18	0,15						
ATA22-020A	12,92	0,17	43,02	0,03	0,62	0,15	-0,80	0,10
ATA22-020D/R							-0,60	0,10
ATA22-020D/V	13,51	0,10	43,03	0,35	0,32	0,15		
ATA22-020G							0,80	0,10
ATA22-022A	17,91	0,14	54,47	0,31	0,67	0,15		
ATA22-022B	18,64	0,24	55,02	0,16	0,58	0,15	2,80	0,10
ATA22-024D3	20,31	0,21	56,76	0,10	-2,19	0,15		
ATA22-024E	20,23	0,29	62,63	0,48	1,02	0,15	2,50	0,10
ATA22-024F					-0,04	0,15		
ATA22-024G1	20,98	0,08	64,35	0,89	0,89	0,15	0,00	0,10
ATA22-024H	20,51	0,11	60,50	0,45	0,25	0,15	4,30	0,10
ATA22-025B	20,99	0,09	61,50	0,20	-0,42	0,15	2,00	0,10
ATA22-026A1	21,17	0,14			1,55	0,15	3,70	0,10
ATA22-026A2	21,20	0,07			2,44	0,15		
ATA22-026B	20,07	0,44			-1,52	0,15		

ATA22-026C	21,25	0,24	59,62	0,53	-0,70	0,15	3,30	0,10
ATA22-066A	13,03	0,20			0,19	0,15	-0,40	0,10
ATA22-066H							0,70	0,10
ATA22-067							1,00	0,10
ATA22-074B	15,75	0,21	46,24	0,57	0,40	0,15	2,30	0,10
ATA22-074D							3,00	0,10
ATA22-075	14,90	0,16			-0,96	0,15	-0,30	0,10
ATA22-077C	18,51	0,08	53,62	2,02	0,11	0,15	2,60	0,10
ATA22-080B	15,53	0,32	46,73	0,17	0,19	0,15		
ATA22-080C	15,20	0,10	47,68	0,38	0,38	0,15		
ATA22-082A	17,26	0,10			1,62	0,15		
ATA22-083A	18,46	0,37			0,03	0,15		
ATA22-085E	18,85	0,60	49,90	2,37	-0,94	0,15		
ATA22-090A	20,90	0,11			0,07	0,15	3,20	0,10
ATA23-002a	20,99	0,18	61,98	0,21	0,76	0,15	2,20	0,10
ATA23-002c	21,58	0,06	62,48	0,24	1,16	0,15	2,90	0,10
ATA23-002d	20,70	0,07	61,36	0,64	0,14	0,15	2,60	0,10
ATA23-002e	20,59	0,40			0,96	0,15	1,30	0,10
ATA23-002f/2	20,85	0,15			0,64	0,15		
ATA23-003/1d							1,30	0,10
ATA23-003/1g	19,70	0,29			-2,03	0,15		
ATA23-003/2h	21,05	0,16	61,52	0,25	2,07	0,15	4,20	0,10
ATA23-003/2i-b	20,86	0,16	62,32	0,02	0,96	0,15	3,90	0,10
ATA23-003/2i-y	20,83	0,12	60,08	1,05	-0,01	0,15	1,60	0,10
ATA23-007/1c							3,20	0,10
ATA23-008c							2,30	0,10
ATA23-008h							1,60	0,10
ATA23-009c							3,20	0,10
ATA23-010c							2,50	0,10
ATA23-013							2,10	0,10
ATA23-018							1,60	0,10
ATA23-024c							0,00	0,10
ATA23-025a							-2,10	0,10
ATA23-026							-1,20	0,10
ATA23-045							3,10	0,10
ATA23-046b							4,10	0,10
ATA23-048b	19,16	0,28	57,69	0,71	-0,42	0,15		
ATA23-050e	19,43	0,12	54,88	1,12	-0,84	0,15		
ATA23-052	20,57	0,04	53,11	0,89	-1,51	0,15		
ATA23-100a2	14,99	0,34	45,40	0,19	-4,43	0,15	4,30	0,10
ATA23-100b2	14,68	0,11			-6,63	0,15		
ATA23-100d			45,18	0,07	-1,01	0,15		
ATA23-101a					-2,52	0,15		
ATA23-101c	15,89	0,11	47,60	0,89	-4,78	0,15		
ATA23-101d	19,60	0,40			-1,62	0,15		

ATA23-102a	14,90	0,19	45,71	0,30	-4,56	0,15		
ATA23-102b	14,32	0,09	43,91	0,59	-7,56	0,15		
ATA23-103	20,62	0,40			-2,24	0,15		
ATA23-104b	21,58	0,07	64,75	0,58	-0,80	0,15		
ATA23-109b	16,13	0,24	49,02	0,85	-2,00	0,15	1,60	0,10
ATA23-109c	18,05	0,17	53,72	1,12	-2,52	0,15	4,70	0,10
ATA23-110a					3,98	0,15		
ATA23-111a							0,40	0,10
ATA23-111b	17,29	0,09	50,99	0,77	-4,08	0,15		
ATA23-111c/1	17,27	0,21	50,23	1,66	-4,32	0,15		
ATA23-111c/2	17,70	0,07	51,12	0,66	-4,44	0,15		
ATA23-111d	17,61	0,28	53,28	1,77	-5,16	0,15		
ATA23-112a							9,80	0,10
ATA23-112c	18,55	0,08	53,44	0,06	-3,76	0,15		
ATA23-OD	13,06	0,33			0,34	0,15	-0,50	0,10
MP19-D	18,75	0,12			1,22	0,15		
MPAD-2	21,53	0,06	63,13	0,68	0,15	0,15		
Pique-118D	18,65	0,22			2,05	0,15		
Pique-118D-2	18,06	0,37	55,80	0,28	3,25	0,15		